

**Study of the decay $\eta \rightarrow e^+e^-e^+e^-$ with
WASA-at-COSY**

Inaugural-Dissertation
zur
Erlangung des Doktorgrades
der Mathematisch-Naturwissenschaftlichen Fakultät
der Universität zu Köln

vorgelegt von
Leonid Sergeewitsch Yurev
aus Voronezh

Forschungszentrum Jülich, 2011

Berichterstatter: Prof. Dr. H. Ströher
Prof. Dr. P. Reiter
Tag der mündlichen Prüfung: 26 Januar 2011

Светлой памяти Игоря и Светланы Ивановых

Zusammenfassung

Im Rahmen der vorliegenden Arbeit wurde der doppelte Dalitz Zerfall $\eta \rightarrow e^+e^-e^+e^-$ untersucht. Derzeit ist experimentell für diesen seltenen Zerfall des η Mesons nur eine Obergrenze für das Verzweigungsverhältnis bekannt.

Theoretisch wird von der Quantenelektrodynamik ein Verzweigungsverhältnis von etwa 2.5×10^{-5} vorhergesagt, dreimal kleiner als die gegenwärtige experimentelle Obergrenze. Von wesentlichem Interesse bei Untersuchungen dieses Zerfalls ist die Möglichkeit, den Übergangsformfaktor zu bestimmen, der die elektromagnetische Struktur des zerfallenden neutralen Mesons am $\eta \rightarrow \gamma^*\gamma^*$ Vertex beschreibt. Die invariante Masse der beiden Leptonpaare im Endzustand des $\eta \rightarrow e^+e^-e^+e^-$ Zerfalls entspricht jeweils dem Betrag des Viererimpulses eines virtuellen Photons. Die Kenntnis der Struktur des Übergangsformfaktors kann Hinweise geben, ob zweifache Vektormesondominanz in der Natur realisiert ist – eine Frage, die beispielsweise von großer Bedeutung für Kaon-Zerfälle und das anomale magnetische Moment des Myons ist.

Mit dem WASA Detektor an COSY ist es erstmalig möglich, das Verzweigungsverhältnis des Zerfalls $\eta \rightarrow e^+e^-e^+e^-$ zu bestimmen. Die vorliegende Analyse basiert auf ~ 10 Millionen aufgezeichneten η -Ereignissen, die in der Reaktion $pd \rightarrow {}^3\text{He}\eta$ bei 1 GeV kinetischer Energie produziert wurden. Aus diesen konnten (30 ± 10) $\eta \rightarrow e^+e^-e^+e^-$ Ereigniskandidaten herausgearbeitet werden, entsprechend einem Verzweigungsverhältnis von 2.9×10^{-5} .

Abstract

This work is dedicated to the study of the double Dalitz decay $\eta \rightarrow e^+e^-e^+e^-$. For this rare decay of the η meson only an experimental upper limit for the branching ratio is known. The theoretical prediction is based on Quantum Electrodynamics for the branching ratio is about 2.5×10^{-5} , which is a factor of three below the experimental upper limit.

One of the main points of interest to study this decay is the possibility to measure the transition form factor, which describes the electromagnetic structure of the decaying neutral meson at the $\eta \rightarrow \gamma^*\gamma^*$ vertex. In the final state of the decay $\eta \rightarrow e^+e^-e^+e^-$ there are two lepton pairs, whose squared invariant mass equals the four momenta squared of the virtual photons. The knowledge about the structure of the transition form factor can indicate whether double vector meson dominance is realized in nature, which has important implications for kaon decays and the μ anomalous magnetic moment.

Using the WASA at COSY facility it is possible for the first time to determine the branching ratio of the $\eta \rightarrow e^+e^-e^+e^-$ decay. The data analyzed in this work were taken in the reaction $pd \rightarrow {}^3\text{He}\eta$ at 1 GeV kinetic energy and contain $\sim 10 \times 10^6$ events of η -mesons. A sample of (30 ± 10) $\eta \rightarrow e^+e^-e^+e^-$ event candidates has been extracted, corresponding to a branching ratio of 2.9×10^{-5} .

Contents

1	Theoretical Background and Motivation	1
1.1	Physics of the η Meson	3
1.2	Transition Form Factors	5
1.3	The Decay Mode $\eta \rightarrow e^+e^-e^+e^-$	7
1.4	Available Data	10
1.5	Why $\eta \rightarrow e^+e^-e^+e^-$ with WASA-at-COSY ?	11
2	Experimental Setup	13
2.1	The COSY Storage Ring	15
2.2	Pellet Target	15
2.3	WASA Detector	18
2.3.1	Central Detector	18
2.3.1.1	Mini Drift Chamber	19
2.3.1.2	Plastic Scintillator Barrel	22
2.3.1.3	Superconducting Solenoid	23
2.3.1.4	Scintillating Electromagnetic Calorimeter	24
2.3.2	Forward detector	25
2.3.2.1	Forward Window Counter	27
2.3.2.2	Forward Proportional Chamber	28
2.3.2.3	Forward Trigger Hodoscope	28
2.3.2.4	Forward Range Hodoscope	30
2.3.2.5	Forward Range Intermediate Hodoscope	30
2.3.2.6	Forward Veto Hodoscope	31
2.3.2.7	Forward Range Absorber	31
2.3.3	The light-pulser monitoring system	32
2.4	Data Acquisition system	32
2.5	Trigger system	33
3	Data Analysis	35
3.1	Software Tools	35
3.1.1	Event Generator Pluto++	35

3.1.2	Detector Simulation Monte Carlo Package	37
3.1.3	RootSorter Software Environment	38
3.2	Calibration	39
3.2.1	Calibration of Straw Tube Detectors	39
3.3	Charged Track Reconstruction	42
3.3.1	Central Detector	43
3.3.1.1	Hit Clustering in the Mini Drift Chamber	43
3.3.1.2	Hit Clustering in the Plastic Scintillator Barrel	49
3.3.1.3	Hit Clustering in the Calorimeter	49
3.3.1.4	Track Assignment in the Central Detector	49
3.3.2	Forward Detector	52
3.4	Particle Identification	53
3.4.1	Charged Particles in the Central Detector	53
3.4.2	Charged Particles in the Forward Detector	55
4	Analysis of the η Double Dalitz Decay	59
4.1	Tagging Reaction	59
4.2	Run Information	61
4.3	Experiment Trigger	62
4.4	Preselection and Calibration Sets	63
4.5	Signal and Background Simulation	64
4.5.1	Background Studies	64
4.5.2	Simulation Channels	66
4.6	Analysis Chain	68
4.6.1	Track Selection	68
4.6.2	Normalization Channel $\eta \rightarrow e^+e^-\gamma$	69
4.6.3	Event Selection for the Decay $\eta \rightarrow e^+e^-e^+e^-$	79
4.7	Simulation and Data Comparison	85
5	Results	89
5.1	Method	89
5.2	Consistency Checks	91
5.2.1	Prompt Pion Subtraction	93
5.2.2	Variation of cuts	93
5.3	Systematic Effect by Event Overlap	102
6	Conclusion and discussions	105
7	Appendix	107

Chapter 1

Theoretical Background and Motivation

Introduction

The Standard Model of particle physics summarizes our present knowledge of fundamental particles and their interactions. The theory covers the strong, electromagnetic and weak interactions between the elementary constituents of matter. The electromagnetic and weak interactions were combined together into the electroweak theory during the 1960's by S. Glashow, S. Weinberg and A. Salam (Nobel Prize in Physics in 1979). The Standard Model does not include the gravitational interaction¹ and must be therefore considered as incomplete. According to the Standard Model matter consists of quarks and leptons, which interact via gauge bosons. An interesting fact is that the matter surrounding us today is made up of u - and d - quarks, electrons, ν_e and the gauge bosons, while all other quarks and leptons existed at an early stage of the universe and nowadays can be seen only in cosmic rays and accelerator experiments. The properties of the interactions are characterized by certain regularities and symmetries which are reflected into conservation laws according to Noether's theorem [1], see the table 1.1.

The strong interaction occurs via the exchange of eight massless gluons, which are the gauge bosons of the symmetry group $SU(3)$. The weak interaction is mediated by the three heavy W^\pm , Z bosons of the symmetry group $SU(2)$. The electromagnetic interaction proceeds via the exchange of the massless photon which is the gauge boson of the symmetry group $U(1)$. The difference between U and SU symmetry groups is whether the group is abelian or non-abelian. The consequence of being non-abelian is that in the Lagrangian additional terms appear which lead to a self-interaction of the corresponding gauge bosons.

¹The influence of the gravitation is negligible for particle physics processes.

Conservation law	Strong	Electromagnetic	Weak
Energy E	+	+	+
Momentum p	+	+	+
Electric Charge Q	+	+	+
Baryon number B	+	+	+
Lepton number L	+	+	+
Isospin I	+	-	-
Isospin projection I_z	+	+	-
Strangeness S	+	+	-
Parity P	+	+	-
Combined parity CP	+	+	-
CPT	+	+	+

Table 1.1: Conservation laws in different interactions: "+" means the characteristic is conserved, "-" means it is violated.

Quantum chromodynamics (QCD) is the non-abelian gauge theory of the strong interaction. The corresponding gauge bosons are eight self-interacting gluons, which have colour charge and mediate the interaction between quarks which also carry colour charge². In comparison, due to abelian structure of electromagnetic interaction $U(1)$, the photon has no self-interaction and, therefore, is electrically neutral. The coupling constant of QCD is energy dependent. At higher energies the distances are short and the coupling between quarks gets weaker. In this case quarks behave as asymptotically free particles and this regime can be described by the methods of perturbative QCD. The low energy regime of QCD is characterized by two mechanisms: the confinement of quarks inside hadrons and the breaking (spontaneous and explicit) of chiral symmetry.

At low and intermediate energies the distances become large and the coupling constant becomes stronger. The self-interaction of gluons leads to the confinement of coloured quarks inside bound objects, colourless hadrons, which are the relevant degrees of freedom in this energy regime of QCD. Hadrons are classified into baryons (qqq) and mesons ($q\bar{q}$). The mesons are grouped into different types depending on their quantum numbers, see table 1.2.

The chiral symmetry is a general symmetry of QCD which considers the three light quarks u, d and s to be massless. The spontaneous breaking gives rise to massless excitations, which are the pseudoscalar π, K, η mesons. The fact that quarks have small, but non-vanishing masses leads to the explicit breaking of the chiral symmetry. Therefore in the low energy regime the methods of Chiral

²The term color is used by convention

	S	L	P	J^P
Pseudoscalar meson	0	0	-	0^-
Pseudovector meson	0	1	+	1^+
Vector meson	1	0	-	1^-
Scalar meson	1	1	+	0^+
Tensor meson	1	1	+	2^+

Table 1.2: Classification of mesons according to their spin S , orbital angular momentum L , parity P , total angular momentum J , total angular momentum combined with parity J^P .

Perturbation Theory (ChPT) are used. ChPT is a non-perturbative method based on the idea that at low energies the dynamics should be controlled by the lightest hadrons (the pions) and the symmetries of QCD, for example chiral symmetry. More details can be found in [2].

The η meson plays an important role in understanding of the low energy regime of QCD. All first order decays of η are forbidden because of conservation laws and therefore are sensitive to higher order parameters of ChPT. In addition η decays allow to test the predictions of ChPT and help to validate an effective theory for the hadronic scale.

This work is dedicated to one of the rare η decay, so called double Dalitz decay $\eta \rightarrow e^+e^-e^+e^-$. This electromagnetic process proceeds via two virtual photons. It was observed on the level of two events only, resulting in an experimental upper limit [3]. This decay allows to test the realization of the Vector Meson Dominance Model in nature. The goal of this study is to determine the branching ratio for the decay.

The work is organized as follows:

Chapter 1 contains the theoretical background and motivation to study the decay $\eta \rightarrow e^+e^-e^+e^-$, in chapter 2 the experimental tools are introduced, chapter 3 describes the software and analysis methods with focus on the important experimental setup components. In chapter 4 the analysis chain is described. The result for the branching ratio of $\eta \rightarrow e^+e^-e^+e^-$ is presented in chapter 5. The final chapter summarizes this work and gives an outlook.

1.1 Physics of the η Meson

The η meson belongs to the ground state octet of pseudoscalar mesons as shown in the fig. 1.1, with strangeness $S = 0$ and electrical charge $Q = 0$. The η meson was discovered in pion-nucleon collisions at the Bevatron at Lawrence

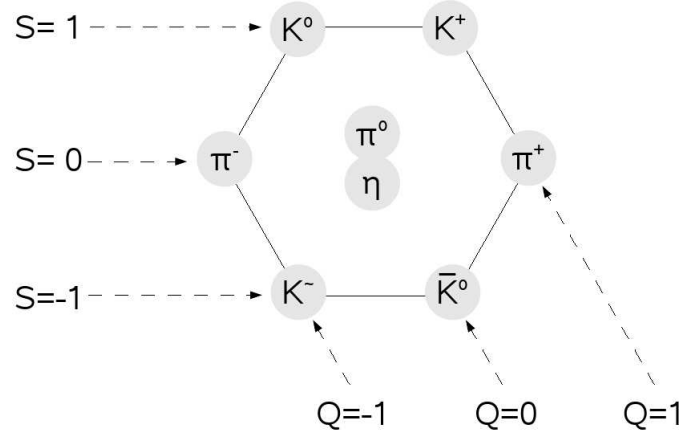


Figure 1.1: The ground state pseudoscalar mesons octet in the coordinates of strangeness S along the vertical axis and electrical charge Q along the diagonal axis.

Berkeley National Laboratory in 1961 [4]. The basic properties of the η meson are listed in the table 1.3.

In terms of the quark model all mesons are quark-antiquark systems. There are nine $q\bar{q}$ combinations among u, d and s quarks and their antiquarks. The η meson is a linear combination of the octet η_8 and singlet η_1 states, given by the formula:

$$\eta = \eta_8 \cos(\theta) - \eta_1 \sin(\theta) \quad (1.1)$$

where octet η_8 and singlet η_1 states have quark composition given by formulas:

$$\eta_8 = \frac{1}{\sqrt{6}}(u\bar{u} + d\bar{d} - 2s\bar{s}) \quad (1.2)$$

$$\eta_1 = \frac{1}{\sqrt{3}}(u\bar{u} + d\bar{d} + s\bar{s}) \quad (1.3)$$

$$\eta = \frac{1}{\sqrt{2}}(u\bar{u} + d\bar{d})\cos(\alpha) - s\bar{s} \sin(\alpha) \quad (1.4)$$

The mixing angle θ was estimated in the range $-(13.83^\circ - 18.76^\circ)$, from the analysis of various decays of vector and pseudoscalar mesons, see [5], [6]. The mixing angle α is related to θ : $\alpha = \theta + 54.7^\circ$, see [7].

Recent measurements by CLEO-c [8] and KLOE [9] have confirmed the NA48 [10] value for η meson mass and nowadays the mass of the η meson is known with a good precision. However, many rare decays of η were not measured precisely because of lack of large statistics η samples. The η meson can participate in the weak, strong and electromagnetic interaction. This and a relatively large mass

m_η	$(547,51 \pm 0.18) \text{ MeV}$
Decay width	1.2 keV
life time	$5 \times 10^{-19} \text{ s}$
B, L	0
S	0
I	0
Q	0
J^{PC}	0^{-+}
G	+1

Table 1.3: The basic properties of the η meson, where B - baryon number, L - lepton number, S - strangeness, Q - electrical charge, isospin - I, J - spin, P - parity, C - charge conjugation and G - G-parity.

cause the η meson to have many decay modes [7]. An overview of η decay physics is given in [11, 12]. However, all decay modes via the strong, electromagnetic and weak interaction are forbidden in the lowest order, which explains why the η , with a life time of $5 \times 10^{-19} \text{ s}$, is relatively long lived particle. The positive eigenvalue for η charge conjugation (C) implies that decays into an odd number of photons are forbidden since the photon C eigenvalue is negative. Thus, also the very rare $\eta \rightarrow \pi^0 e^+ e^-$ decay is forbidden if the electron-positron pair comes from a virtual photon. The decays into lepton-antilepton pairs $\eta \rightarrow \mu^+ \mu^-$ and $\eta \rightarrow e^+ e^-$ cannot proceed via a single virtual photon intermediate state since the spins of an η meson and γ differ by one unit. Within the framework of the Standard Model the decays which are dominated by a two virtual photon intermediate state are suppressed by helicity factors m_l/m_η at each $\gamma l^+ l^-$ vertex. Thus the rates of these decays are small and they might be sensitive to hypothetical interactions.

Many η decays are forbidden by P , CP symmetries, for example the hadronic decays $\eta \rightarrow \pi^0 \pi^0$ and $\eta \rightarrow \pi^+ \pi^-$. The non-hadronic decay modes are summarized in the table 1.4.

1.2 Transition Form Factors

The text below is partly taken from [14]. Electromagnetic structure of charged particle can be obtained by scattering of the charged point-like probe on it. The modification of the differential cross section by the charge distribution in the object of study is given by:

$$\frac{d\sigma}{dq^2} = \frac{d\sigma}{dq^2_{point}} |F(q^2)|^2 \quad (1.5)$$

where $\frac{d\sigma}{dq^2_{point}}$ is the differential cross section for the scattering of an electron by a point-like charged particle, based on the predictions from Quantum Electrodynamics (QED). The form factor $F(q^2)$ in 1.5 characterizes the spatial charge distribution in the particle and can be determined by comparing experimental results on the differential cross section with the exact calculation for point-like particle. In the non-relativistic case the form factor is related to the charge density distribution, described by a Fourier transformation.

The spatial structure of neutral mesons cannot be studied in a similar way because the process with single photon exchange is forbidden due to C - parity, conserved in strong and electromagnetic interactions, see table 1.1. Thus the electromagnetic form factors of neutral mesons are always zero and the internal structure of neutral mesons can manifest itself in radiative decays into a photon and meson of opposite C - parity: $P \rightarrow V\gamma$. The photon can be real or virtual, in the latter case the virtual photon decays into a lepton pair l^+l^- , that is called *internal conversion*:

$$P \rightarrow V\gamma^* \rightarrow Vl^+l^- \quad (1.6)$$

The invariant mass of the lepton pair equals to the four-momentum of the virtual photon. The lepton invariant mass distribution depends on the electromagnetic structure at the $P \rightarrow V$ transition vertex, which is due to a cloud of virtual states. The dynamics of this mechanism is described by the *transition form factor* - the function of the four-momentum of the virtual photon. More details can be found in [14].

The vector meson V in the 1.6 can be replaced by a photon, in this case the decay is called *single Dalitz decay*: $P \rightarrow \gamma\gamma^* \rightarrow \gamma l^+l^-$. The lepton pair mass spectrum is given by formula:

$$\frac{d\Gamma}{dq^2} = \frac{d\Gamma}{dq^2_{point}} |F_{PV(\gamma)}(q^2)|^2 \quad (1.7)$$

The electromagnetic properties of the decaying meson P can be studied at $P\gamma$ vertex. The transition form factor $F_{PV(\gamma)}(q^2)$ in the 1.7 can be calculated from QED and normalized to the two photon decay width. Then the lepton pair mass spectrum is obtained:

$$\frac{d\Gamma(l^+l^-\gamma)}{dq^2\Gamma(\gamma\gamma)} = \frac{2\alpha_{em}}{3\pi m} \sqrt{1 - \frac{4m_l^2}{q^2}} \left(1 + \frac{2m_l^2}{q^2}\right) \frac{1}{q^2} \left(1 - \frac{q^2}{m_P^2}\right)^3 |F_P(q^2)|^2 \quad (1.8)$$

Decay	Experimental value	SM predictions
$\gamma\gamma$	$(3.93 \pm 0.02) \times 10^{-1}$	
$e^+e^-\gamma$	$(7.0 \pm 0.7) \times 10^{-3}$	
$\mu^+\mu^-\gamma$	$(3.1 \pm 0.4) \times 10^{-4}$	
$\mu^+\mu^-$	$(5.8 \pm 0.8) \times 10^{-6}$	
e^+e^-	$< 2.7 \times 10^{-5}$ [20]	
$e^+e^-e^+e^-$	$< 6.9 \times 10^{-5}$ [19]	2.6×10^{-5} (QED) [21]
$\mu^+\mu^-e^+e^-$	$< 1.6 \times 10^{-4}$ [20]	$(1.57 - 2.21) \times 10^{-6}$ [21], [23]
$\mu^+\mu^-\mu^+\mu^-$	3.6×10^{-4} [20]	$(2.4 - 3.7) \times 10^{-9}$ [23], [24]
$\gamma\gamma\gamma$	$< 2.8 \times 10^{-4}$	$3 \times 10^{(-12)}$ [27]
$\gamma\gamma\gamma$	$< 1.6 \times 10^{-5}$	
$\mu^+e^- + \mu^-e^+$	$< 6 \times 10^{-6}$	0

Table 1.4: Non hadronic decay modes of the η meson. The range for the predicted branching ratio is an estimate of the influence of the form factor taken from [21] and [23].

Three electromagnetic decays of the η : $\eta \rightarrow l\bar{l}\gamma$, $\eta \rightarrow l\bar{l}l'\bar{l}'$, $\eta \rightarrow l\bar{l}$ contain information about the transition form factor which is parameterized by the function $F(q_1^2, q_2^2, m_\eta^2)$, describing the $\eta\gamma\gamma$ vertex. Here q_1, q_2 are the four-momenta of the two photons. The transition form factor for single Dalitz decay $F(q_1^2, 0, m_\eta^2)$ has been measured fairly well for the decay $\eta \rightarrow \gamma\mu^+\mu^-$ in [16], also for an overview of the η decays see [17].

1.3 The Decay Mode $\eta \rightarrow e^+e^-e^+e^-$

The decay $\eta \rightarrow e^+e^-e^+e^-$ is closely related to the radiative decays: $\eta \rightarrow \gamma\gamma$, $\eta \rightarrow \gamma\pi^+\pi^-$, $\eta \rightarrow \gamma e^+e^-$ which are driven by the chiral anomaly of Quantum Chromodynamics. The $\eta \rightarrow e^+e^-e^+e^-$ is due to the triangle anomaly and up to one-loop order this can be represented by the Feynman diagram in fig. 1.2a. The decays of the η meson with lepton pairs can be related to the corresponding radiative decays with one or two photons using Quantum Electrodynamics and by introducing the transition form factor $F(q_1^2, q_2^2, m_\eta^2)$. The decay proceeds via two virtual photons each converting to a lepton pair: $\gamma^* \rightarrow e^+e^-$. Within the Vector meson Dominance Model (VDM) the interaction between η meson and two virtual photons proceeds via two vector mesons in the intermediate state (ρ, ω for example), fig. 1.2b. In the final state this decay has four leptons or two dilepton pairs and is called *double Dalitz decay* [18]. The four-momentum q of the emitted virtual photon can vary between twice the lepton mass and the mass of the meson.

The main interest in the lepton pairs is the fact that their invariant mass ($m_{e^+e^-}$)

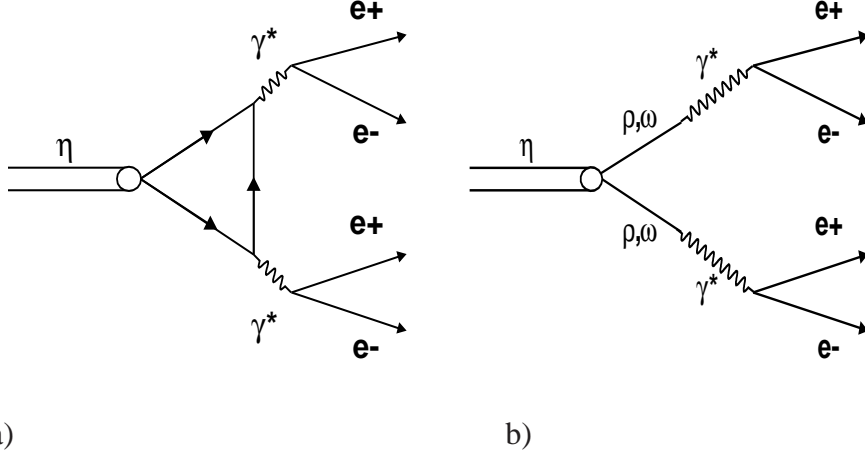


Figure 1.2: The diagrams for $\eta \rightarrow e^+e^-e^+e^-$ decay: a) Quark loop: triangle anomaly and b) Vector meson Dominance Model: vector mesons mediate the interaction between the η and the virtual photons

is equal to the four momentum transfer squared (q^2) in the process of virtual photon emission: $m_{e^+e^-} = q^2$. Thus, the four-momentum squared distribution of virtual photons becomes experimentally observable by internal conversion of the virtual photons to lepton-antilepton pairs. The invariant mass of the lepton pair is an experimental observable while the momentum of the virtual photon can not be measured.

Fig. 1.3 shows a two-dimensional distribution of momenta of two virtual photons of the double Dalitz decay of the η meson. The surface shape will tell about the function which describes the momenta distribution of γ^* . Thus, the $\eta \rightarrow \gamma^*\gamma^* \rightarrow e^+e^-e^+e^-$ decay allows to measure the η meson transition form factor as a function of the momentum-squared of the two photons $F(q_1^2, q_2^2, m_\eta^2)$ in the time-like region for four-momenta between twice the lepton mass and the mass of the η . The four-momentum distribution of the virtual photons depends on the electromagnetic structure at the $\eta \rightarrow \gamma^*\gamma^*$ transition vertex. The form factor correspondingly contains then dynamic information about the electromagnetic structure of the decaying meson [14].

Using the transition form factor, the differential decay width is then modified to:

$$\frac{d\Gamma}{dq^2} = \frac{d\Gamma}{dq^2_{point}} |F(q_1^2, q_2^2, m_\eta^2)|^2 \quad (1.9)$$

where the spectrum of effective masses of the lepton pairs for point-like objects, $\frac{d\Gamma}{dq^2_{point}}$ can be calculated reliably from QED, and the transition form factor

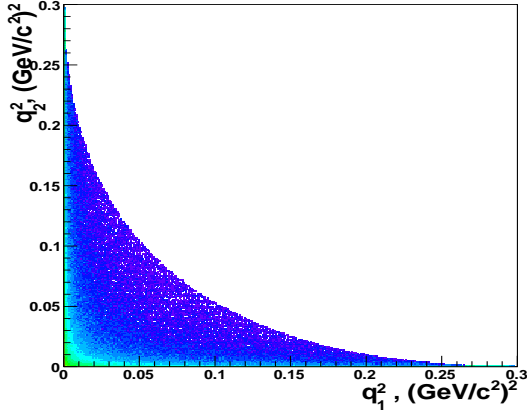


Figure 1.3: Simulation: two-dimensional distribution of the momenta squared of two virtual photons from $\eta \rightarrow \gamma^* \gamma^*$: q_1^2 on the X-axis vs q_2^2 on the Y-axis, $F = f(q_1^2, q_2^2, m_\eta^2) = 1$.

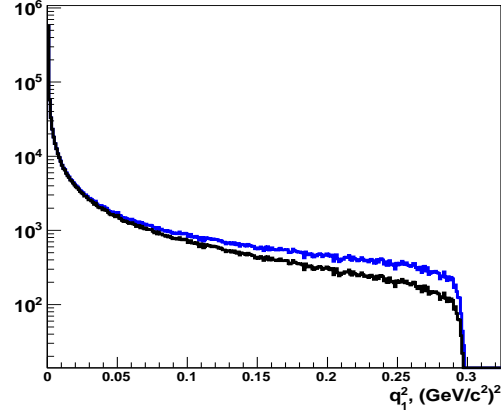


Figure 1.4: Momentum squared of one of the virtual photons from $\eta \rightarrow \gamma^* \gamma^*$ with $F(q^2) = 1$ (black) and with a pole type form factor from equation 1.10 (blue).

can be obtained experimentally.

In the left part of equation 1.9 is a differential decay width modified by introducing the structure of the region of interaction. In the right part there is a known cross section for point-like objects multiplied by transition form factor, which can be obtained experimentally. Including the form factor modifies the mass spectrum of lepton pairs, as can be seen in the fig. 1.4, where a pole type formula was used for the form factor:

$$F(q_1^2, q_2^2) = \frac{\Lambda^4}{(\Lambda^2 - q_1^2)(\Lambda^2 - q_2^2)} \quad (1.10)$$

which corresponds to the standard double vector meson dominance model. For the parameter Λ a mass of $770 \text{ MeV}/c^2$ close to the mass of the ρ meson was taken. The effect becomes significant for higher masses, where two curves diverge. The effects of different form factors in meson-photon-photon processes were investigated in 2001 by Johan Bijnens and Frederik Persson [25].

Based on Quantum Electrodynamics, with a transition form factor $F(q_1^2, q_2^2) = 1$ already in 1967 Jarlskog and Pilkuhn [21] evaluated the ratio based on earlier calculations [22]:

$$R_1 = \frac{\Gamma_{\eta \rightarrow e^+ e^- e^+ e^-}}{\Gamma_{\eta \rightarrow \gamma \gamma}} = 6.6 \times 10^{-5} \quad (1.11)$$

As can be seen from comparing equation 1.9 and 1.11, the decay $\eta \rightarrow e^+ e^- e^+ e^-$

can be related to the $\eta \rightarrow \gamma\gamma$ decay by using Quantum Electrodynamics, where both photons are real and the transition form factor is normalized to unity at $q_1 = 0, q_2 = 0$ (because for real photons $m_\gamma = 0$), it implies the region of interaction is a point-like:

$$F(0, 0, m_\eta^2) = 1 \quad (1.12)$$

According to equation 1.11 the branching ratio is $BR_{\eta \rightarrow e^+e^-e^+e^-} = 2.59 \times 10^{-5}$. The calculations in [22] were done within QED, neglecting a cross term $\chi_{\bar{l}l}$ in the amplitude which originates from the exchange of identical leptons or antileptons in different pairs. Similar calculations were done in [24] neglecting form factor influence. The result for the branching ratio with consideration of the cross term $\chi_{\bar{l}l}$ gives $BR = 2.56 \times 10^{-5}$. Neglecting the cross term the branching ratio slightly changes $BR = 2.41 \times 10^{-5}$. Other calculations of the branching ratio with the cross term $\chi_{\bar{l}l}$ were presented in [25]. The neglect of form factor result gives the branching ratio 2.52×10^{-5} . Including the form factor from the VDM, three different form factors were used and the branching ratio was found in the range $(2.52 - 2.65) \times 10^{-5}$. The most recent calculations were done in [26], for QED case without cross term $\chi_{\bar{l}l}$ the branching ratio was found 2.55×10^{-5} , with cross term 2.54×10^{-5} . Introducing two different form factors from VDM gives the range for the branching ratio $(2.54 - 2.67) \times 10^{-5}$.

Thus, the results for the branching ratio based on QED agree rather well between each other. As can be seen introducing the form factor increases the branching ratio. In general the branching ratio for $\eta \rightarrow e^+e^-e^+e^-$ does not expose significantly either by introducing the form factor or the cross term $\chi_{\bar{l}l}$. The influence of the form factor on lepton pair invariant mass spectrum was demonstrated in the figure 1.4: the effect becomes larger for higher masses.

In the framework of the analysis presented in the thesis the form factor influence was neglected.

1.4 Available Data

The decay $\eta \rightarrow e^+e^-e^+e^-$ has not been yet observed and the only experimental data offer an upper limit for its branching ratio. The theoretical predictions based on Quantum Electrodynamics give a branching ratio of 2.6×10^{-5} , [21]. The latest experimental limit on the $\eta \rightarrow e^+e^-e^+e^-$ branching ratio comes from the CMD-2 experiment [19] at the VEPP-2M e^+e^- collider. The upper limit for the branching ratio of the $\eta \rightarrow e^+e^-e^+e^-$ was measured to be 6.9×10^{-5} with a confidence level of 90%. WASA/CELSIUS found two event candidates of the $\eta \rightarrow e^+e^-e^+e^-$ with an upper limit of 9.7×10^{-5} .

In parallel with the WASA activity there are ongoing studies, performed by the KLOE experiment at the DAFNE e^+e^- collider in Frascati [30], with one of the

focuses of experimental program including η decays. In the frame of public meetings the KLOE has reported about 400 event-candidates of the $\eta \rightarrow e^+e^-e^+e^-$ decay. Therefore it is very interesting to compare two independent measurements for the rare decay.

1.5 Why $\eta \rightarrow e^+e^-e^+e^-$ with WASA-at-COSY ?

The decay contains important information about two vector meson exchange processes which are negligible compared to one vector meson exchange according to ChPT. However there are no experimental data to check this.

WASA was designed for studies of the decay products of light mesons, particularly it was optimized for dilepton pair identification by introducing material and dimensions to reduce the probability of photon conversion, the details will be discussed later in chapter 2. As it was mentioned, the upper limit for the branching ratio is the only experimental information and WASA/CELSIUS has already identified it. The measurements were based on a 2×10^5 η -s sample and now using the upgraded facility, having abundant η -sample and known methods which were used by WASA/CELSIUS, it becomes possible to obtain a solid number for the branching ratio and later focus on the lepton mass spectra study.

In this thesis a statistically more significant η -sample is analysed with a similar method to that used by WASA/CELSIUS, therefore it can be expected to produce a solid number for the branching ratio with lower statistical error. The aim of this thesis is to present $\eta \rightarrow e^+e^-e^+e^-$ event candidates with reasonable signal-to-background ratio and to determine the branching ratio of the $\eta \rightarrow e^+e^-e^+e^-$.

Chapter 2

Experimental Setup

Any experiment in nuclear physics has the goal to explore the building blocks of matter by colliding particles at high energies and registering the produced re-jectiles. An experiment includes three major parts: an accelerator facility, a target and a detector setup. The accelerator facility delivers a beam of particles which interacts with the target and the products of this interaction are registered by a sys-tem of detectors. Instead of a fixed target a second beam of particles coming from the opposite direction can be used, in this case the accelerator facility is called a collider.

The Wide Angle Shower Apparatus (WASA) was designed to study light me-son production in hadronic interactions and their decays. The mesons are produced in proton-proton and proton-deuteron interactions. Originally it was operated at the CELSIUS¹ ring in Uppsala, Sweden, with proton beam momenta up to 2.1 GeV/c . In summer 2005 after the shutdown of CELSIUS the setup was trans-ported to COSY² facility, Juelich, Germany, which offers higher beam momenta up to 3.7 GeV/c as well as polarized beams. This adds possibility to study other mesons than η such as η' , ω , ϕ .

After the setup was transferred to Juelich, its components were inspected in the laboratories of the Nuclear Physics Institute. Certain modifications and upgrades were done in order to improve the detector performance. The data acquisition has been renewed.

The detector is operated with an internal hydrogen and deuteron target using a pellet target system with effective target densities $> 10^{15} \frac{atoms}{cm^2}$ providing high luminosities in the order of $10^{32} cm^{-2} s^{-1}$.

¹Cooling with Electrons and Storing Ions from Uppsala-cyclotron

²COoler SYnchrotron

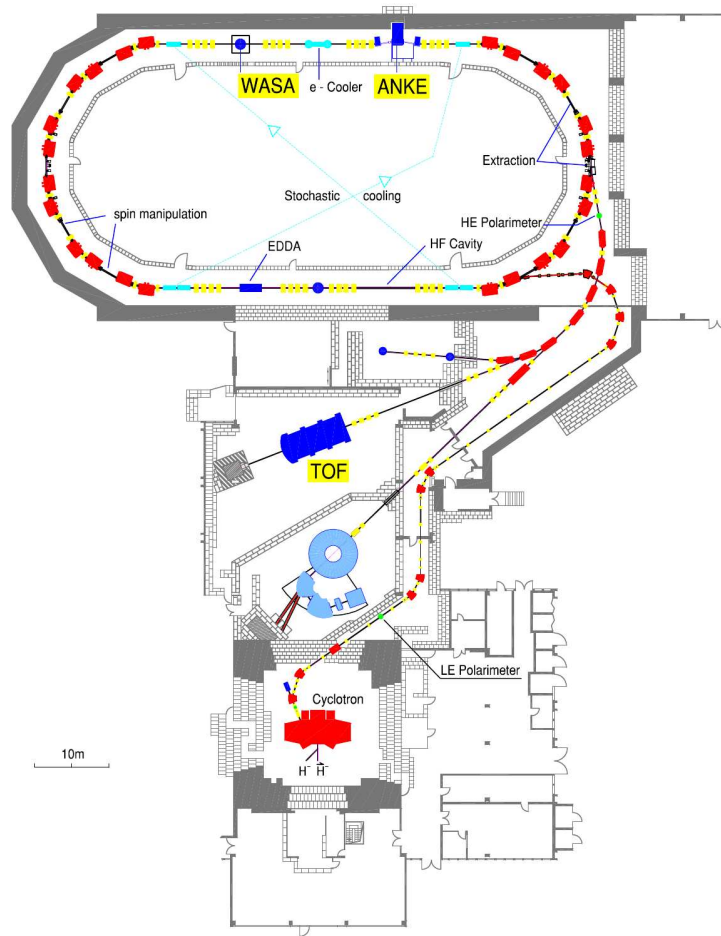


Figure 2.1: COSY floor plan: schematic view

2.1 The COSY Storage Ring

The COoler SYnchrotron COSY is a storage ring [32] providing high precision proton and deuterium beams in the momentum range from $0.3 \text{ GeV}/c$ up to $3.7 \text{ GeV}/c$. The accelerator complex depicted in the figure 2.1 consists of several ion sources, the isochronous cyclotron, a 100 m long injection beam line, the COSY ring with a circumference of 184 m, and extraction beam lines to external experiments. The cyclotron serves as injector to COSY and is fed by either unpolarized or polarized H^- and D^- sources. The injection momentum of the ions is $296 \text{ GeV}/c$.

COSY has the shape of a longitudinally stretched ring with two arc sections of 52 m length and two straight sections of 40 m length, where the internal experiments are located. Comparing with the conditions at CELSIUS, COSY offers certain improvements in experimental conditions: fast magnet ramping, dispersion-free target position, electron and stochastic cooling and a smooth microscopic time structure of the beam. The COSY ring can be filled up 10^{11} particles leading to typical luminosities of $10^{31} \text{ cm}^{-2} \text{ s}^{-1}$ with a cluster target and $10^{32} \text{ cm}^{-2} \text{ s}^{-1}$ with a pellet target. Two cooling systems [33] are used: electron-cooling at injection energy and stochastic cooling for higher momenta. The electron cooling is used with 22 keV electrons to increase the intensity of the polarised proton beam. Stochastic cooling is working in the proton momenta range between $1.5 \text{ GeV}/c$ and $3.5 \text{ GeV}/c$.

After acceleration and injection, the beam is stored and can be used for experiment. In case of internal experiments, the beam interacts loses its intensity. Thus, the beam in the storage ring has only a certain lifetime. When it is used up, new particles have to be injected. The time between two injections is called a it cycle. A typical beam cycle during the beamtime in November, 2008 is shown in the figure 2.2. The beam intensity is defined by the beam current and is decreasing to the end of the cycle due to interaction with the pellets, following the black curve.

2.2 Pellet Target

The study of rare processes puts some demands on the target: a suitable effective target thickness (in the order of $2 \times 10^{15} \frac{\text{atoms}}{\text{cm}^2}$), a good definition at the interaction point definition and access to a solid angle close to 4π . Another requirement is especially important for final states with electron-positron pairs - that there should be only little material for the reaction products to reach the detectors. This helps to minimize the background from photon conversion. All these requirements can be met with a pellet target.

The pellet-target system is an unique target developed particularly for high

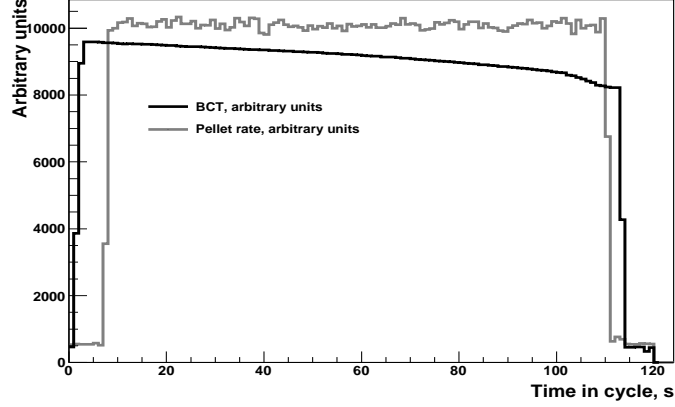


Figure 2.2: Beam current in arbitrary units and pellet rate per second on the Y-axis as a function of time in cycle on the X-axis during a beamtime in November, 2008, reaction $pp \rightarrow pp\eta$ at 1.4 GeV . That illustrates how the beam intensity is decreasing due to beam-target interaction.

luminosity and high precision measurements [34]. The setup produces a narrow stream of frozen hydrogen droplets which cross the beam vertically from above. The idea of using a running stream of droplets was first proposed in 1984 by Sven Kullander at CELSIUS.

The layout of the setup is depicted in figure 2.3. The pellet generator is located on top of the setup where a high purity jet of liquefied gas (H_2, D_2) is broken up into individual droplets by vibrating glass nozzle. When the droplets enter the vacuum chamber through an injection capillary they freeze due to evaporation and become solid spheres or pellets. At the same time they are accelerated up to velocities of 100 m/s by the gas flow through the capillary. Further down a skimmer is used to collimate the pellet beam before entering the pellet beam tube. The pellet tube is 2 m long and has a diameter of 7 mm . The pellets have a size of $20\text{-}40 \mu\text{m}$ and form a pellet beam with a diameter of $2\text{-}4 \text{ mm}$ at the interaction point. The small size of the pellets is one of the important parameters to achieve a well defined interaction point and to reduce the probability of secondary interactions in the target.

The initial droplet rate is determined by the vibration frequency of the nozzle. However, mainly due to turbulences during the vacuum injections the typical pellet rate is $3000\text{-}10000 \text{ s}^{-1}$ after collimation at the interaction point. The typical operation parameters of the pellet target are summarized in the table 2.1. The photo of the pellet stream is shown in the figure 2.4.

After passing the COSY beam the pellets are stopped in the pellet beam dump and the gas from the evaporating pellets is removed by turbo pumps.

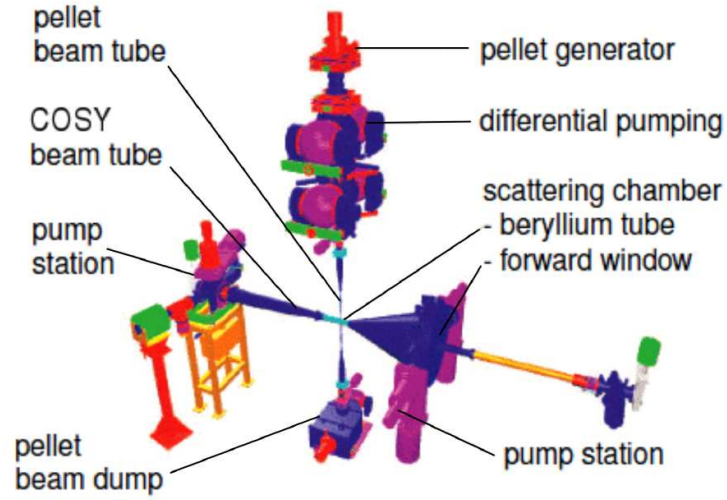


Figure 2.3: Pellet target setup: schematic view.

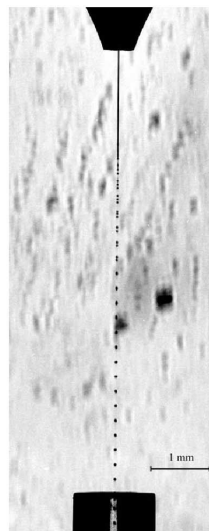


Figure 2.4: Photo of the pellet target stream: the nozzle (truncated cone) is at the top, the vacuum capillary in the lower part.

Pellet size	20-40 μm
Pellet frequency at nozzle	70 kHz
at interaction point	5-12 kHz
Pellet flight velocity	60-100 m/s
Pellet beam angular divergence	0.04 $^\circ$

Table 2.1: Typical pellet target parameters achieved during the beamtime in October-November, 2008.

2.3 WASA Detector

The WASA detector was designed to study the decays of light mesons. It can be divided into two main parts, the forward and the central detector. The forward detector provides the reconstruction of the recoil particles and allows to tag on the produced meson via the missing mass technique. The central detector then detects and identifies both charged and neutral decay products of mesons.

A cross section of the complete setup is shown in the figure 2.5. The WASA master coordinates x, y, z are given in a right handed coordinate system with the origin at the vertex of the reaction. The z -axis is directed along the beam, the x -axis goes perpendicular to the z -axis outward from the COSY ring in the horizontal plane, the y -axis is orthogonal to x - z plane directed upwards.

In the following sections the individual components of the detector are described in more details.

2.3.1 Central Detector

The central detector measures charged particles and photons originating from meson decays. The Mini Drift Chamber (MDC) and the Plastic Scintillator Barrel (PSB) are placed inside a magnetic field provided by a superconducting solenoid. With the MDC the momenta of charged particles are measured and positively and negatively charged particles are distinguished by the bending direction of the track in the magnetic field. The PSB also delivers information about the energy deposit of charged particles and provides fast signals which are used on trigger level. In addition the Scintillator Electromagnetic Calorimeter (SEC) surrounds MDC and PSB and measures the energy deposit of both charged and neutral particles. In combination with the information from the PSB one can distinguish between charged and neutral particles.

The Central Detector covers polar angles in the range from 20° to 169° and the complete azimuthal angular range. All three components together provide the

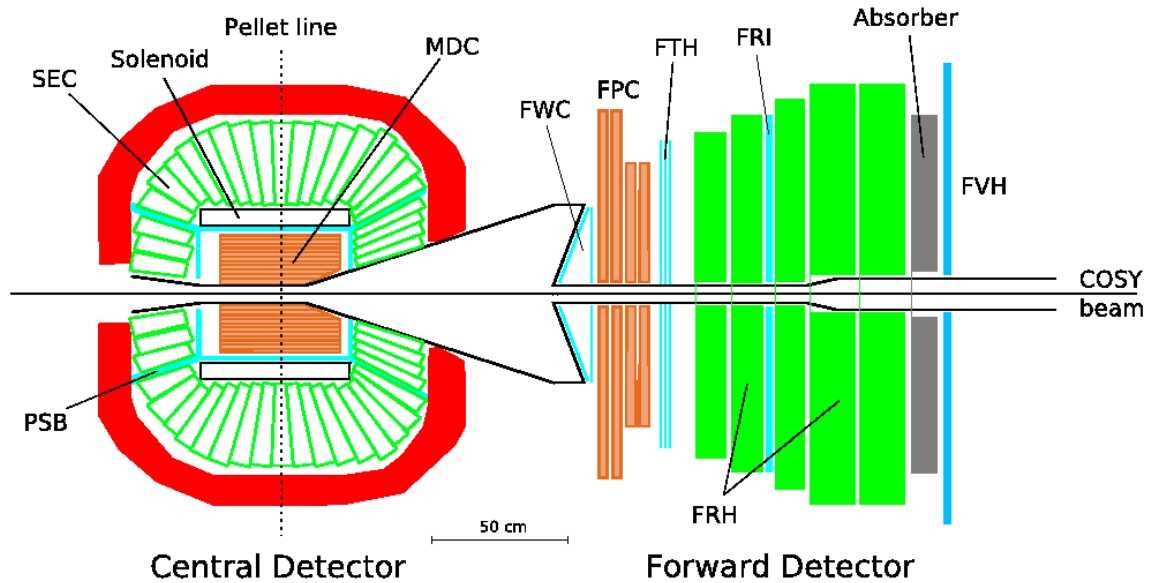


Figure 2.5: Cross section of the WASA detector. For a discussion of the individual components see text.

full four-momentum for each particle.

2.3.1.1 Mini Drift Chamber

The MDC is used to measure charged particles. It is built around the interaction point covering scattering angles from 24° to 159° . The detector consists of 1738 drift tubes in a cylindrical geometry. The tubes are organized into 17 concentric layers centered at the beam axis. In order to keep the amount of material low and to reduce secondary interactions, each tube is made from a thin $25 \mu\text{m}$ aluminized mylar wall tube and a stainless steel sensitive wire of $20 \mu\text{m}$ diameter. These type of drift tubes is called *straw tube*.

The mechanical construction of the MDC is symmetric with respect to the YZ -plane and can be divided into two halves: each layer of the MDC consists of two semi-layers, which form a cylindrical surface. The most inner and outer layer of the straw tubes are located in radii of 41 and 203 mm respectively. Numbering the layers from inside to outside, the nine odd layers are parallel to the z -axis while the eight even layers are stereo layers with different skew angles ($6^\circ - 9^\circ$) with respect to the z -axis. Therefore, the axes of the tubes in stereo layer form a hyperboloidal surface. The axial layers provide two-dimensional information about the track coordinates in the XY -plane. In addition, the stereo layers are

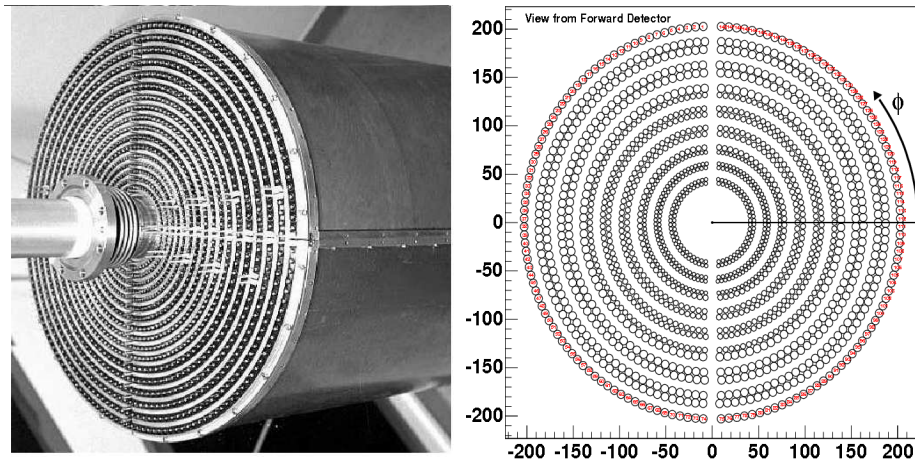


Figure 2.6: Left: backward photo of the MDC layers with incoming beam pipe. Right: depiction of the straw tubes as a projection to XY-plane, the scale on the axes is in millimeters.

used to measure the z coordinates of the track.

The layers can be divided into three groups with diameters of 4, 6 and 8 mm. The first five inner layers have a diameter of 4 mm. Furthermore, the length of these tubes is increasing from inside to outside due to the cone shape of the scattering chamber in forward direction (see the black contour in the figure 2.5). The outer most twelve layers have the same length: the layers from six to twelve have a diameter of 6 mm, the five outer layers have a diameter of 8 mm. All layers are aligned with respect to the backward end of the MDC, see figure 2.6, left. Each layer is supported by $Al - Be$ (50% Al -50% Be) semi-cylindrical plates, i.e. semirings, see figure 2.7. These semirings are interleaved with the straw tube layers and finally the whole construction is covered by a 1 mm thick $Al - Be$ cylinder. Each semi-layer can be flushed with gas individually. The semi-layers were joined into one layer which is flushed with gas. Thus, each MDC layer is monitored by means of input and output gas flows. During the inspection of the MDC before the installation at COSY gas leakages were identified and classified by the gas losses.

The MDC is operated with a commonly used gas mixture: 80 % Ar and 20 % C_2H_6 at atmospheric pressure. This choice of the gas mixture has several advantages: relatively low operating voltage can be applied to the wires in order to provide a high rate capacity and, therefore, the operation becomes more safe, as the major component of the mixture is noble gas the low interaction ability of gas with material of straws prevents from *aging effects* [35]. Another advantage is the linear drift function of the gas mixture. Additional information can be found in [31].

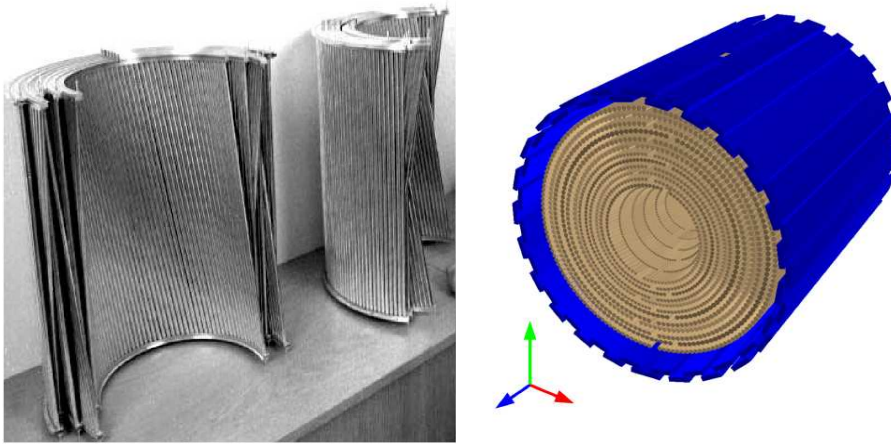


Figure 2.7: Left: the semi-cylindrical plates support and separate the layers of straw tubes, the visible inclined plate illustrates how the stereo layers are interleaved with the parallel layers. Right: barrel part of the PSB(blue) covers the MDC layers.

Signal wires are connected to newly developed electronics based on CMP-16 amplifier-discriminators (for details see [36]) via combined signal-high voltage cables. The CMP-16 modules produce a logic signal in the LVDS-standard³ which is then passed to a TDC⁴.

The working principle of the MDC is based on the motion of charged particles in an electric field: when a charged particle crosses a gas volume the gas is ionized and the produced electrons are accelerated along the electric field, finally producing an *electron avalanche* and positively charged ions in the region close to the anode-wire. The information about the coordinates of the charged particle track is determined through the measurement of the drift time of electrons and ions, more detailed information can be found in [37]. The chamber measures three dimensional trajectory of a charged particle in a nearly uniform magnetic field, then the momentum is calculated from the curvature of particle trajectory in magnetic field.

The momenta of electrons and positrons can be measured in the range about of $20 \text{ MeV}/c$ - $600 \text{ MeV}/c$. The momentum range of heavier charged particles are slight different, for pions the range is $100 \text{ MeV}/c$ - $600 \text{ MeV}/c$, for protons it's $200 \text{ MeV}/c$ - $800 \text{ MeV}/c$.

The MDC performance during the beamtime in spring 2008 is shown in the figure 2.8. This study is based on the reaction $pp \rightarrow d\pi^+$ at 600 MeV , where the π^+ is identified in the Central Detector by PSB and SEC and the deuteron is

³Low Voltage Differential Signal

⁴Time-to-Digital Converter

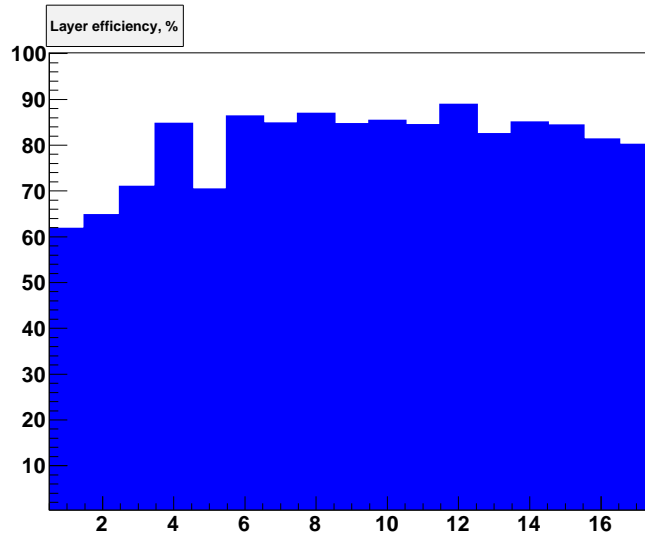


Figure 2.8: The MDC layer efficiency based on the tracks reconstructed by the PSB and SEC. The lower efficiencies of the first layers are due to larger amount of not responding channels, the fifth layer has the largest number of 20% damaged tubes from total number of tubes in the layer.

detected in the Forward Detector. The signature of the two body reaction allows the preselection of a clean sample of one track events in the Central Detector. The histogram illustrates the individual layer efficiencies of the MDC, which are based on the amount of MDC tracks relatively to the tracks found by PSB and SEC. The average efficiency is around 80 % for individual layers.

2.3.1.2 Plastic Scintillator Barrel

The Plastic Scintillator Barrel (PSB) surrounds the mini drift chamber and consists of three parts: the central (barrel) part and forward and backward end caps, see figure 2.9. The central part has a cylindrical geometry around the beam axis. Each part is made of 48 thin plastic elements of 8 mm thickness, see figure 2.3.1.2. The most bottom and the most top elements in the barrel are divided into two halves in order to provide space for the pellet target pipe: the gaps are visible in the figure 2.9.

The elements in the barrel overlap by 6 mm. With such design gaps between two neighboring strips can be avoided and resulting in an increased detection efficiency. The forward and backward parts consist of elements of trapezoidal shape, see figure 2.9. The elements in the forward cap are perpendicular to the beam axis

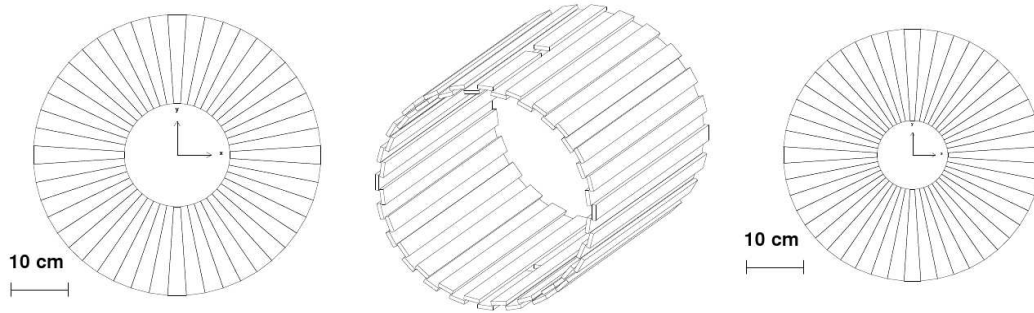


Figure 2.9: From left to right: forward, central and backward part of the PSB. Two holes situated diametrically opposite in the central part are for pellet target pipes.

and flat, forming a disc. The elements in the rear cap are inclined outward and form a conical surface with an angle of 60° . Each element is read out individually by a photomultiplier. The scintillation light is transferred from the scintillator to the photomultiplier via light guides.

The PSB provides time and amplitude information and has two important functions:

- as a thin plastic scintillator it provides fast time signals for the trigger logic discriminating charged and neutral particles
- the energy deposit is used for particle identification via ΔE -p plots.

2.3.1.3 Superconducting Solenoid

The Superconducting Solenoid (SCS) surrounds MDC and PSB and provides an axial magnetic field along the Z -axis. The thickness of the solenoid is optimized such, that photon conversion is minimized. Accuracy of the energy measurements in the calorimeter and equals to $0.18 X_0$. The coil is cooled down by liquid helium and operated at $4.5K$.

The return path for the magnetic flux is provided by an iron yoke, the red thick contour in figure 2.5. The yoke has two purposes: it confines the magnetic field in the central part of WASA and serves as support structure for the photomultipliers of the calorimeter. It contains 1012 holes for connecting the calorimeter crystals to their photomultiplier tubes by means of plastic light guides. The magnetic field was measured by a hall probe. The field distribution was calculated and compared with simulations of magnetic field distributions. The distribution of the magnetic field inside the iron yoke calculated for a coil current of $667 A$ is shown in the

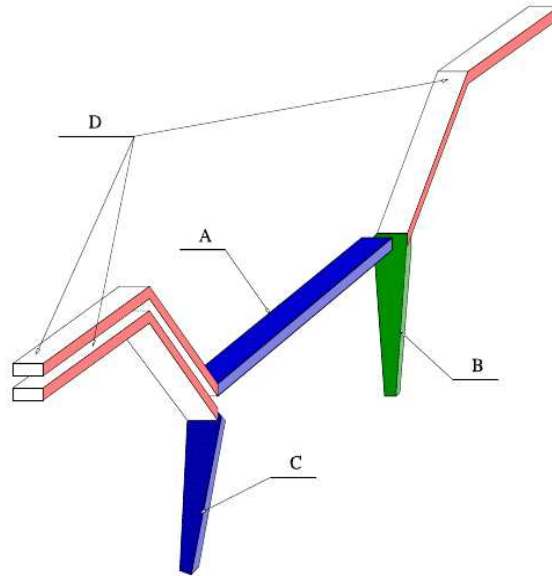


Figure 2.10: Schematic view of one Plastic Scintillator Barrel element: from forward part (B), central part (A) and backward part (C). The light is transferred by lightguides (D).

figure 2.11. The field uniformity inside the MDC is $1.22 \pm 20\%$ T. A more detailed description of the SCS can be found in [38].

2.3.1.4 Scintillating Electromagnetic Calorimeter

The Scintillating Electromagnetic Calorimeter (SEC) is placed between the solenoid and the iron yoke, covering the MDC and the PSB. It consists of 1012 sodium doped *CsI* crystals for measuring energies and angles of photons and charged particles in the polar angular range between 20° and 169° .

The SEC is divided into three parts: the central part and two end caps (backward and forward), see figure 2.12. There are gaps between the central part and end caps which are needed for the lightguides of the Plastic Scintillator Barrel. It covers nearly the complete azimuthal angle from 0° to 360° having two holes for the pellet pipe and the solenoid chimney for liquid helium (not shown in the figures).

Each crystal has a shape of truncated quadrangular pyramid (figure 2.13). The crystals are organized into 24 rings (layers) with centers situated on the beam pipe axis. The forward end cap is represented by 4 layers of 36 crystals each and covers the scattering angle in the range an 20° - 36° . The central part consists of 17

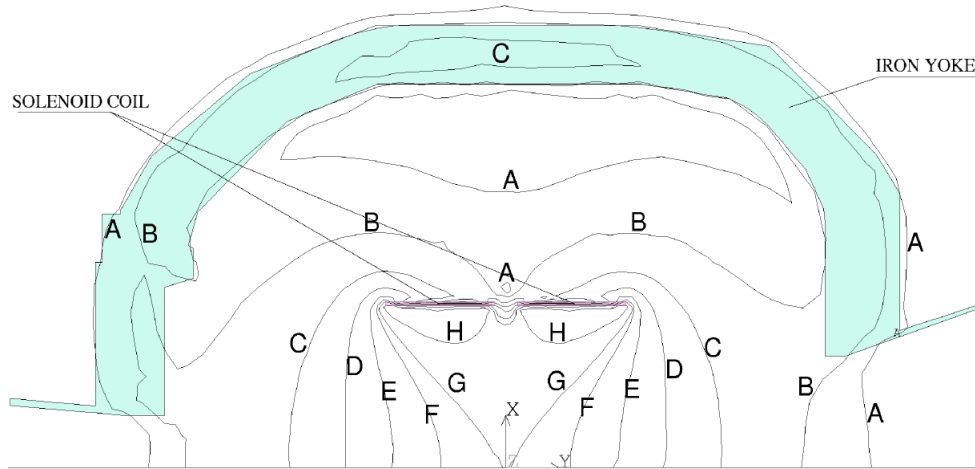


Figure 2.11: Calculated values of the magnetic field inside the iron yoke for a coil current of 667 A. The marked contours constrain the regions with the same magnetic field values. Contour maxima are indicated by lines marked A-H, where: A = 0.10 T, B = 0.25 T, C = 0.50 T, D = 0.75 T, E = 1.00 T, F = 1.20 T, G = 1.30 T and H = 1.50 T.

layers with 48 crystals each, covering an angular range 40° - 140° and the backward end cap (red elements in the left part of the figure 2.12) with 3 layers of crystals covers the angles up to 169° . More detailed information about the mechanical construction of the SEC can be found in [39], [40].

The placement of the solenoid inside of the calorimeter allows using photomultipliers outside of the return yoke. Lightguides are used for signal transmission from the crystals to the photomultipliers through the iron yoke, see 2.13. Thus, all read out electronics is situated outside the magnetic field and not affected by that. The SEC is involved in the trigger logic by using the information about the multiplicity of groups of crystals above a variable energy threshold.

The minimum energy for photon detection in SEC is around 2 MeV. The relative energy resolution for photons is given by: $\frac{\sigma_E}{E} = \frac{5\%}{\sqrt{E}}$, where the energy E is measured in GeV . The angular resolution is limited by the crystal size.

2.3.2 Forward detector

The forward detector measures charged recoil particles and scattered projectiles in the polar angular range between 3° and 18° . It consists of 11 scintillator hodoscopes in different configurations and 4 planes of straw tubes. The subdetectors form a sequence of planes each one perpendicular to the beam axis except the first layer of the Forward Window Counter. This resembles the conical surface of the exit window of the scattering chamber, see 2.5.

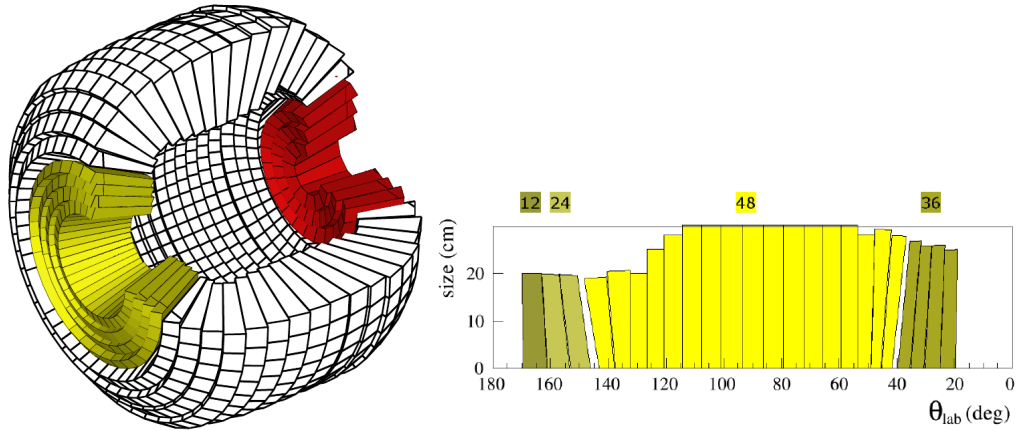


Figure 2.12: Left: the view cut of the Scintillating Electromagnetic Calorimeter, crystals of the backward part are marked red, crystals of the forward part are marked green, the central part crystals are white. Right: the coverage of the polar angle by the calorimeter. The numbers on the top correspond to the numbers of crystals per calorimeter ring.



Figure 2.13: Fully equipped calorimeter module with CsI crystal, lightguide, photomultiplier and housing.

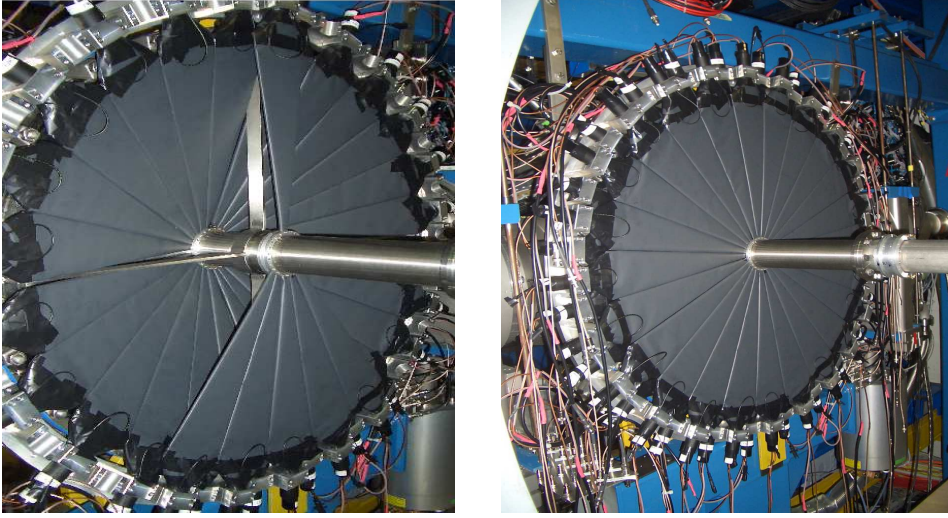


Figure 2.14: The photo of the FWC. Left: a complete first layer and some segments of the second layer. Right: complete second layer overcasts the first layer.

In general, time and amplitude information from the scintillators is used in the trigger logic and later for particle identification by using the ΔE - E technique. The straw tube detector is used to improve the angular resolution by measuring precise track coordinates.

In the next subsections the geometry and the purpose of each component of the forward detector is given.

2.3.2.1 Forward Window Counter

The Forward Window Counter is the first subdetector following the exit window of the scattering chamber. It consists of two layers of scintillator counters in a *pizza-like* shape. Both layers are made from 3 *mm* thick plastic scintillators. Each layer consists of 24 radial segments which are read out individually by photomultipliers. The layers are shifted by half of segment respectively to each other providing overlap between scintillators and, therefore, a complete coverage in azimuthal angle. The first layer is inclined by 80° respectively to the beam axis and adheres closely to the scattering chamber surface, forming a conical surface. The second layer is planar, perpendicular to the beam axis and is situated right after the first layer, see figure 2.14.

Using this detector in the trigger significantly reduces the background from secondary interactions in the beam pipe. A low and high threshold on the amplitude allows the discrimination of particles according to their ionization density.

This is used to separate ${}^3\text{He}$ tracks from the protons and deuterons, since ${}^3\text{He}$ ions deposit more energy than protons and deuterons. Thus, it provides cleaner tagging of the $pd \rightarrow {}^3\text{He}\eta$ reaction already on trigger level.

2.3.2.2 Forward Proportional Chamber

The Forward Proportional Chamber (FPC) is placed directly after the Window Counter. It consists of 4 planar modules, each with four layers of 122 cylindrical drift tubes (straw tubes) of 8 mm diameter. Similar to MDC, see 2.3.1.1, the tubes are made from aluminized mylar of $26\ \mu\text{m}$ thickness. The sensitive wire is made from stainless steel and has a diameter of $20\ \mu\text{m}$. Each wire is stretched with a tension of 40 g.

The straw tubes in the layers are staggered by shift of one tube radius respectively each other. This is the most dense configuration, providing as much as many tubes as possible along the straight trajectory of the particle. The first two modules are rotated by -45° and $+45^\circ$ degrees in azimuthal angle, see figure 2.15. The tubes in the third module are parallel to Y -axis and in the last, fourth, module the tubes are parallel to X -axis. Similar to MDC, the straw tubes of the FPC are read out from one side by the same electronics, however different to the MDC the electronics is mounted directly on the modules, avoiding signal transmission via the *high voltage-signal* cables.

The FPC is supplied by a common gas system for straw detectors, providing $20\%C_2H_6$ - $80\%Ar$ gas mixture under atmospheric pressure. In September 2007 all four modules were installed and operated all together the first time. The FPC serves as an accurate coordinate detector providing precise angular information for reconstructing tracks of the particles originating from the target region.

2.3.2.3 Forward Trigger Hodoscope

The Forward Trigger Hodoscope is the next scintillator detector placed after the FWC. It is built from three layers of 5 mm thick plastic scintillators. The first layer counts 48 sectors in a pizza-like manner. The two others layers consist of 24 elements each, built as Archimedian spirals with different orientation to each other. Such a special geometry provides a pixel structure.

In figure 2.16 the situation with two charged tracks crossing the FTH elements is shown (fired elements are marked black). In the right panel the projection of the layers illustrates how two tracks cross them, each point is defined by the elements from three layers. With this structure it is possible to solve multi-hit ambiguities. All elements are read out individually by photomultipliers.

The FTH plays an important role in the trigger logic. It provides hit multiplicity as well as azimuthal and polar angular information on the trigger level.

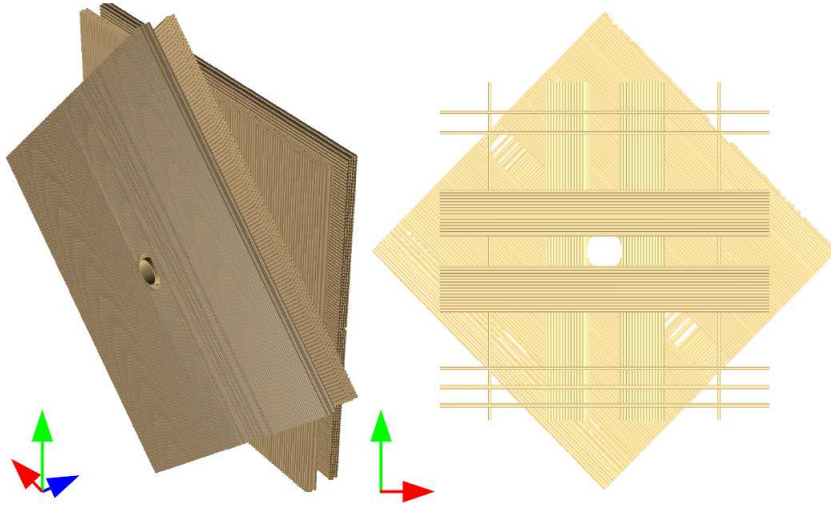


Figure 2.15: The FPC modules: 3-D view to the left and the position of the tubes in different modules to the right(some internal tubes are removed for better illustration).

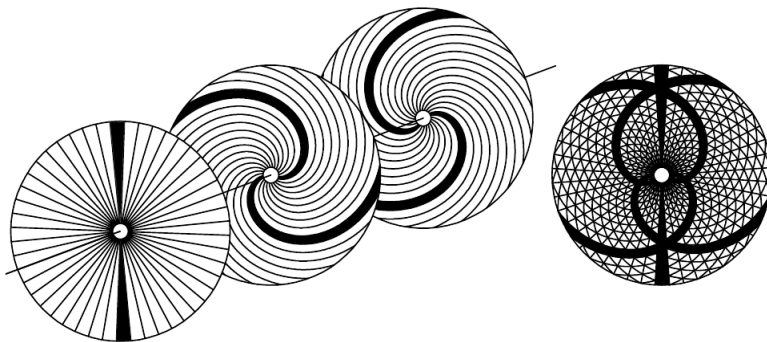


Figure 2.16: The FTH view, left is a 3-D view of element orientation in each layer; right is a projection of elements from all layers.

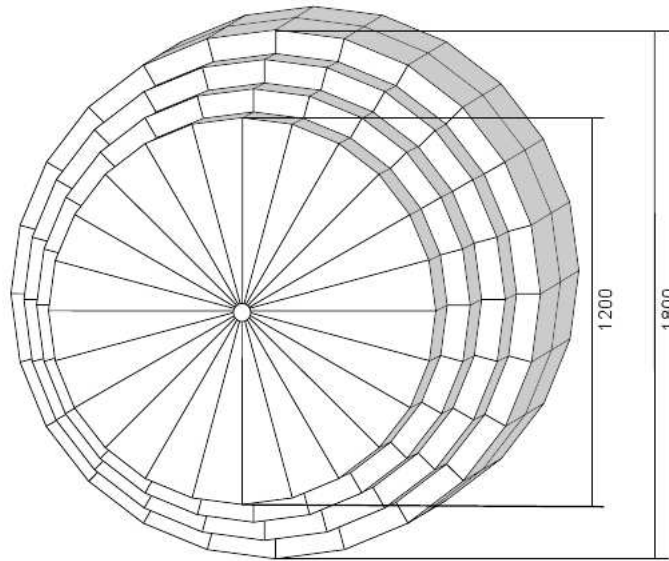


Figure 2.17: The FRH layers are situated behind each other, the dimensions are in *mm*.

2.3.2.4 Forward Range Hodoscope

The Forward Range Hodoscope (FRH) is a system of five layers of thick plastic scintillators: the first three layers have a thickness of 110 *mm* thickness, the other two of 150 *mm*. Each layer is a disc with 24 plastic scintillators, arranged in a pizza-like manner. The diameter of every next layer is increasing, in order to cover the full angular range up to 18° . The fifth layer diameter is the same as the fourth, see figure 2.17.

The main purpose of thick detector is to measure the energy loss of the particles, which will then be used to recalculate the initial kinetic energy at the interaction point. The stopping power of the Range Hodoscope for pions is 200 *MeV*, for protons 360 *MeV*, for deuterons 450 *MeV*, ^3He ions 1000 *MeV* can be stopped and α -particles 1100 *MeV*. As a scintillator detector the Range Hodoscope provides fast signals to the trigger logic.

2.3.2.5 Forward Range Intermediate Hodoscope

The Forward Range Intermediate hodoscope is a double layer hodoscope placed between the second and the third planes of the FRH. There are 32 rectangular elements in each layer, in the first layer the elements are situated horizontally and in the second - vertically, see figure 2.18. This is an additional scintillating detector

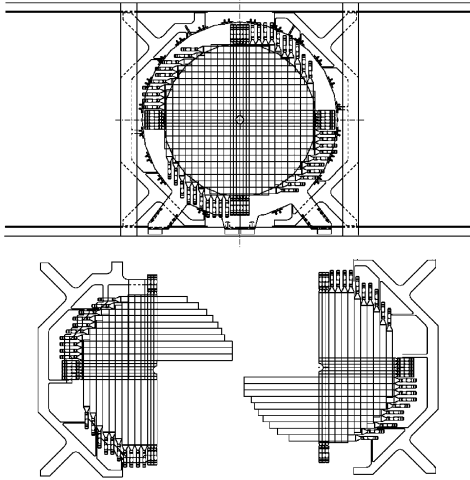


Figure 2.18: The FRI hodoscope: two layers of scintillators perpendicular to each other.

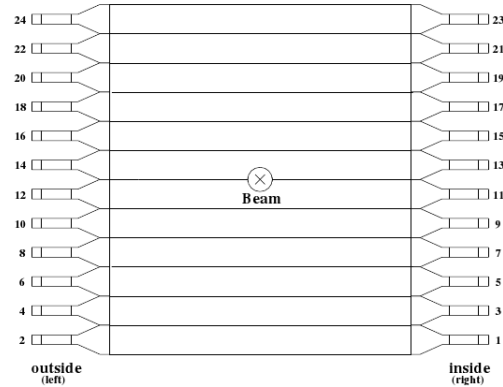


Figure 2.19: The FVH hodoscope: one layer of scintillators.

for a position measurements inside the FRH, it helps to suppress secondary interactions inside the FRH material. More detailed information about the FRI can be found in [42].

2.3.2.6 Forward Veto Hodoscope

The Forward Veto Hodoscope is the last active component in the FD. This is one layer of twelve horizontally oriented rectangular plastic scintillators. Each scintillator is a 20 mm thick and 137 mm wide. The Forward Veto Hodoscope (FVH) is drawn in the figure 2.19. The scintillators are read out from both ends by photomultipliers. The FVH is used in the trigger logic for the registration of punch-through particles and identification of certain undesired reactions.

2.3.2.7 Forward Range Absorber

The Forward Range Absorber is a passive component, placed between the FRH and the FVH. It is made from 5 mm thick iron plates which can be put together and provide a total thickness of 100 mm . The Forward Range Absorber(FRA) is equipped with supporting rails and can be easily moved in or out.

The FRA was designed to stop slow protons from η -production in proton elastic scattering reactions. Fast protons penetrate the FRA and trigger signals in the FVH which can be used for veto in the trigger system.

2.3.3 The light-pulser monitoring system

The light-pulser monitoring system is used for monitoring all photomultipliers in the whole detector. The light pulser provides a reference light pulse for each photomultiplier, which can be used for monitoring its stability. There are two types of light sources: one "slow" source for monitoring of the photomultipliers of the calorimeter and four "fast" LED-based sources for the photomultipliers of the plastic scintillators.

The light pulser monitors the stability of the scintillation counters with a precision $\sim 1\%$, which corresponds to the energy resolution for stopped particles. The system has the possibility to change the intensity of light flashes that also allows to study the calibration and linearity of the detectors. A detailed information about the light-pulser monitoring system can be found in [43].

2.4 Data Acquisition system

The Data Acquisition system (DAQ) is a set of electronic devices that organizes the process of handling and storing of measured variables as digital information.

The DAQ, currently used at WASA, belongs to the third generation of the DAQs developed by Central Institute for Electronics (ZEL) at COSY. It is able to provide a read-out with short dead-times in the order of $20\text{-}30\mu\text{s}$ and, thus, allows the WASA detector to run at high luminosities and high event rates. For details see [44].

An overview of the DAQ system developed for WASA is shown in figure 2.20. The analog signals from the detectors are processed through the preamplifiers, discriminators and splitters and transformed into digital signals by TDCs and QDCs⁵. TDCs and QDCs are continuously digitizing and storing the signals in internal buffer. This allows trigger delays up to $2\mu\text{s}$ and avoids delaying the data signals. The plastic scintillators provide both time and amplitude information and are read out by TDC and QDC modules. The straw tube detectors provide time information only and are read out by TDC modules. The TDC and QDC modules are organized in LVDS crates, each crate is equipped with a system controller for the communication between the crates and the readout computer farm, see figure 2.20. All data are collected by an event builder and finally stored on disc. The design of the DAQ allows data rates of $\approx 80\text{ MB/s}$.

⁵Time- or Charge-to-Digital Converter

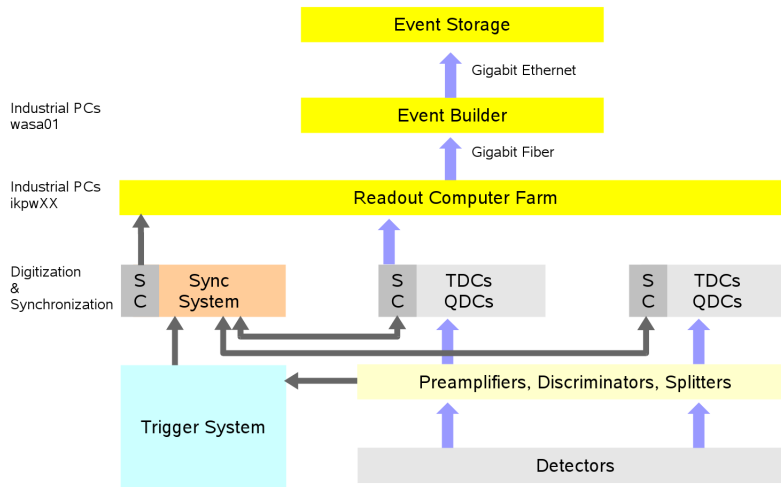


Figure 2.20: The scheme of the DAQ.

2.5 Trigger system

The goal of the trigger system is to reduce the initial amount of events by selecting those that satisfies the experimental interests. The trigger system of WASA is drawn schematically in figure 2.21. In general, the triggers can be divided into *fast* and *slow* triggers. Fast triggers are produced by the plastic scintillators from all over the setup. This type of trigger is based on hit multiplicities of detector layers, their coincidences, cluster multiplicities and track alignment in the forward detector. The slow triggers use the information from the SEC: cluster multiplicity and energy deposits in the crystals (e.g. so-called energy-sum trigger).

Following the scheme in the figure 2.21, the multiplicity signals are matched and then combined into more complex trigger expressions. Depending on the frequency of the triggers they can be prescaled in order to balance the event rate.

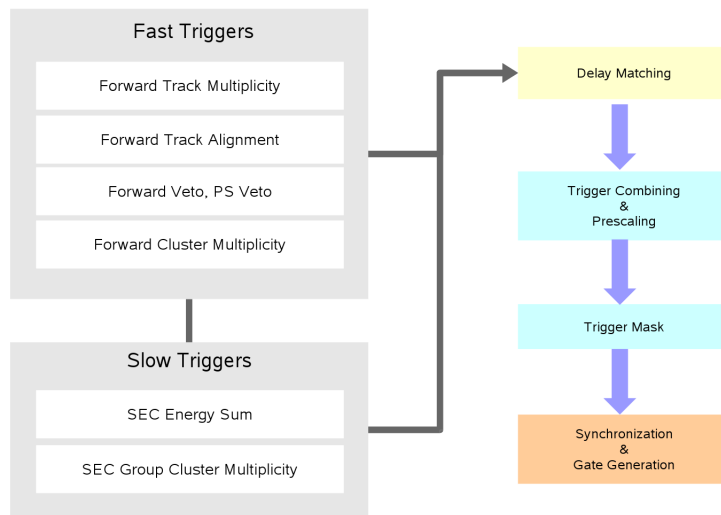


Figure 2.21: The schematic drawing of the trigger system.

Chapter 3

Data Analysis

The data analysis includes the decoding of the digitized information, calibration of the detectors, track reconstruction and comparison the experimental data with simulations. The data analysis is implemented using the software package RootSorter (see Section 3.1), based on ROOT [45] - a technique for scientific programming. The sketch of the data analysis chain is depicted in figure 3.1.

Following the scheme from the top, there are two possible inputs for RootSorter: experimental data as they come from the data acquisition and simulation. In case of simulations the desired reactions are generated using the event generator Pluto. Then the generated events are tracked through the detector setup, described by a GEANT3 based on Monte Carlo simulations.

Simulations are always necessary for evaluation of experimental data. The study of the rare processes requires large event samples in order to develop the analysis methods by considering the kinematics of the process and the detector response.

This chapter will cover the tools that were used for simulation and for data analysis, as well as the calibration procedures for the central detector components, focusing on the Mini Drift Chamber. In addition the track reconstruction in both parts of the WASA setup will be discussed. The relevant plots of the particle identification are shown for $pd \rightarrow {}^3\text{He}\eta$ at 1 GeV .

3.1 Software Tools

3.1.1 Event Generator Pluto++

An event generator is used to get correctly determined sets of Lorentz-vectors for a given physics reaction. Pluto is an event generator entirely based on the ROOT software package and designed for hadronic interactions like meson pro-

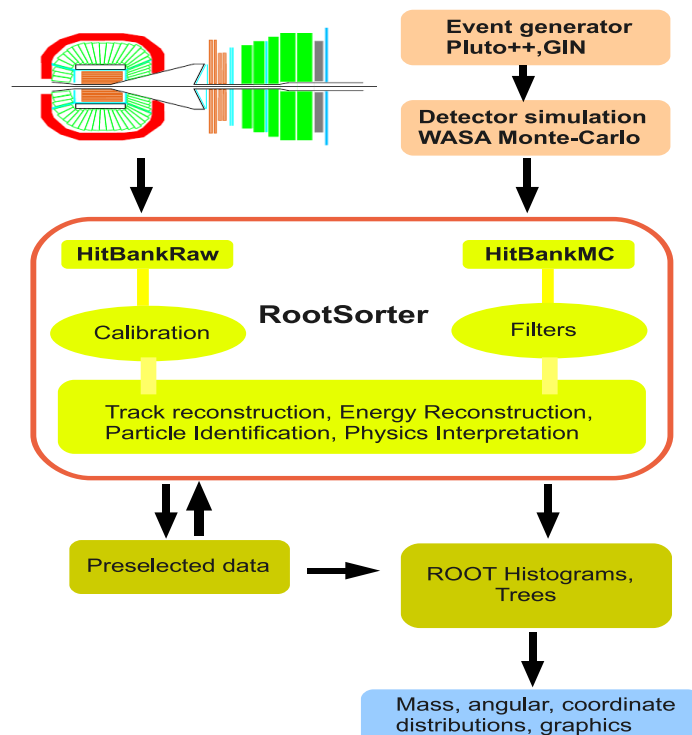


Figure 3.1: Schematic drawing of the data analysis chain.

duction at threshold up to intermediate energies of a few GeV . Initially, the package had been designed for the physics program of the HADES [46]. However, its flexible user-interface can easily be changed to suit other experiments and various models can be included, like the Vector Meson Dominance Model.

In the following the basics for the event generation of the decay $\eta \rightarrow e^+e^-e^+e^-$ is described. For pseudoscalar meson Dalitz decays the mass dependence of the Dalitz-decay width is given by [15]:

$$\frac{d\Gamma^k(m)}{\Gamma^{A \rightarrow 2\gamma} dm} = \frac{4\alpha}{3\pi m} \sqrt{1 - \frac{4m_e^2}{m^2}} \left(1 + \frac{2m_e^2}{m^2}\right) \left(1 - \frac{m^2}{m_A^2}\right) |F_A(m^2)|^2 \quad (3.1)$$

Formula 3.1 describes the mass sampling for virtual photons, where index A refers to the parent meson (e.g. η), m is the dilepton mass, m_e is the electron mass and m_A is the meson mass. The last factor is the parent form factor. In the first approach for η meson this form factor was taken as one-pole approximation:

$$F_A(m^2) = \frac{1}{1 - \frac{m^2}{\Lambda^2}} \quad (3.2)$$

where $\Lambda = 0.75 GeV$ is used according to Vector-Meson-Dominance-Model calculations. Experimental measurements yield $\Lambda = 0.72 \pm 0.09 GeV$ based on the single Dalitz decay $\eta \rightarrow \mu^+\mu^-\gamma$, [29]. Both results from theory and experiment indicate that the interaction between mesons and virtual photons proceeds via an intermediate ρ -meson.

Similarly, the double Dalitz decay of the η meson can be generated. In this work, the influence of the form factor was neglected: $F_A(m^2) = 1$, because of the poor statistics of the experimental data. As it was shown in figure 1.4 the form factor influences the region of high lepton pair masses, while in the region of low lepton pair masses the influence is small. The interference between leptons, discussed in 1.3 is not considered either. In this work, the simulation of the background channels was performed using the Pluto version 5.31.

3.1.2 Detector Simulation Monte Carlo Package

The simulation of the WASA detector is done with a Monte Carlo package, based on the GEANT3 software [47]. The main purpose of the Monte Carlo software package is the study of the detector response for different physical processes. The simulation tool reproduces the properties of the experimental setup as close as possible to reality including the construction of the setup, the material properties of the detector components together with the supporting mechanics and particle interaction with the detector material. Additional effects are implemented via

Monte Carlo smearing filters, based on the experimentally measured values. These filters consider such processes like electronic noises, light propagation or the drift of electrons in gas volume. The magnetic field is included as a three-dimensional distribution coded in a field map.

The events provided by the event generator serve as an input for the Monte Carlo software. Each event is defined as a set of Lorentz vectors, which correspond to the particles from the physical reaction. The particles interact with the detector material and the initial values of the parameters change. The Monte Carlo simulation covers the following important effects of particle interaction with detector material: photon interaction with matter (Compton scattering, generation of e^+e^- pairs, photoelectric effect), Coulomb multiple scattering, positron annihilation, hadronic interaction with secondaries, energy loss, quenching effects.

The output of the Monte Carlo simulation contains the initial parameters of the particles (as generated by Pluto) as well as the energy deposits and time information from all detector components. It allows us to study the detector response and efficiencies. Apart from the external input (i.e Pluto) there is a possibility to generate single track events inside the Monte Carlo package for detailed studies of the detector.

3.1.3 RootSorter Software Environment

The RootSorter framework is written in the C++ programming language and based on ROOT [45]. It provides the necessary classes for low level data analysis, for monitoring during data taking as well as for high-level physics analysis. The entire package for the WASA-at-COSY detector is under development since 2005.

RootSorter is organized in analysis modules, each module is represented by group of classes performing certain steps in the data analysis: from decoding to particle track reconstruction. The modular software allows to add new modules without modification of the entire package.

The data can be classified into information units: hits, clusters (group of hits) and the tracks. These units are stored in the appropriate containers (banks). A hit is the response of an individual detector element (signal from single readout channel). A cluster is a combination of hits from the same detector. Tracks of the particles can be reconstructed by matching the clusters from the different detectors. In fact, a cluster from a single detector can also be called a track, e.g. a neutral cluster in the electromagnetic calorimeter or a charged cluster in the drift chamber. The whole procedure of data processing can be described as follows: after decoding of the information from the data stream RootSorter first fills the raw hit banks. Then the raw hits are calibrated and stored into calibrated hit banks. Dedicated analysis modules - *the cluster-finders* - build the clusters from the calibrated hits and fill the cluster banks. Afterwards, *the track-finders* build tracks out of the

clusters. In case of Monte Carlo simulations, the calibration stage is replaced by filters, which take into account gates and thresholds for time and energy as well as additional smearing.

The standard analysis modules (decoding, calibration, track reconstruction) and the raw analysis modules are the part of the software package. The high level analysis has to be developed by the individual user. The data analysis was done with the RootSorter version 3398 and ROOT version 5.24.

3.2 Calibration

A calibration of a detector is a transformation of measured digitized signals back into physical variables. For the WASA detector there are different calibrations: time and energy.

3.2.1 Calibration of Straw Tube Detectors

Calibration method

The currently used calibration method for the straw tube detectors is based on the integration method, described in [48]. This method determines the relation $R(t)$ between drift time and drift distance. It is based on the following assumptions:

- the tube works with 100% efficiency without noise, it implies that all measured times correspond to correct drift distances,
- the track distribution $\frac{dn}{dr}$ along the tube radius is uniform: $\frac{dn}{dr} = const = \frac{N_{total}}{R_{tube}}$, where N_{total} is the total number of registered tracks, R_{tube} is the tube radius corresponding to the maximum drift distance.

The drift velocity can be calculated:

$$V(t) = \frac{dr}{dt} = \frac{dn}{dt} \frac{dr}{dn} = \frac{R_{tube}}{N_{total}} \frac{dn}{dt}, \quad (3.3)$$

The drift distance is expressed by integral of the equation 3.3 over time:

$$R(t) = \frac{R_{tube}}{N_{total}} \int_0^t \frac{dn}{dt} dt \quad (3.4)$$

where t is the drift time of the track inside the tube.

Calibration procedure

The mini drift chamber calibration is based on the drift time measurement which is later converted into drift distances. The calibration is a two-stage procedure. The first step is the T_0 determination, i.e. the time alignment of all straw tubes

relative to the main trigger signal. The second step is a determination of the *time-to-distance relation*, i.e. a transformation of drift time into the distance inside the individual straw tube. As an input for calibration serves the time in units of the TDC-channels delivered from the raw hit bank. The output of the calibration procedure are two tables: the first one contains the T_0 constant for each tube, the second one contains the parameters for the calculation of the distance. The calibration procedure must be performed for stable operational conditions (high voltage, thresholds on electronics, gas mixture) and repeated in case of any changes of electronic modules or cables.

The time is measured relatively to the trigger signal which may vary event by event, therefore, only events from one specific trigger are selected. An ideal reaction for the mini drift chamber calibration (and for the plastic scintillator barrel as well) is inelastic proton-proton scattering: $pp \rightarrow d\pi^+$ at 600 MeV . It provides one charged particle in the central detector (π^+) and one charged particle in the first plane of the forward range hodoscope (d). The reaction can be tagged by using the angular correlation of the two-body process. The remaining background has an almost flat shape which can be easily subtracted during the time-to-distance parameterization.

Time alignment. The typical raw time spectra for the mini drift chamber are shown in figure 3.2. The time is measured individually for each tube and runs from right to left (common stop mode). As a reference position for $T_0 = 0$ on the raw time spectra the wire position is selected (marked in red), which defines the individual time offset for a straw tube. These time offsets are determined by fitting of the raw spectra from each straw tube by a Fermi function given by:

$$f(x) = P_3 + \frac{P_2}{1 + e^{\frac{x-P_0}{P_1}}} \quad (3.5)$$

The greatest value at 20% of the maximum of time spectrum and the parameter P_3 of the Fermi function are selected as individual time offset. A corresponding table is filled with the acquired time offsets.

Time-distance parameters. After the determination of T_0 and the time alignment the second step is the extraction of the time-distance parameters, which convert the drift time into the drift distance inside the tube. Based on the cylindrical symmetry of the chamber the time-to-distance parameters are calculated individually for each layer. As discussed in section 2.3.1.1 one of the features of the used gas mixture is its linearity - it provides a constant drift velocity along the radius of tube. Therefore, in the first approach, only one parameter is used to describe the time-distance relation: the drift velocity.

There are two general steps to extract this parameter: subtraction of the background and integration of the time spectra. Fermi and reversed Fermi functions

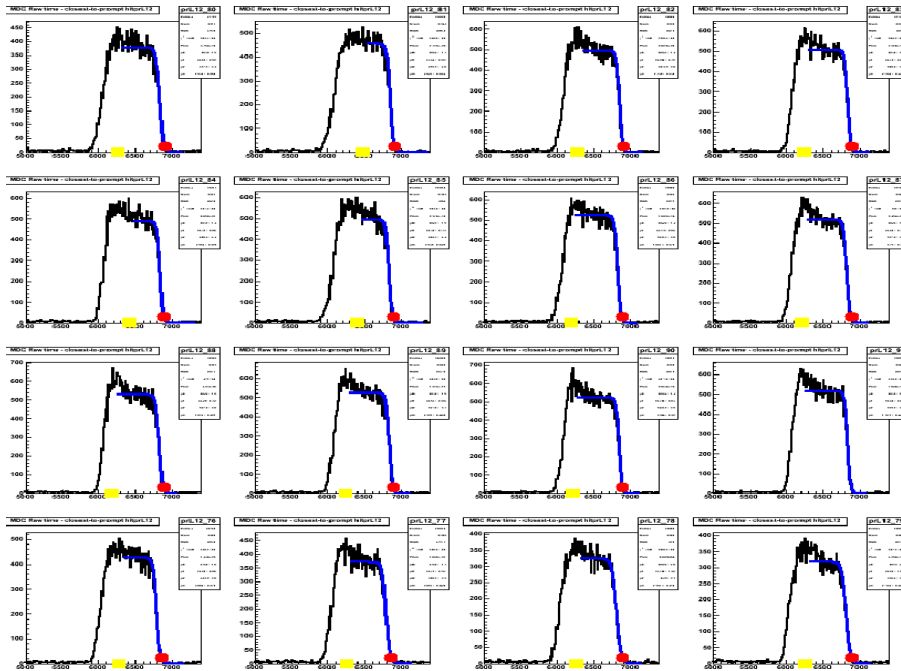


Figure 3.2: Raw time spectra from the individual straw tubes of the mini drift chamber are fitted with a Fermi function. The time corresponding to the wire position is marked in red. The maximum of the time spectra is marked in yellow. The data are from the reaction $pp \rightarrow d\pi^+$ at a proton beam energy of 600 MeV from April 2008.

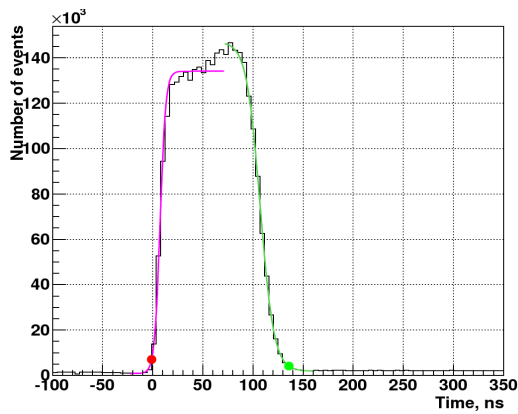


Figure 3.3: Calibrated time spectrum: the wire position is marked in green, the wall position is marked in red.

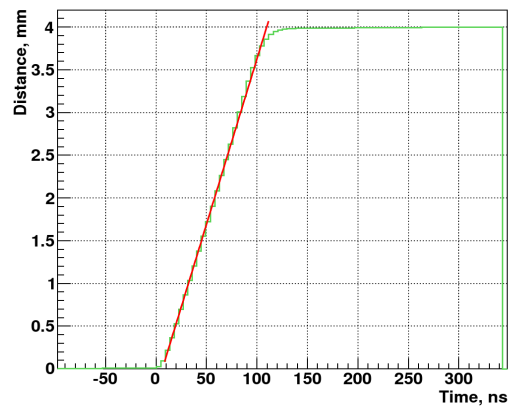


Figure 3.4: Drift function for the tubes with 8 mm diameter (green line) and linear fit (red line).

were used for fitting and defining lower and upper boundary: the wire and the wall position. The limits of the drift region are marked in the figure 3.3.

Using the integrated time spectra one can obtain the drift function for each layer. As shown in figure 3.4, the drift function is linear in a wide range, a deviation occurs only in the region very close to the wall of the tube, which is due to detection inefficiencies of the tube itself.

Finally, two tables with constants describe the calibration of the mini drift chamber: the individual time offsets for each tube and the time-distance parameters for each layer.

A new generation of the Mini Drift Chamber calibration procedure was performed in May 2009, as an extension of the existing one. It includes the time-distance relation individually for each tube and stores the complete shape of the drift function. Furthermore, the time alignment of the tubes is done relatively to the time of the plastic scintillator barrel. These changes make the calibration more precise for drift distance determination.

3.3 Charged Track Reconstruction

The track reconstruction is one of the last stages in the analysis chain and the very first step in the physics interpretation of the data. The track of the particle is reconstructed from the clusters of different detectors. The detector clusters are merged together by checking the geometrical overlap of hit elements and their timing. The allowed overlap regions and time windows are defined in input files and can be tuned in order to achieve optimal conditions. The cluster and track finding procedures differ depending on the detector geometry and type.

There are two categories of charged tracks: charged tracks in the central detector and charged tracks in the forward detector. Charged tracks in the central detector at least require a plastic barrel cluster and a mini drift chamber cluster or calorimeter cluster. The calorimeter cluster is optional and will add energy information for the track. In this work the charged track in the central detector must contain the mini drift chamber cluster and plastic barrel or calorimeter cluster. The mini drift chamber participation, providing the momentum of the track, is a must for a four-vector reconstruction.

Charged tracks in the forward detector must contain at least one cluster in any of the forward scintillators. The neutral tracks in the forward detector are defined as not containing clusters in the thin forward scintillators, but a cluster in the forward range hodoscope planes. In the context of this work only charged tracks in the forward detector are used.

3.3.1 Central Detector

The track finding in the central detector is based on matching the clusters provided by each component: mini drift chamber, plastic scintillator barrel and calorimeter. Each of the component is a different type of the detector and there are separate track finding procedures.

3.3.1.1 Hit Clustering in the Mini Drift Chamber

The charged track reconstruction in a magnetic field is one of the difficult tasks in experiments. The track reconstruction in the MDC is divided into two steps: the pattern reconstruction and the full fitting. The pattern reconstruction works with hit patterns and provides first particle trajectories. The track parameters found by it serve as an input for the full fitting. The full fitting is intended to refine the track-helices provided by the pattern reconstruction.

Currently, three pattern reconstruction algorithms are available: *Dubna-algorithm* (historical title), *Spanning Tree* and *Simple*. The Dubna-algorithm routine can be implemented for any tracking device with a cylindrical geometry. The full fitting is more specific for the detector and was adapted for the WASA setup.

The Pattern Recognition

The pattern recognition performs the recognition of hit patterns by fitting helices. The algorithm assumes a homogeneous magnetic field inside the mini drift chamber parallel to the Z -axis and describes the particle tracks as regular helices with an axis also parallel to the Z -axis, see figure 3.5. The helix is described by six parameters:

- R_0 - the distance in XY-plane from the helix axis to the origin,
- Φ_0 - the azimuthal angle of the helix axis in XY-plane,
- R - the radius of the helix,
- Q - the charge of the particle, determined from the direction of curvature,
- θ - dip angle giving the inclination of the tangent with respect to the XY -projection,
- z_0 - the z -coordinate of the closest approach of the helix to the origin.

The parameters are illustrated in figure 3.6. The algorithm fits the helices to the hit patterns by applying multi-model regression methods. First, the tracks are treated as projections onto the XY-plane, where the drift distances are used for minimization of the weighted sum of the distances to the center of each circle. At this step the information only from the axial layers is used.

After the circle is identified the following parameters are fixed: Φ_0 , R_0 , R and Q . The helix 3-D ambiguity will be solved after using the Z -information from

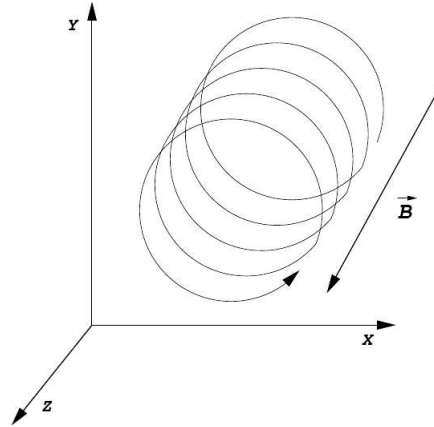


Figure 3.5: The trajectory of the charged particle reconstructed by the pattern recognition as a regular helix with axis parallel to the Z-axis of the WASA coordinate system. Taken from[31].

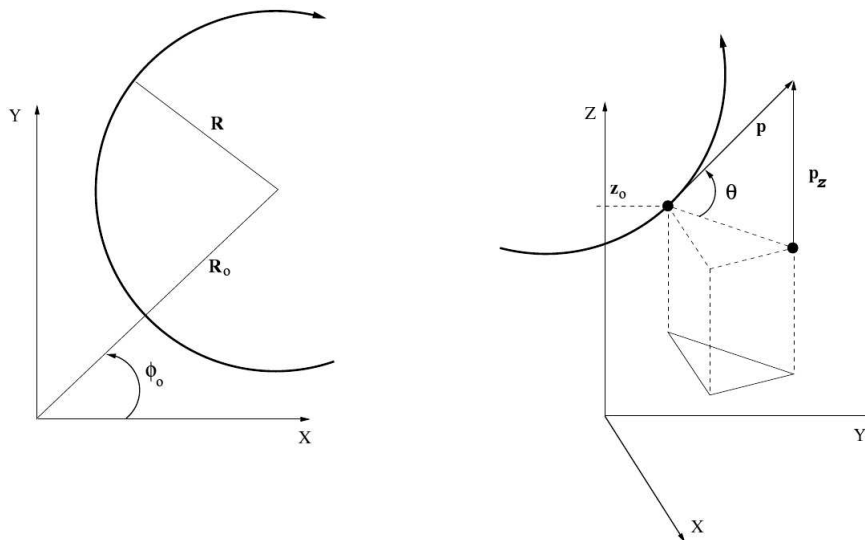


Figure 3.6: Depiction of the helix parameters. Left: R_0 , R and Φ_0 parameters of the circle in the XY-plane, the direction of the circle is defined by the charge Q . Right: 3-D picture of the z_0 and θ parameters. Taken from[31].

stereo layers. The coordinates of the closest point of the track with respect to the inclined tube axis can be found. The same multi-model regression methods, as in the XY-plane, are used in order to find the last two parameters: z_0 and θ .

Thus, the half-helix is described by the following equations:

$$z = z_0 + \frac{R}{\tan(\theta)} \arccos\left(\frac{R_0^2 + R^2 - r^2}{2R_0R}\right) \quad (3.6)$$

$$\phi = \phi_0 + Q \arccos\left(\frac{R_0^2 - R^2 + r^2}{2R_0r}\right) \quad (3.7)$$

where the r is the distance in XY -plane from the origin, point $(0,0,0)$, to given helix point, ϕ is azimuthal angle of this point. More details can be found in [51]:

The Full Fitting

The tracks found by the pattern recognition are reconstructed with limited precision due to the several model assumptions (uniformity of the magnetic field, the track was approximated by a helix). The helix parameters can be further improved by including important physical effects: the nonuniformity of the magnetic field, energy loss and multiple Coulomb scattering. This is done by the full fitting. It does not only provide track parameters but also their covariance matrix.

By applying a Kalman filter [52] the tracks can be traced back from the outer layers to the beam axis to search for vertices. The Kalman filter method provides a successive and efficient way to estimate the state vector of a process by minimizing the mean of the squared error. The filter uses the measurements containing noise (random variations) and other inaccuracies. The main steps in the Kalman filter algorithm are: prediction, correction and smoothing. In case of the full fitting program, the state vector is defined by 3.8, which is updated by the filter.

$$T = \left\{ \frac{q}{p}, \lambda, \phi, d_0, z_0 \right\} \quad (3.8)$$

where $\frac{q}{p}$ is a signed curvature, λ is the dip angle, ϕ is the azimuthal angle, d_0 is the shortest distance to z -axis and z_0 is the z -coordinate at that point.

Following the track points, the parameters of the trajectory are progressively improved by adding new information at each measurement point. A more detailed description of the Kalman filtering method can be found in [53], [54].

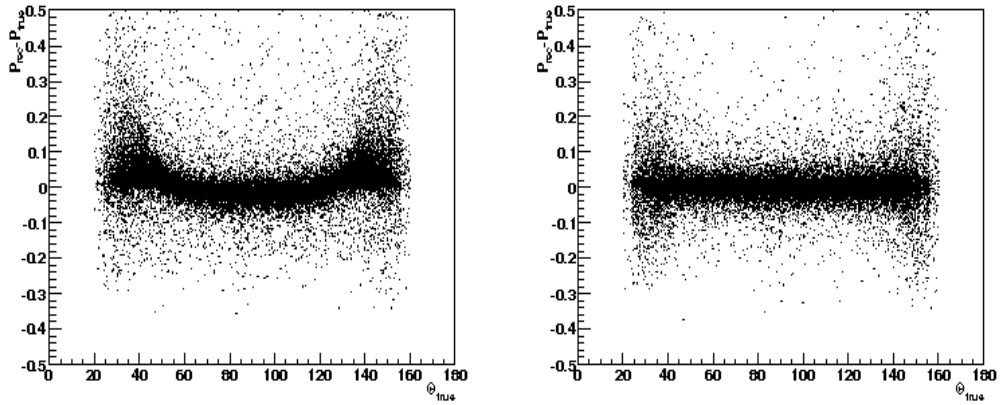


Figure 3.7: Monte Carlo studies based on single electron events: the difference between the reconstructed momentum and the true momentum plotted versus the scattering angle. Left: Pattern Recognition, right: Full Fitting. The effects at the low and high angles are due to the nonuniformity of the magnetic field which are corrected by using the Full Fitting.

Performance of the Track Finding Routines

After processing the tracks in the full fitting procedure the particle trajectories are no longer the regular helices but curling helices. The parameters of the trajectories are changed which leads to a different momentum reconstruction by pattern recognition and full fitting. Qualitatively, the effect is shown in figure 3.7, where simulated single electron events were studied. The electrons were simulated in the energy range of $(20,500) \text{ MeV}$ and the scattering angle range of $(20^\circ, 170^\circ)$. As it can be seen on the left panel, where the reconstructed momentum is provided by the pattern recognition, there is a systematic shift at the side regions where the magnetic field is most nonuniform, while in the right panel, where the momentum was reconstructed by the full fitting, the shift is gone.

As any fitting routine the full fitting must have certain operation parameters, they are the spatial resolution and the mass of the particle. In the frame of this work the mass of an electron was used as the mass parameter in all analysis steps. The effects of using different spatial resolutions on the momenta resolution are shown in figure 3.8. In the left panel the momentum resolution as a function of particle momentum is shown. In the right panel the momentum resolution as a function of scattering angle is shown. As it can be seen, a smaller spatial resolution provides the higher momentum resolution. The common behavior of the momentum resolution for small and large scattering angles is due to the geometry: the lower number of the layers participating in the track reconstruction at low and high scattering angles, resulting into a smaller number of measuring points and,

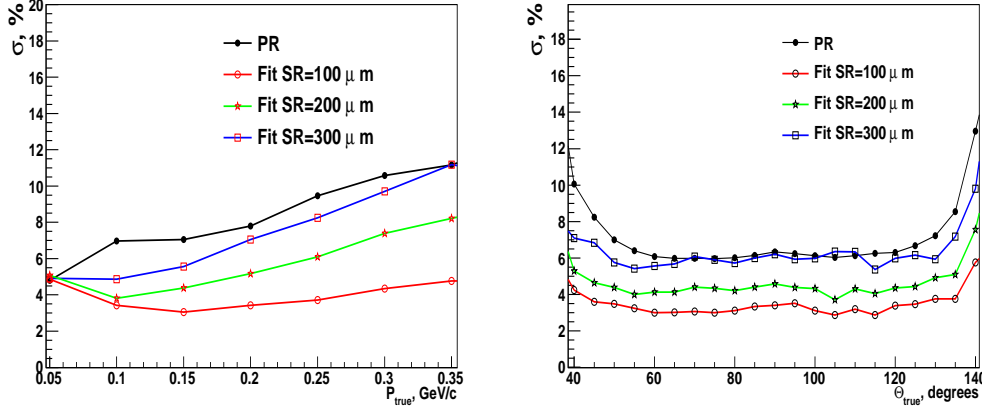


Figure 3.8: Left: Relative momentum resolution (Y-axis) as a function particle momentum (X-axis). Right: and as a function of scattering angle, right panel. The influence of the different spatial resolution on the momentum resolution for single electron events: the black line represents the Pattern Recognition results, the colored curves are the Full Fitting results with different hypothetical spatial resolution. a) the relative momentum resolution as a function of momentum b) the momentum resolution as a function of scattering angle

thus, into a worse resolution.

The real spatial resolution can be obtained from the best agreement of simulated and experimental data analyzed with different spatial resolutions. By studying the residual distributions defined as the difference between measured drift distance and the true distance of the fitted track to the wire of the straw tube, the optimal spatial resolution was found as $325 \mu m$ in [41].

The comparison of different pattern recognition algorithms is shown in figure 3.9. The studies are based on single tracks of electrons. The pattern recognition Simple is based on the information from axial layers of the drift chamber, while others use the full 3-D information, and, therefore, the pattern recognition Simple can not be compared with the Dubna and Spanning Tree algorithms. The Spanning Tree can be used both for straight (without magnetic field) and curved (with magnetic field) tracks. It uses *line* and *circle* models. The efficiencies of both algorithms turn out to be similar: the Dubna-algorithm has systematically lower efficiency by $\sim 5\%$ than the Spanning Tree, however the analysis speed is slower in case of the Spanning Tree. The efficiency as a function of momentum and scattering angle is shown in figure 3.10. The regions of lower efficiency are visible for low and high scattering angles. The effect is explained by reduced number of the layers contributing to the tracks with such scattering angles, the same as for the momentum resolution, see figure 3.8.

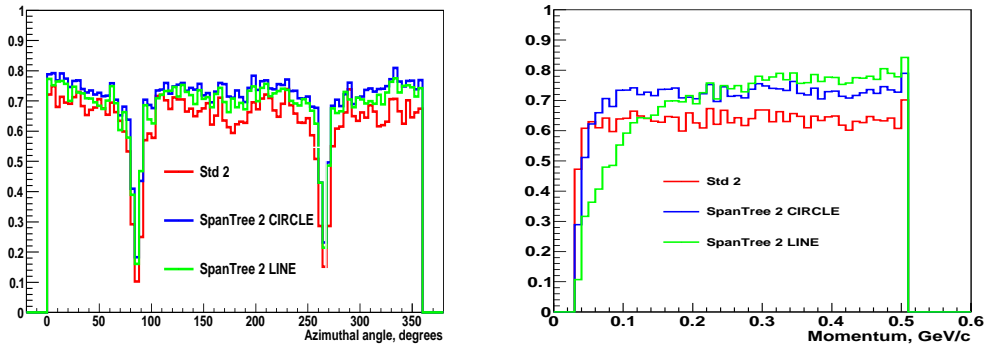


Figure 3.9: Monte Carlo studies based on single electron events, the red curve represents the Dubna algorithm, blue - Spanning Tree with a circle, green - Spanning Tree with a line. Left: efficiency reconstruction as a function of azimuthal angle: two inefficient regions at 90° and 270° are due to the pellet tube. Right: efficiency reconstruction as a function of momentum: the Spanning Tree algorithm with an assumption of straight tracks has significantly lower efficiency for low momenta electrons since such tracks have small radii and the probability to fit them by straight lines is low.

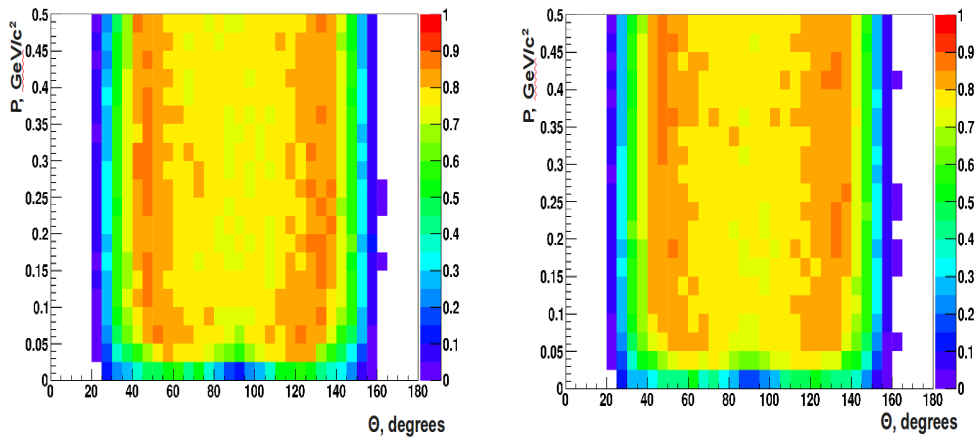


Figure 3.10: Monte Carlo studies based on single electron events: efficiency as a function of momenta and scattering angle of electrons. Left: Dubna algorithm results, right: full fitting results.

3.3.1.2 Hit Clustering in the Plastic Scintillator Barrel

A cluster in the Plastic Scintillator Barrel can be formed by one single hit or by two hits from neighboring elements if the hits satisfy certain criteria: a minimum deposited energy $\Delta E_{min} = 0.5 MeV$ and a time difference between them $\Delta T_{max} \leq 10 ns$. The first hit is assigned to a cluster if the energy deposit is above the minimum deposited energy. The average time of the hits contributing to the PSB cluster defines its time information. The deposited energy of the cluster is taken from the hit with the highest energy deposit.

The angular information delivered by the PSB cluster is unilateral: the azimuthal angle is calculated as the average among the fired elements contributing to the cluster and the polar angle is not determined by the PSB.

3.3.1.3 Hit Clustering in the Calorimeter

A photon and charged lepton reaching the calorimeter produces an electromagnetic shower which is spreading over a group of neighboring crystals. The crystals belonging to the same electromagnetic shower form a cluster. The cluster finding routine is intended to identify these crystals and assign them to one cluster.

The hit with the highest deposited energy is chosen as the center of the cluster. The neighboring crystals checked for associated hits are added if they satisfy timing and energy criteria. The time difference between the central and associated hits has to be less than $50 ns$ and the energy deposit has to be greater than $2 MeV$. In addition there is the requirement for a formed cluster to have a total deposited energy of at least $10 MeV$. The energy of a cluster is taken as the sum of the contributing hits, the time of a cluster corresponds to the time of the hit with the highest deposited energy. The position of the cluster is defined by the weighted sum of the positions of the individual crystals^{3.9}:

$$\vec{X} = \frac{\sum_i w_i \vec{x}_i}{\sum_i w_i} \quad (3.9)$$

where the weights are based on the energy deposits in the crystals:

$$w_i = MAX\{0, W_0 + \ln \frac{E_i}{\sum_i E_i}\} \quad (3.10)$$

Thus, the reconstructed clusters provide a complete information for four-vector of a particle.

3.3.1.4 Track Assignment in the Central Detector

The track assignment in the CD is based on the geometrical overlap of clusters from different components and time coincidence of the clusters from Plastic

Cluster combination	Type	Matching information
MDC, PSB, SEC	charged	$\Delta\phi, \Theta_{PS}, \Delta\Omega, \Delta T$
MDC, PSB	charged	$\Delta\phi, \theta_{PS}$
MDC, SEC	charged	$\Delta\Omega$
PSB, SEC	charged	$\Delta\phi_{PSB-SEC}, \Delta T$
MDC	charged	
PSB	charged	no momentum information
SEC	neutral	

Table 3.1: Tracks in the Central Detector

Scintillator Barrel and Electromagnetic Calorimeter. A charged track consists at least of two clusters from different CD components and a neutral track is defined as a solitary cluster from the Electromagnetic Calorimeter. There are four possible combinations of the CD clusters forming the tracks and three combinations for solitary clusters, summarized in the table 3.1. The first three types of tracks are considered in this work as charged tracks and the neutral track is defined as a solitary cluster in Electromagnetic Calorimeter.

The CD track finder operates on the cluster banks from the CD subdetectors. The matching scheme between the clusters is depicted in the figure 3.11: the cluster parameters used for matching are shown. The first step of the procedure is to check cluster combinations of the Mini Drift Chamber and the Plastic Scintillator Barrel. The condition of their matching is based on the difference of the azimuthal angles $\Delta\phi_{MDC-PSB}$ from cluster of the Plastic Barrel (ϕ_{PSB}) and the exit coordinate of the cluster of the drift chamber ($\phi_{exitMDC}$). The distribution of the difference is shown in the figure 3.12: $\Delta\phi_{MDC-PSB}$ should be smaller than 10° . The condition for polar angles is limited by the Plastic Scintillator geometry: it is checked that the exit coordinate of the MDC track is within the polar angular range of the PSB element.

Afterwards the MDC and PSB clusters are combined with the calorimeter clusters. For this purpose the direction of the track in the drift chamber cluster is extrapolated to the calorimeter by a straight line. The opening angle between the extrapolated position of drift chamber cluster and the calorimeter cluster itself, labeled in the figure 3.11 as Ω , is used for evaluation: figure 3.13 shows that the opening angle has to be smaller than 20° .

The matching of the Plastic Scintillator clusters with the calorimeter clusters is based on a twofold comparison: the difference of the azimuthal angles and the time difference of the clusters. Figure 3.14 shows both distributions where a maximum difference of azimuthal angles is 20° and a maximum difference in time was taken

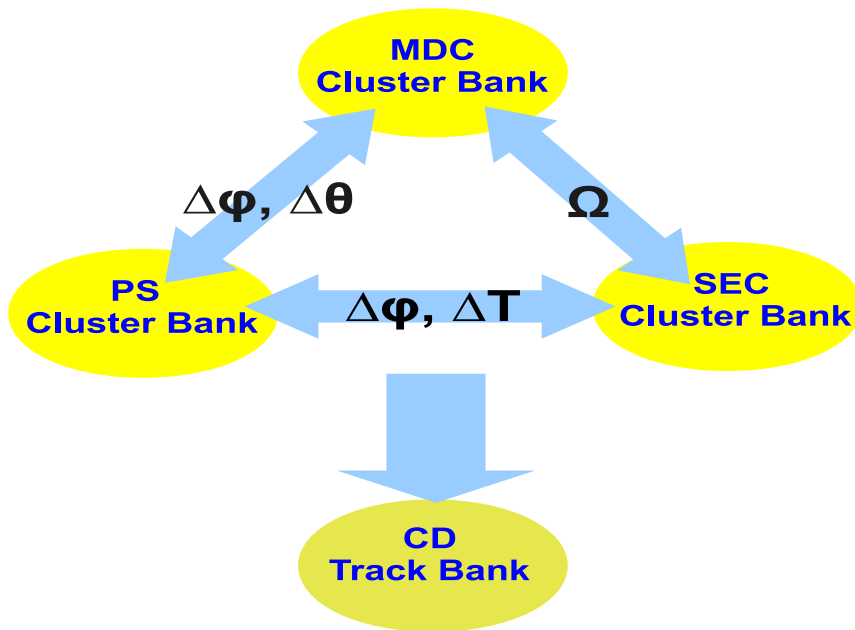


Figure 3.11: Matching scheme between the cluster banks during track reconstruction in the Central Detector.

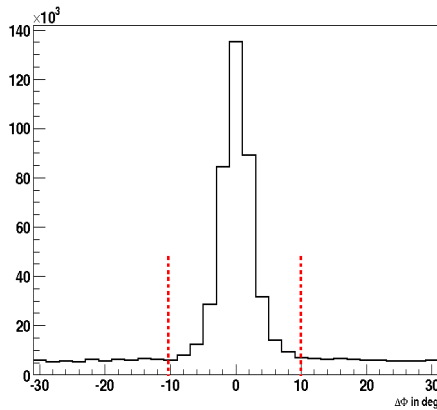


Figure 3.12: The experimental difference between the azimuthal angles of the exit coordinate of the drift chamber cluster and the azimuthal angle of the Plastic Scintillator cluster. The red dotted verticals represent the maximum allowed difference of 10° .

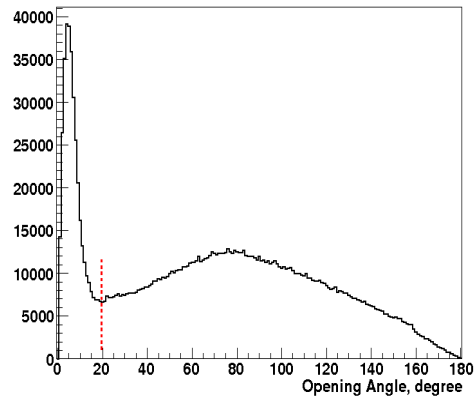


Figure 3.13: The experimental distribution of the opening angle between the extrapolated drift chamber cluster and the calorimeter cluster. The condition for merging is shown by red vertical: $\Omega \leq 10^\circ$.

as 35 ns . All distributions are based on data from the beamtime in September-October, 2008 for $pd \rightarrow {}^3\text{He}\eta$ reaction at 1 GeV .

Thus, in the first step of the track reconstruction all drift chamber clusters have been merged with the clusters of the Plastic Scintillator and/or the calorimeter, or were identified as solitary tracks. In the second step the remaining Plastic Scintillator clusters are checked with the calorimeter clusters. Neutral tracks are identified as remaining calorimeter clusters.

The conditions for track assignment have to be checked for each beamtime period individually, since the calibrations may change the detector response.

3.3.2 Forward Detector

The track reconstruction in the Forward Detector is based on matching of clusters from hits in neighboring elements of each subdetector layer. The clusters are found by time coincidence and position of the hits. The average of the time and angular information from the hits define the cluster. The energy of the cluster is the sum of the energies from the hits contributing to it. Single hit is assigned to cluster if it has energy deposit above threshold.

The basis for the charged track reconstruction is the Forward Trigger Hodoscope due to its special geometry resulting in a pixel structure, see Section 2.3.2.3. The FTH elements are checked for a geometrical overlap of hits in all

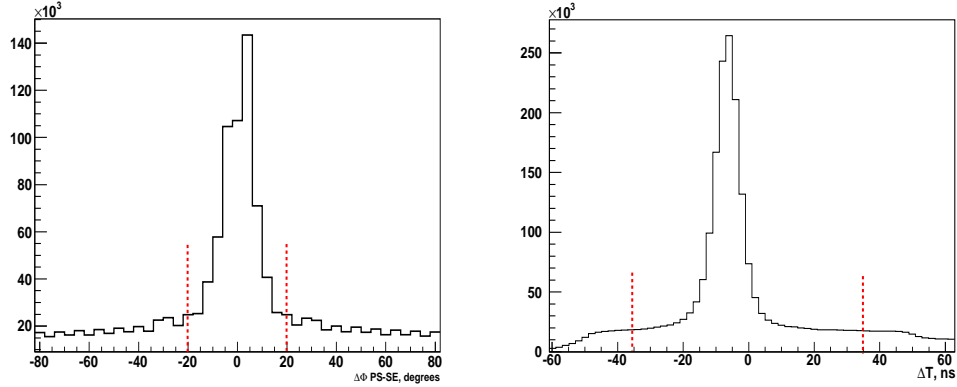


Figure 3.14: Experimental distributions of the difference between azimuthal angles of the Plastic Scintillator and the calorimeter clusters (left) and their time difference (right).

three layers. The overlapping elements are combined into pixels which define a track. Such tracks contain a rough angular information, assuming the interaction point as one belonging to the track. At this stage the angular information from the Trigger Hodoscope can be refined by involving the Forward Proportional Chamber. Due to the high granularity of the wire chamber the angular resolution can be improved.

Subsequently, the track finding routine searches in the Window Counter, the Range Hodoscope and the Veto Hodoscope layers for clusters. These clusters are checked for an azimuthal overlap, a small time difference and a minimum deposited energy.

3.4 Particle Identification

The particle identification in WASA is based on $\Delta E - E$ or $\Delta E - P$ techniques, governed by the Beth-Bloch formula [55]. The $\Delta E - E$ method implies the correlation of the deposited energy and full (kinetic) energy of charged particles by different scintillator detectors. The $\Delta E(E) - P$ method is used when measuring charged particles in a magnetic field: the deposited or full energy of the particle measured by a scintillator detector or a calorimeter is plotted versus the momenta provided by a tracking device.

3.4.1 Charged Particles in the Central Detector

A particle in the Central Detector is identified by its momentum and energy deposit in the plastic scintillator or calorimeter. The combination of all three com-

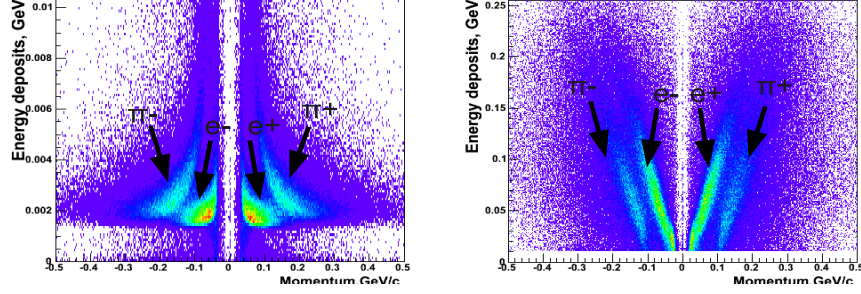


Figure 3.15: Monte Carlo simulation of $\eta \rightarrow \pi^+\pi^-e^+e^-$ decay in the reaction $pd \rightarrow {}^3\text{He}\eta$ at 1 GeV. Identification of electrons and pions in the Central Detector. On the Y-axis of the left panel is energy deposited in the Plastic Scintillator(central part), on the Y-axis of the right panel is the energy deposited in the calorimeter, on the X-axis of both panels is the momentum in GeV/c units multiplied by charge of particle.

ponents provide three possible correlation plots for particle identification:

- energy deposit in the plastic scintillator correlated with the momentum from the drift chamber, $\Delta E - P$ method
- energy deposits in the calorimeter correlated with the momentum from the drift chamber, $E - P$ method
- energy deposit in the Plastic Scintillator correlated with the energy deposit in the calorimeter, $\Delta E - E$ method

The first two identification methods allow us to distinguish between electrons and pions and their charge state. The simulated decay channel $\eta \rightarrow \pi^+\pi^-e^+e^-$ was used for demonstration. As it can be seen from the left panel of figure 3.15, the bands of leptons and pions start to overlap at momenta $0.12 GeV/c$. At this momentum region the second method can be used, involving energy deposit in the calorimeter (the right panel of the figure 3.15). Charged leptons deposit their total energy in the calorimeter resulting in a linear correlation of momentum and deposited energy. The pions as hadrons do not produce electromagnetic showers like electrons and positrons and deposit only part of their energy (the lower bands in the right panel of the figure 3.15).

In case of experimental data such plots are less illustrative as pions are dominating. In the figure 3.16 the same plots as in the figure 3.15 are shown based on the experimental data: exactly two positively and two negatively charged tracks were selected and their energy deposits in the Plastic Scintillator and calorimeter

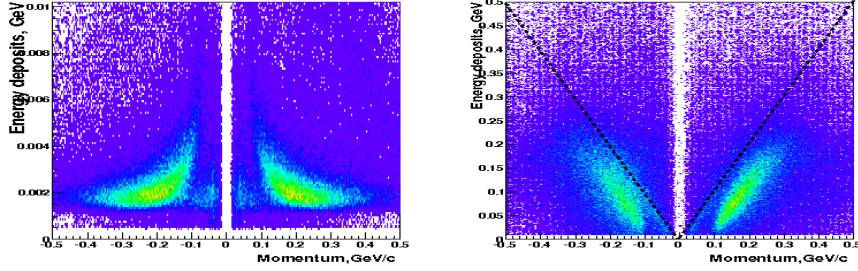


Figure 3.16: Experimental data: energy deposited in the central part of the Plastic Scintillator versus momentum on the left panel and energy deposited in the calorimeter versus momentum on the right panel. The dotted lines on the right panel represent the linear correlation between energy and momentum, which is a characteristic of electrons and positrons. There are hardly visible structures following the lines corresponding to electrons and positrons bands.

were plotted versus their momentum from the drift chamber. The pion bands are significantly pronounced and overshadow the bands of electrons and positrons. Analogical plots are shown in figure 3.18 under more stricter conditions: the invariant mass of both hypothetical lepton pairs (a pair of tracks with opposite charge) were required to be smaller than $0.1 \text{ GeV}/c^2$ - this condition rejects the pion contribution significantly, as it will be discussed in the section 4.6. The lepton bands become more pronounced although with poor statistics. Particle identification plots for single Dalitz of η are shown in the figure ?? under the final cuts for the decay products: the invariant mass of lepton pair is smaller than $0.1 \text{ GeV}/c^2$, the missing mass of the decay products in the interval $2.6 - 2.9 \text{ GeV}/c^2$ and the missing mass of ${}^3\text{He}$ is in the interval $0.535 - 0.560 \text{ GeV}/c^2$.

The third identification method does not involve the Mini Drift Chamber and is, therefore, momentum independent. This method is effective for separation of particles which deposit far different energy in the plastic scintillator and calorimeter in order to provide as much as possible distanced particle bands.

3.4.2 Charged Particles in the Forward Detector

The particle identification in the Forward Detector is based on the $\Delta E - E$ technique. A variety of scintillator counters in different geometries and lengths measure the deposited energy as well as the full energy of particles with different masses from pions to ${}^4\text{He}$ -ions. Particle determination is done by comparing the total deposited energy in the Forward Range Hodoscope layers to the partial energy depositions in the thin scintillators of the Forward Detector.

In the figure 3.19 some identification plots are shown for the reactions $pp \rightarrow$

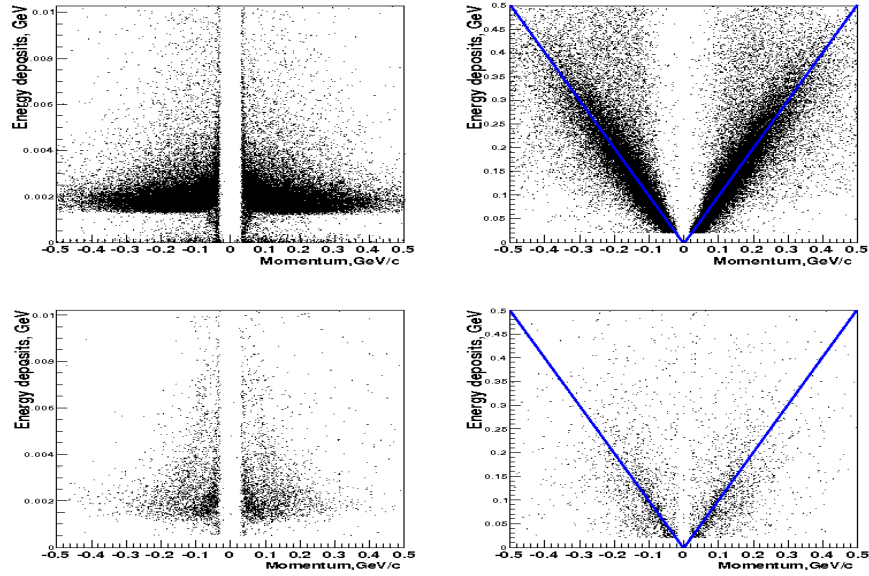


Figure 3.17: Upper row: a Monte Carlo simulation for $\eta \rightarrow e^+e^-e^+e^-$, the lower row: are experimental data showing the whole sample from the beamtime in September-October, 2008.

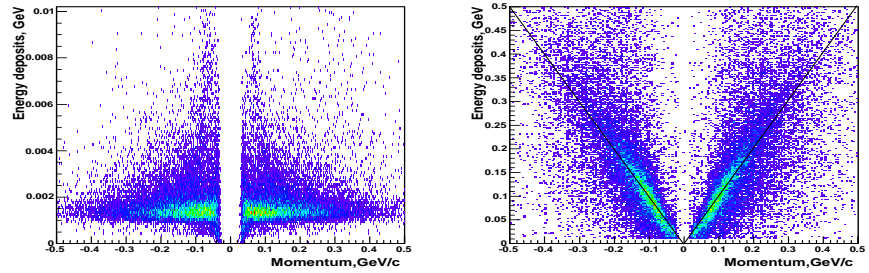


Figure 3.18: Final sample of $\eta \rightarrow e^+e^-\gamma$ in data, whole sample from the beamtime in September-October, 2008.

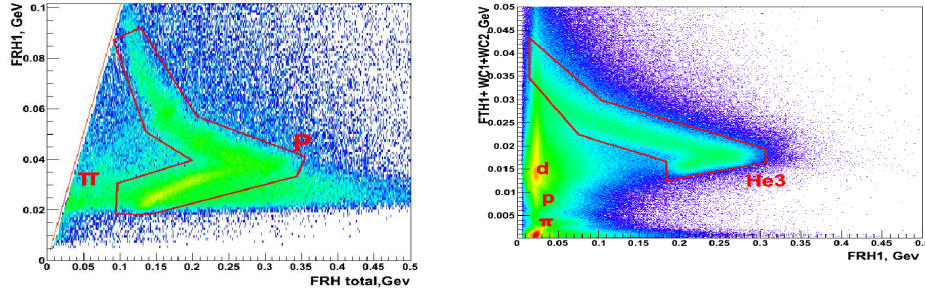


Figure 3.19: Experimental distributions: particle identification in the $pp \rightarrow pp\eta$ reaction at 1.4 GeV (left) and in the $pd \rightarrow {}^3\text{He}\eta$ reaction at 1 GeV (right). On the left panel the correlation between the energy deposited in the first layer of the Range Hodoscope on the Y-axis and total energy deposited in all five layers of the Range Hodoscope is shown. On the right panel other correlation involving sum of energies in the first layer of the Trigger Hodoscope and both layers of the Window Counter versus energy deposited in the first layer of the Range Hodoscope is shown.

$pp\eta$ at 1.4 GeV and $pd \rightarrow {}^3\text{He}\eta$ at 1 GeV. Well distinguished bands of particles are visible, which can be separated by simple graphical cuts (shown by red contour), or by more sophisticated methods. The descending band inside the graphical cut (left panel of the figure) corresponds to the protons stopping in the first layer of the Range Hodoscope, ascending band is due to the protons penetrating through the layer. The right panel shows an other correlation using three components of the Forward Detector: π, p, d and ${}^3\text{He}$ bands are visible. In both panels of the figure 3.19 the pions are minimum ionizing and only visible at low energy deposits.

Chapter 4

Analysis of the η Double Dalitz Decay

This chapter gives an overview of the analyzed data, describes the analysis steps for the tagging of the $\eta \rightarrow e^+e^-e^+e^-$ decay in data. The features of the tagging reaction are discussed. The analysis of the normalization channel $\eta \rightarrow e^+e^-\gamma$ is presented as a main background channel for the $\eta \rightarrow e^+e^-e^+e^-$ decay. Finally data and simulation are compared.

4.1 Tagging Reaction

In order to study a decay channel of the η meson, especially a rare decay, one should think about its production and define the reaction and the beam parameters for the experiment. In the combination WASA and COSY two main methods are used to produce η mesons:

- the reaction $pp \rightarrow pp\eta$ at a proton beam energy of $T = 1.4 \text{ GeV}$, where the η meson production cross section is $\sigma = 9.8 \pm 1.0 \mu\text{b}$ [56],
- the reaction $pd \rightarrow {}^3\text{He}\eta$ at a proton beam energy of $T = 1.0 \text{ GeV}$, where the η meson production cross section is $\sigma = 0.412 \pm 0.016 \mu\text{b}$ [57].

These methods have different advantages and complement each other in the studies of different η decay channels.

The reaction $pd \rightarrow {}^3\text{He}\eta$ has a lower cross section for η meson production than the reaction $pp \rightarrow pp\eta$, but there are several important arguments to use it instead of the proton-proton interactions:

- ${}^3\text{He}$ -ions can be easily identified in the Forward Detector and serve as a very selective trigger for η mesons in the reaction $pd \rightarrow {}^3\text{He}\eta$. A typical

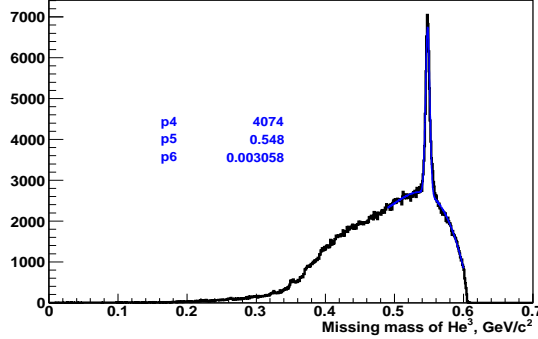


Figure 4.1: Unbiased distribution of the missing mass ${}^3\text{He}$ from experimental data. The blue curve represents a combined function of a Gaussian and a polynomial of third order. The values of the parameters of the Gaussian fit are shown: the parameter $p6$ corresponds to the missing mass resolution of $\sigma \sim 3 \text{ MeV}$. Events with exactly one ${}^3\text{He}$ track were selected satisfying the conditions on energy deposits in the first layer of Range Hodoscope, both layers of Window Counter and the first layer of Trigger Hodoscope.

distribution of the missing mass of ${}^3\text{He}$ after tagging the ${}^3\text{He}$ ions by the $\Delta E - E$ technique resulting in a clear peak at η mass with a width of $\sim 3 \text{ MeV}$ is shown in figure 4.1 for unpreselected data.

- significantly lower background: the cross section of two pion production in pd interactions is at least 20 times lower than in pp interactions. According to figure 4.1 the ratio of the η signal to background is $\sim 1:1$.
- tagging of the η mesons by the mentioned trigger does not put any conditions on the η decay system and, therefore, allows us to measure the absolute number of the η mesons and absolute branching ratios of the η decay channels.

Summarizing the advantages of the reaction $pd \rightarrow {}^3\text{He}\eta$, one can conclude that a clear signal of the η mesons in experimental data allows to focus on the analysis of the specific decay and control the signal of this η decay on different stages of analysis chain in the Central Detector. This can be done by monitoring the ${}^3\text{He}$ missing mass distribution for each introduced condition on the decay system. Thus, the reaction $pd \rightarrow {}^3\text{He}\eta$ is a very revealing tool especially for rare η decays. The developed methods for tagging of rare η decays in the central part of WASA can later be used in the analysis of the reaction $pp \rightarrow pp\eta$ with minor modifications.

Among the disadvantages is that the data on the cross sections of prompt pion production that are not available from this reaction at a beam energy $T = 1 \text{ GeV}$.

Beam energy	1 <i>GeV</i>
Beam momentum	1.7 <i>GeV/c</i>
Pellet rate	7 - 10 <i>kHz</i>
Cycle duration	100 <i>s</i>
Data recording within cycle	~90 <i>s</i>
Particles on flat top	5×10^9
Main trigger	<i>fwHeal fwHeb1 fHedwr1</i>
Magnetic field at (0,0,0) point	0.85 <i>T</i>
DAQ life time	90 %
Total number of analyzed runs	980
Sequences of analyzed runs	10392 - 11301, 11456 - 11525

Table 4.1: Experimental conditions and run characteristics during the beamtime in October, 2008

However, cross section measurements were done at similar energies for $pd \rightarrow {}^3\text{He}\pi^+\pi^-\pi^0$ and $pd \rightarrow {}^3\text{He}\pi^0\pi^0\pi^0$, see [60], for $pd \rightarrow {}^3\text{He}\pi^+\pi^-$ and $pd \rightarrow {}^3\text{He}\pi^0\pi^0$ in [61]. The method of subtracting the contributions from prompt pion production will be discussed in subsection 4.6.2.

4.2 Run Information

The data presented in this work were taken during a beamtime of four weeks in October, 2008, using the reaction $pd \rightarrow {}^3\text{He}\eta$, where a proton beam with a kinetic energy of $T_{beam} = 1 \text{ GeV}$ ($P_{beam} = 1.7 \text{ GeV}/c$) interacted with deuterium pellet target. The important characteristics of the beamtime are summarized in table 4.1.

The cycle starts with beam injection: protons are accelerated in cyclotron to the injection energy and then they are injected into the COSY ring, where they are accelerated to the energy of 1 *GeV*. During the cycle the beam is stored and interacts with the pellet target. The duration of the cycle is defined by beam losses due to beam-target interactions. In this beamtime it was set to 100 *s*. During such a period the beam current is dropping down typically by a factor of 2 and at the end of the cycle the remaining beam is dumped.

At beam injection and dumping the beam can interact with the beam pipe and other passive material close to WASA producing high counting rates, which are dangerous for the detectors. Due to that the voltages of the wire chambers are reduced during the beam injection and dumping. The high voltage modules receive the signal for ramping up after beam injection at $t_v = 3.4 \text{ s}$ and the detectors reach the operational values after a few seconds. Next, at $t_t = 7 \text{ s}$, the vacuum shutters open for the target system and the data acquisition system starts data recording.

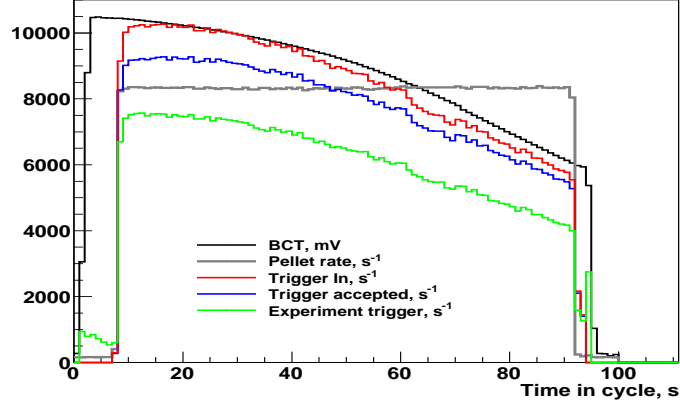


Figure 4.2: A typical beam cycle with rates: on the Y -axis the counting rate for different observables is shown, on the X -axis is the time in the cycle. The beam current (black curve) is provided by a beam current transformer (BCT) in arbitrary units and scaled up by factor of 3. The pellet rate is given per second (grey curve). The rates of triggers accepted by DAQ (Trigger accepted, in blue) and all input triggers (TriggerIN, in red) are scaled up by factor of ~ 10 here.

In the end of the cycle the voltages on the detectors are ramped down before the beam is dumped.

A typical beam cycle is shown in figure 4.2 with some important rates: the beam current, the pellet rate and three trigger rates. The moment of starting data taking can be tracked by the rising trigger rates.

4.3 Experiment Trigger

Identification of ^3He -ions on the trigger level is defined as trigger number 10 and used as main trigger. The trigger was organized in the following way to select events with at least one track satisfying the following criteria:

- the track must have a high energy deposit in both layers of the Window Counter, labeled as $fwHeal$ and $fwHeb1$ respectively,
- the track is found by the Track Matching procedure [58], labeled as $fhdwr1$, where "1" means at least one found track.

The Track Matching procedure is intended to increase the selectivity of the trigger by checking the elements of the Window Counter, Trigger Hodoscope and

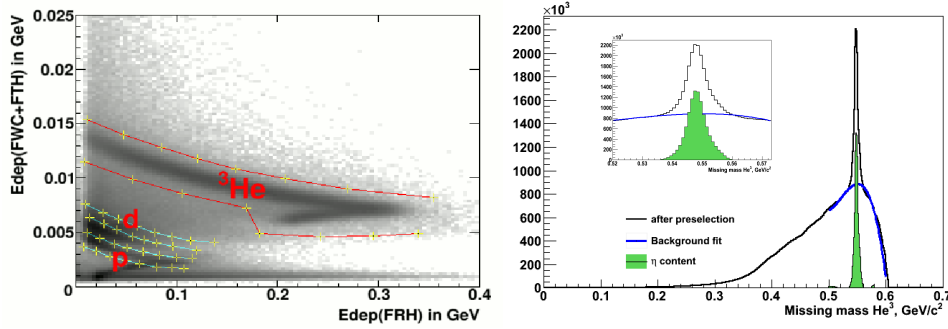


Figure 4.3: Signal of the η in data. Left panel: identification of ${}^3\text{He}$ ions in raw data by the ODIN analysis. ${}^3\text{He}$ band is clearly visible and is well separated from proton and deuteron bands. The red contour represents the graphical cut for selecting events with tracks inside the marked region. Right panel: missing mass of ${}^3\text{He}$ based on the preselected sample: the blue line represents the polynomial fit of the background and green filled area is the signal distribution after background subtraction.

Range Hodoscope for overlap in azimuthal angle (ϕ). These conditions only effect the Forward Detector and lead to an unbiased sample of the η mesons in the Central Detector.

4.4 Preselection and Calibration Sets

The data files provided by DAQ (raw data) were preselected by the ODIN analysis [59]. The preselection was based on the online calibration and aimed to select events with at least one track potentially associated with a ${}^3\text{He}$ track. The ${}^3\text{He}$ identification was based on the $\Delta E - E$ technique, which is shown in the left panel of the figure 4.3: the sum of energy deposits in both layers of the Window Counter and the first layer of the Trigger Hodoscope versus energy deposit in the first layer of the Range Hodoscope. The well enhanced ${}^3\text{He}$ band was selected by a graphical cut, shown as a red contour. Thus, the preselected sample contains all possible $pd \rightarrow {}^3\text{He}X$ events. These preselected data were analyzed in this work. A qualitative comparison between raw and preselected data is shown in figures 4.4 and 4.5, where the left side plots are based on raw data and the plots to the right are for data after the ${}^3\text{He}$ preselection. As it can be seen from the figure 4.4 the ${}^3\text{He}$ band becomes more pronounced after the preselection. The same effect is shown in the figure 4.5, the signature of the two body reaction, expressed in a "rising moon shape", becomes more enhanced.

The selected sample contains events from prompt pion production along with

Detector	calibration set valid for run periods
Mini Drift Chamber	10314 - 11525 (new generation)
Plastic Scintillator Barrel	10314 - 11525
Calorimeter	10314 - 16303
Window counter	3482 - 13776
Trigger Hodoscope	6795 - 11525
Range Hodoscope	10314 - 11301, 11455 - 11525
Proportional Chamber	10314 - now
Veto Hodoscope	10314 - now

Table 4.2: The calibration sets for the detector components used for the analysis.

the η -signal. The vector of the missing particle X can be reconstructed, since beam and target parameters are known and the ${}^3\text{He}$ track is reconstructed by the Forward Detector, therefore $\vec{X} = \vec{P} + \vec{D} - {}^3\vec{He}$. The mass of X (the missing mass of ${}^3\text{He}$) can be calculated by:

$$MM({}^3\text{He}) = \sqrt{(E_{beam} + m_d - E_{{}^3\text{He}})^2 - (p_{beam}^{\vec{}} - p_{{}^3\text{He}}^{\vec{}})^2} \quad (4.1)$$

The missing mass provided by equation 4.1 is shown in the right panel of figure 4.3 for the whole data sample after ${}^3\text{He}$ preselection. The η signal obtained after background subtraction counts roughly 10.7 million η -s (calculated with the Forward Detector).

The missing mass distribution with its pronounced peak at η -mass will be used for monitoring the η content in the experimental data and simulations at different stages of the analysis chain and finally will serve as a tool for calculating the $\eta \rightarrow e^+e^-e^+e^-$ admixture in the data sample.

The calibration sets used for the analysis are described in table 4.2. The components of the setup used for the analysis were calibrated for this run period or for previous beamtimes.

4.5 Signal and Background Simulation

4.5.1 Background Studies

Background studies have to take into account two parts: the cross section or branching ratio of the potential background channel and specific features of this channel (number and type of particles in the final state, the topology of the particles in space, the life time of the decay products etc.).

The cross section of the background channel corresponds to the probability in which degree it contributes to the final signal. The specific features of the back-

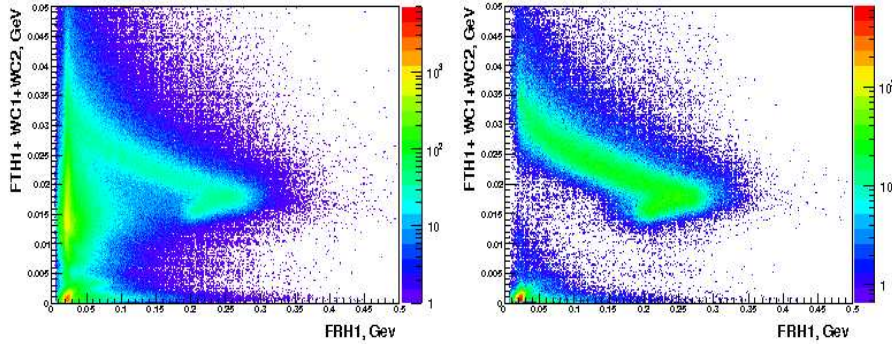


Figure 4.4: ${}^3\text{He}$ identification in data: raw data in the left panel and after ${}^3\text{He}$ preselection on the right panel. On the Y -axis is the sum of the energy deposits in both layers of Window counter and Trigger Hodoscope and on the X -axis is the energy deposited in the first layer of the Range Hodoscope. The same run (10876) was used.

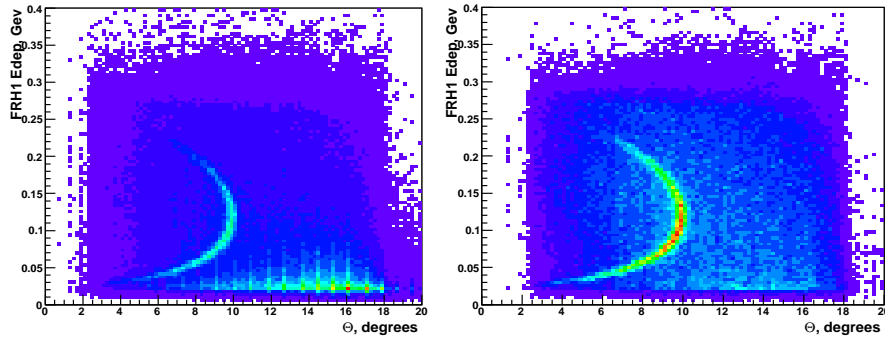


Figure 4.5: The signature of two body reaction $pd \rightarrow {}^3\text{He}X$: the scattering angle of the potential ${}^3\text{He}$ track on the X -axis and the energy deposited in the first layer of the Range Hodoscope on the Y -axis. The same run (10876) was used. Left panel represents the raw data, right panel is based on the preselected data after ${}^3\text{He}$ selection. The "rising moon" shape becomes more enhanced, indicating the $pd \rightarrow {}^3\text{He}\eta$ reaction.

ground channel reveal its behavior under cuts and define the acceptance for the background channel. The probability for background channel to contribute to the final sample of event candidates is defined first of all by the same final state as signal events. This includes particle misidentification, photon conversion and event overlap. Then, the distributions of observables for background channel can be completely different to the signal. For example, identical final states (four charged tracks) of the background channel and the signal channel can result in different regions (invariant mass of pions calculated with a mass of electron will be shifted), that can be used for background subtraction. Therefore, a high cross section of the background channel does not necessary mean a major contribution.

The analysis method (e.g. events selection, used cuts) is very revealing for the background consideration. The channels with muons were found to have a negligible contribution to the final state of the decay of interest. The channel $\eta \rightarrow \mu^+ \mu^- \gamma$ was studied, where the photon can convert into a $e^+ e^-$ pair. This contribution was found very low: only 24 events out of one million of simulated survived the final cuts. This can be explained by high penetration ability of muons without interacting with detector material.

There can be artificial background sources due to the properties of the setup and data taking. One of them is possible event overlap during data taking: by this effect the particles from random coincidences can be joined into the same event and thus fake the final state identical to the signal. It becomes unavoidable effect while comparing experimental data and Monte Carlo simulation: in the last case such phenomena do not exist at all. In order to study the effect of event overlap on the branching ratio the events with more or equal than four tracks were considered.

4.5.2 Simulation Channels

The current experimental upper limit for the branching ratio of the $\eta \rightarrow e^+ e^- e^+ e^-$ decay is 6.9×10^{-5} [19], the predicted branching ratio from Quantum Electrodynamics gives 2.6×10^{-5} [21]. The very low branching ratio of the signal channel implies that the possible background channels have to be studied carefully. In this work the channels with branching ratios larger than the experimental upper limit for the branching ratio of the decay $\eta \rightarrow e^+ e^- e^+ e^-$ were considered. The signal channel was simulated for the QED case as it was discussed in 3.1.1. Table 4.3 presents the simulated background channels.

The background for the decay $\eta \rightarrow e^+ e^- e^+ e^-$ can be divided into two sources. The first source is caused by η decays which can contribute to the same final state as $\eta \rightarrow e^+ e^- e^+ e^-$. Among them the channels with photons are significant since the probability of photon conversion in the 1.2 mm thick beryllium tube wall is 3×10^{-3} , which results in values comparable with the branching ratio. Table 4.4 contains the first estimate of the background admixture from the decays with pho-

Channel	BR	Number of events
$\eta \rightarrow e^+e^-e^+e^-$:	6.9×10^{-5} (u.l.)	100×10^3
$\eta \rightarrow \gamma\gamma$	3.93×10^{-1}	50×10^6
$\eta \rightarrow \pi^+\pi^-\pi^0$	2.27×10^{-1}	30×10^6
$\eta \rightarrow \pi^+\pi^-\gamma$	4.60×10^{-2}	7×10^6
$\eta \rightarrow \pi^0\pi^0\pi^0$	3.26×10^{-1}	50×10^6
$\eta \rightarrow \pi^+\pi^-e^+e^-$	2.68×10^{-1}	1×10^6
$\eta \rightarrow e^+e^-\gamma$	7.0×10^{-3}	1×10^6
$pd \rightarrow {}^3\text{He}\pi^+\pi^-\pi^0$	unknown	50×10^6
$pd \rightarrow {}^3\text{He}\pi^+\pi^-$	unknown	50×10^6
$pd \rightarrow {}^3\text{He}\pi^0\pi^0$	unknown	50×10^6
$pd \rightarrow {}^3\text{He}\pi^0\pi^0\pi^0$	unknown	50×10^6

Table 4.3: Simulated Monte Carlo channels for the $\eta \rightarrow e^+e^-e^+e^-$ and $\eta \rightarrow e^+e^-\gamma$ studies. The decay $\eta \rightarrow \pi^+\pi^-e^+e^-$ was considered only for studies of $\eta \rightarrow e^+e^-e^+e^-$. The last column contains the number of simulated events. The branching ratio for $\eta \rightarrow \pi^+\pi^-e^+e^-$ is taken from the Particle Data Booklet, 2010. The cross sections of the prompt pion production channels were taken as parameters for the first estimates, for calculating the branching ratio they were fitted and subtracted.

tons. As it can be seen, the single Dalitz decay is the most significant contributor despite that $\eta \rightarrow \gamma\gamma$ has a higher branching ratio.

Besides the background caused by η decays there are also background events due to prompt pion production. These channels are listed in the lower part of the table 4.3. The cross sections of these reactions are unknown for this beam energy, but they were measured at similar energies: $\sigma(pd \rightarrow {}^3\text{He}\pi^+\pi^-\pi^0) = 1.4\mu\text{b}$ and $\sigma(pd \rightarrow {}^3\text{He}\pi^0\pi^0\pi^0) = 0.18\mu\text{b}$ for a proton beam energy of $T_p = 1.36\text{GeV}$ [60], $\sigma(pd \rightarrow {}^3\text{He}\pi^0\pi^0) = 2.8\mu\text{b}$ and $\sigma(pd \rightarrow {}^3\text{He}\pi^+\pi^-) = 4.6\mu\text{b}$ at a beam energy of $T_p = 0.893\text{GeV}$ [61]. This source of background can be effectively subtracted by using the ${}^3\text{He}$ missing mass, where the prompt pion channels fill a continuous

Decay channel	BR_i	P_{4e}	$BR \times P_{4e}$	Admixture, %
$\eta \rightarrow e^+e^-e^+e^-$	6.9×10^{-5}	1	6.9×10^{-5}	100
$\eta \rightarrow \gamma\gamma$	3.9×10^{-1}	9×10^{-6}	3.5×10^{-6}	5.1
$\eta \rightarrow e^+e^-\gamma$	6.8×10^{-3}	3×10^{-3}	2.0×10^{-5}	29.0

Table 4.4: Preliminary estimates of background admixture for some η decay channels. The first column contains the decay channel, the second column the branching ratio BR_i , the third column is the probability P_{4e} to have two lepton pairs in final state, the fourth column is the total probability of the appearance of four leptons in the final state and the last column shows ratio the background channel and $\eta \rightarrow e^+e^-e^+e^-$.

region while the η decays result in a narrow peak sitting on top of the prompt pion events, see figure 4.3, for example.

4.6 Analysis Chain

4.6.1 Track Selection

The tagging of the η -decays in the reaction $pd \rightarrow {}^3\text{He}\eta$ starts with the track selection in the final state: there are a ${}^3\text{He}$ track and decay products to be detected. In this section the analysis of two η decays are discussed: in addition to the decay $\eta \rightarrow e^+e^-e^+e^-$, the study of the single Dalitz decay $\eta \rightarrow e^+e^-\gamma$ is presented.

${}^3\text{He}$ selection in the Forward Detector starts with checking the scattering angle of the tracks: it has to be inside the detector acceptance in the range 3° - 18° . Further cuts reproduce the trigger conditions, see 4.3. Potential ${}^3\text{He}$ candidates must have energy deposits in both layers of the Window Counter, the first layer of the Trigger Hodoscope and in the first layer of the Range Hodoscope. Using $\Delta E - E$ techniques allows to distinguish ${}^3\text{He}$ band from other particles, see figure 4.6. If there is exactly one track in the event with energy deposits above the red line then it is taken as a ${}^3\text{He}$ track. The procedure of ${}^3\text{He}$ identification is common for any η decay channel, see the advantages of the pd reaction in section 4.1.

The decay products are identified in the Central Detector. The momentum information from the Mini Drift Chamber is needed for the identification of the lepton pair and, therefore, the presence of this detector is the first condition for charged track reconstruction in the Central Detector. Thus, according to the current method of the track finder in the Central Detector, (see 3.3.1.4) the tracks with information from the following detector components are considered:

- MDC-PS
- MDC-SE
- MDC-PS-SE

In the next step the time of each charged track in the Central Detector is correlated with the time of a ${}^3\text{He}$ track. In figure 4.7 the time difference between each charged track in the Central Detector and a ${}^3\text{He}$ track is shown. The red lines represent the cut region. The last condition for track selection in the Central Detector is a preliminary vertex cut: the distance from the track to the vertex point was used. The distribution is shown in the figure 4.8, the gaussian fit gives $\sigma = 2.5$ mm . A generous cut in the interval $(-10;10)$ mm was applied that corresponds to a four σ -s interval. This cut is supposed to reject events not originating from the

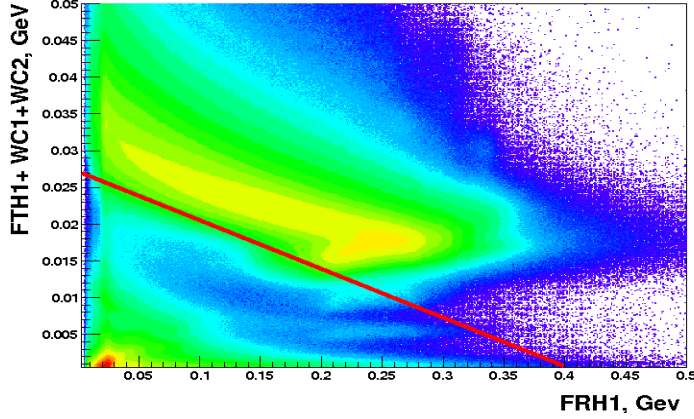


Figure 4.6: ${}^3\text{He}$ identification in data with the Forward Detector: X -axis -deposited energy in the first layer of Range Hodoscope, Y -axis - sum of the deposited energy in both layers of the Window Counter and the first layer of the Trigger Hodoscope. The tracks with energy deposits above the red line are associated with ${}^3\text{He}$ track.

vertex: secondary interactions, particularly events with photon conversion in the beam tube.

Neutral track selection is needed for $\eta \rightarrow e^+e^-\gamma$ studies. Their reconstruction is provided by the calorimeter. According to the current track finding algorithm a neutral track is defined as a solitary calorimeter cluster: MDC and PS information is used as veto. The selection of neutral tracks starts with a time condition similar to the charged track selection: the time of each neutral track is correlated with the time of ${}^3\text{He}$. The distribution is shown in figure 4.9. Another condition on the neutral track is the energy threshold for the suppression of *splitoff*-s. Energy of photons from single Dalitz of the η is shown in the figure 4.10. The cut was applied to consider photons with energies of $E \geq 0.1 \text{ GeV}$.

4.6.2 Normalization Channel $\eta \rightarrow e^+e^-\gamma$

A normalization channel is obligatory needed in order to calculate a branching ratio. In the formula for the branching ratio of the decay $\eta \rightarrow e^+e^-e^+e^-$ the total number of the η mesons produced in the experiment N_η is included. As it was pointed out earlier in section 4.1, the tagging of ${}^3\text{He}$ ions in Forward Detector does not introduce any bias on η decay system and the number of the η mesons derived from the missing mass of ${}^3\text{He}$ after ${}^3\text{He}$ identification does not include the reconstruction efficiency in the Central Detector. In order to consider the response of the Central Detector for the η decay products (e.g. efficiency of the lepton pair reconstruction) one should derive the number of the η mesons N_η from the another

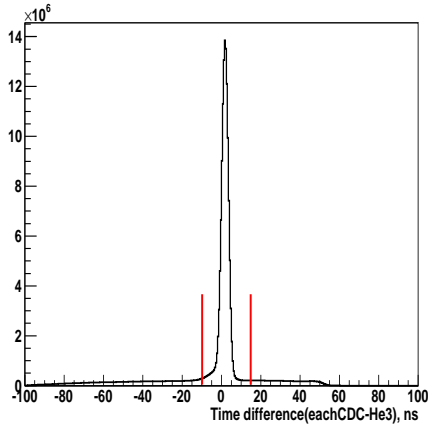


Figure 4.7: Experimental data: the time difference between each charged track in the Central Detector and ^3He track. The cut was applied in the range $[-10, 15]$ ns.

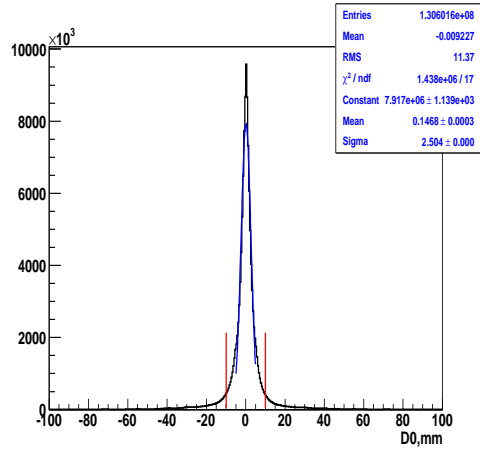


Figure 4.8: Experimental data: the distance from the MDC-cluster to the vertex in XY-plane after applying the time cut.

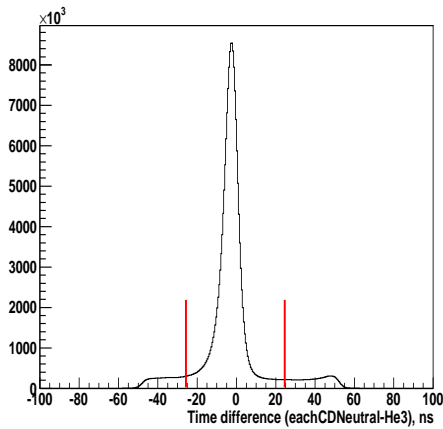


Figure 4.9: Experimental data: the time difference between each neutral track in the Central Detector and ^3He track. The red lines represent the cut region the range $[-25, 25]$ ns.

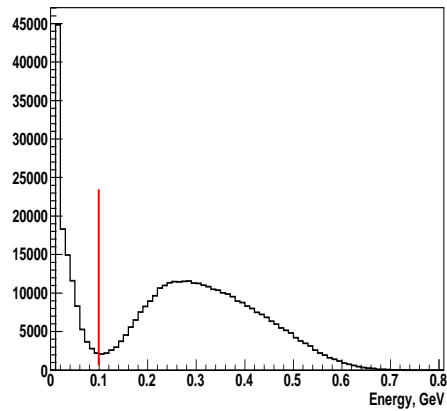


Figure 4.10: Monte Carlo simulation of the single Dalitz decay of the η : energy of the neutral tracks in laboratory frame, the events to the right from the red line were accepted for further analysis. The peak at low energies corresponds to the low energetic clusters in the calorimeter due to the splitoff-s.

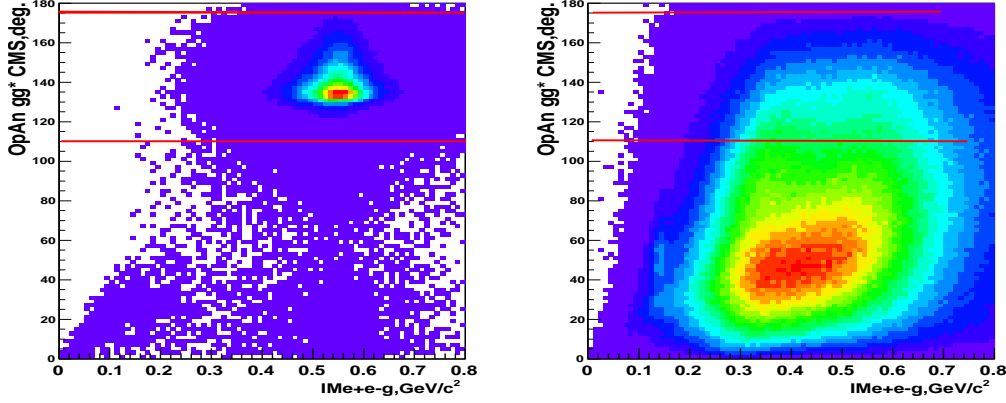


Figure 4.11: The opening angle between real and virtual photons in the center mass of the entire system on Y -axis and the invariant mass of $\eta \rightarrow e^+e^-\gamma$ on X -axis in GeV/c^2 . Left: the Monte Carlo simulation of the decay $\eta \rightarrow e^+e^-\gamma$, right: data under the same conditions. The events between red lines are accepted, that corresponds to the cut on the opening angle in the range ($110^\circ - 175^\circ$).

η decay. The single Dalitz decay was chosen as the normalization channel. This choice is caused by three reasons:

- it is the main background channel for $\eta \rightarrow e^+e^-e^+e^-$ and therefore the study of this channel is necessary for a better understanding of the signal channel
- the detector response for the lepton pair reconstruction can be checked with this decay: the reconstruction of lepton pairs, as well as photon conversion in the detector material
- the analysis methods for both decays $\eta \rightarrow e^+e^-e^+e^-$ and $\eta \rightarrow e^+e^-\gamma$ are similar, but the decay $\eta \rightarrow e^+e^-\gamma$ is statistically more abundant.

Event selection for the decay $\eta \rightarrow e^+e^-\gamma$

The event selection for the decay $\eta \rightarrow e^+e^-\gamma$ starts with the selection of exactly one positively and exactly one negatively charged track in the Central Detector. The total four-vector of these two tracks is assigned to the four-vector of the lepton pair or virtual photon γ^* . Afterwards, the neutral track selection procedure the opening angle Ω between γ and γ^* in the η rest frame has to be

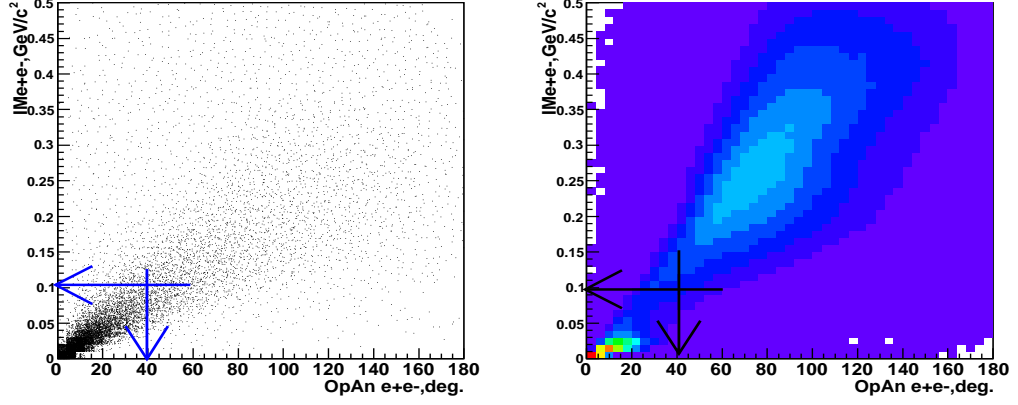


Figure 4.12: The correlation of the opening angle of the lepton pair on the X -axis and the invariant mass on the Y -axis. Left: Monte Carlo simulation, right: data. Both correlation plots are after track selection for the decay $\eta \rightarrow e^+e^-\gamma$. The arrows represent the cut region: events below with $IM_{e^+e^-} < 0.1 \text{ GeV}/c^2$, and with $\Omega_{e^+e^-} < 40^\circ$, are accepted for further analysis.

180° since $\eta \rightarrow \gamma\gamma^*$ is a two body process. In case of several neutral tracks the photon with Ω closest to 180° is selected. The next condition comes from the topology of the $\gamma - \gamma^*$ system in the center mass of the entire system: the opening angle between the real and virtual photons, see figure 4.11.

The next cut is based on the topology of the lepton pair, as it is enhanced at a low invariant mass, $IM_{e^+e^-}$, and a low opening angle of a lepton pair, $\Omega_{e^+e^-}$. This can be seen in the left panel of figure 4.12, where the correlation of the opening angle and invariant mass of lepton pair for the Monte Carlo simulation is shown. The blue lines represent the cut region. In the right panel the data under the same conditions as in the left panel are presented. Two enhancements are visible: the region close to the origin is due to the signal of $\eta \rightarrow e^+e^-\gamma$ and the decay $\eta \rightarrow \gamma\gamma$. The enhancement at higher angles and masses correspond to the channels with pions misidentified as electrons.

The cut on the invariant mass of the lepton pair suppresses the misidentified pions. The comparison of the Monte Carlo simulation and the data is shown in figure 4.13. In the right panel, for the data case, two enhancements are visible: the upper region towards the diagonal hints on massive particles - misidentified pions. Here the pions are coming from hadronic decays of the η ($\eta \rightarrow \pi^+\pi^-\pi^0$, $\eta \rightarrow \pi^+\pi^-\gamma$) and from prompt pion production, mainly from the $pd \rightarrow {}^3\text{He}\pi^+\pi^-\pi^0$. The low enhanced region is the signal of the decay $\eta \rightarrow e^+e^-\gamma$.

The influence of the cuts on the missing mass of ${}^3\text{He}$ is shown in figure 4.14. The black curve represents the distribution after all cuts and is compared to the

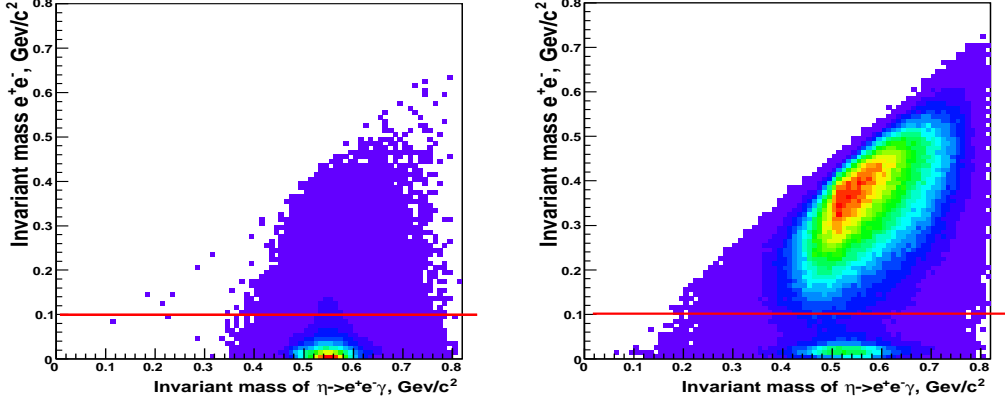


Figure 4.13: The correlation of the invariant masses of $\eta \rightarrow e^+e^-\gamma$ on the X -axis and of the lepton pair e^+e^- on the Y -axis. Left: Monte Carlo simulation, right: data. Both correlation plots are after event selection for the decay $\eta \rightarrow e^+e^-\gamma$ and after a preliminary cut on the missing mass of the decay products $e^+e^-\gamma$ in the range $(2.6-2.9) \text{ GeV}/c^2$. The events below the red horizontal line are accepted.

Monte Carlo simulation of the $\eta \rightarrow e^+e^-\gamma$ decay after the same cuts, drawn in red. From this comparison the significant content of the signal of the $\eta \rightarrow e^+e^-\gamma$ decay in data is visible. Concluding that, four orders of magnitude were suppressed in data by the designed cuts, all together the cuts lead to reasonable signal-to-background ratio, simulation and data can be compared at this stage of the analysis.

Comparison of Simulation and Data

All Monte Carlo channels were normalized to data according to the formula:

$$MC_i = \frac{1}{N_{sim_i}} * BR_i * N_\eta \quad (4.2)$$

where MC_i is the given Monte Carlo channel, N_{sim_i} is the number of simulated events, BR_i is the cross section or branching ratio for this channel and N_η is the total number of produced η -s in the experiment.

In figure 4.15 the comparison of simulation and data is shown. In the left panel the missing mass of ${}^3\text{He}$ after event selection and the cuts on the invariant mass of the lepton pair and on the missing mass of the decay products is shown. In the right panel the invariant mass of $e^+e^-\gamma$ after the mentioned cuts is plotted and, in an addition, the cut on the missing mass of ${}^3\text{He}$ is applied in order to

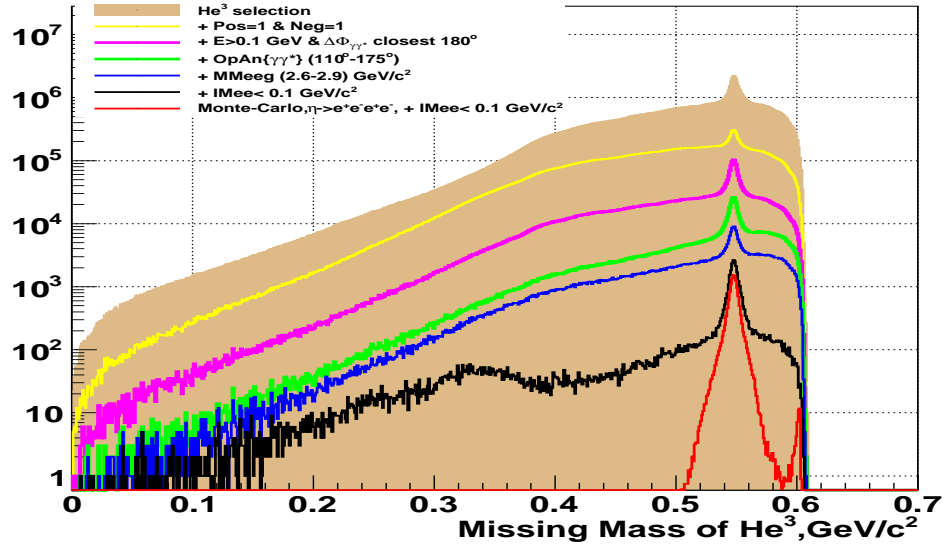


Figure 4.14: The missing mass of ${}^3\text{He}$ developing in data with the cuts for tagging the $\eta \rightarrow e^+e^-\gamma$ decay: the brown filled area corresponds to the events after the ${}^3\text{He}$ selection, the yellow curve is after selecting exactly one positively and one negatively charged track in the central detector, the pink curve is after photon selection, the green curve is after an additional cut on the opening angle between the real and the virtual photon in the center of mass of the entire system. The events survived after the cut on the missing mass of the decay products in the range (2.6 - 2.9) GeV/c^2 are shown by the blue line and after requiring the invariant mass of the lepton pair to be smaller than $0.1 \text{ GeV}/c^2$ are shown by the black curve. Each cut is an enhancement of the previous one. The red curve represents the Monte Carlo simulation of the $\eta \rightarrow e^+e^-\gamma$ decay under the same cuts as the black curve in data.

Channel	Cross section, μb
$pd \rightarrow He^3\pi^+\pi^-\pi^0$	0.5
$pd \rightarrow He^3\pi^+\pi^-$	6.8
$pd \rightarrow He^3\pi^0\pi^0$	1.8
$pd \rightarrow He^3\pi^0\pi^0\pi^0$	0.05

Table 4.5: Extracted cross sections of the prompt pion channels according to the missing mass of ${}^3\text{He}$ in the figure 4.15.

suppress non- η events. Here, the missing mass of ${}^3\text{He}$ was used to normalize the simulation to the data and for extraction of the parameters: the cross sections of the channels with prompt pions and the total number of the η -s N_η . The extracted values are shown in table 4.5. They are in reasonable agreement with the cross sections at slightly different beam energies. The total number of the η mesons was extracted as 9.6×10^6 . This number is lower than that one extracted with the Forward Detector in 4.4, it was 10.7×10^6 . The difference in total number of η -mesons is explained by involvement the Central Detector, that introduces some efficiency reconstruction for the decay products and, therefore, the total number of η -mesons has to be similar or lower than the extracted with the Forward Detector. As it can be seen the invariant masses in both Monte Carlo and data peak at η mass and have the same width. The shape in the peak region is slightly different, which can be explained by unknown differential distributions of the prompt pion channels.

In figure 4.16 the invariant mass of the lepton pair is shown. There are two regions: low masses correspond to the signal decay and double photon decay of the η and the region of higher masses is due to misidentified pions. The signal region is at the correct position, but high mass region differs in shape for Monte Carlo sum and data. It can be explained by a predominance of prompt pions and by hadronic η decays, which are not fully suppressed due to the absence of particle identification cuts. All presented distributions show a general agreement between Monte Carlo and data.

Prompt pions subtraction

The missing mass of ${}^3\text{He}$ can be effectively used for the separation of η decays from non- η events. Prompt pions result in a wide, smoothly populated region and can be easily fitted by a polynomial function and then subtracted. The missing mass of ${}^3\text{He}$ after the final cuts for the decay $\eta \rightarrow e^+e^-\gamma$ is shown in figure 4.15. There is a well pronounced peak from η decays sitting on a smooth background

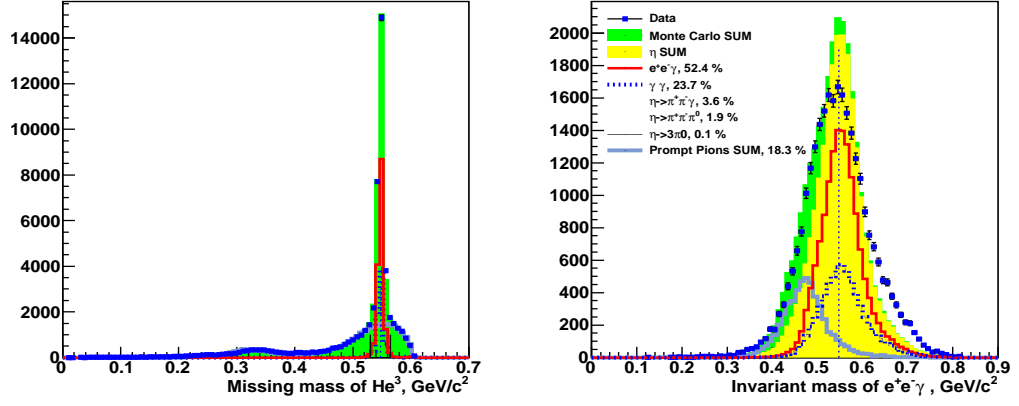


Figure 4.15: Left: ${}^3\text{He}$ missing mass after event selection for the decay $\eta \rightarrow e^+e^-\gamma$, with cut on the invariant mass of the lepton pair $IM_{e^+e^-} < 0.1\text{GeV}/c^2$ and a cut on the missing mass of the decay products $e^+e^-\gamma$ in the range $(2.6 - 2.9)\text{GeV}/c^2$. Right: the invariant mass distribution of the $e^+e^-\gamma$ is shown after the mentioned cuts and, in addition, a cut on the missing mass of ${}^3\text{He}$ in the range $(0.535 - 0.560)\text{GeV}/c^2$.

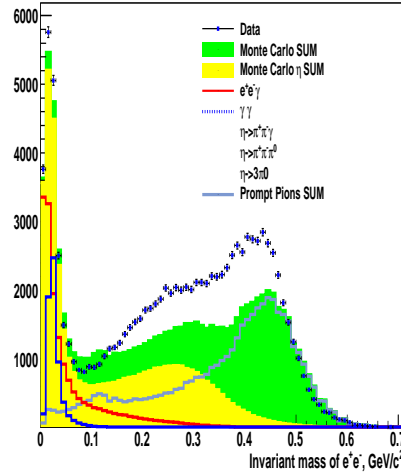


Figure 4.16: The invariant mass of lepton pair after the event selection for the decay $\eta \rightarrow e^+e^-\gamma$, the cut on the missing mass of the decay products in the range $(2.6 - 2.9)\text{GeV}/c^2$, the missing mass of ${}^3\text{He}$ in the range $(0.539 - 0.555)\text{GeV}/c^2$

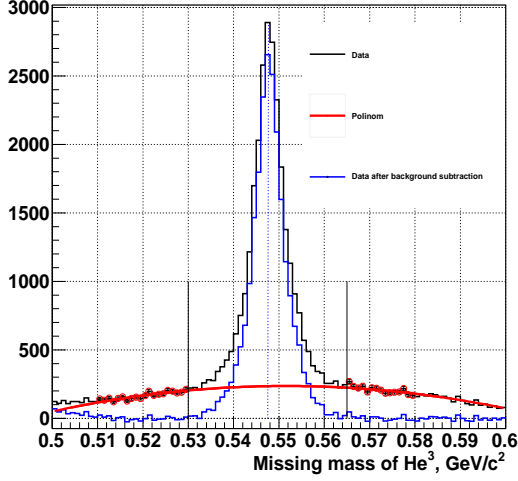


Figure 4.17: Subtraction of the prompt pions in data using the missing mass of ${}^3\text{He}$. The solid black line is the missing mass of $e^+e^-\gamma$ from the left panel of figure 4.15, the red curve represents a polynomial fit (second order) in the region outside the η signal and the solid blue line is the result after the subtraction of the polynomial background. The vertical black lines represent the η signal region, ($0.530 - 0.565 \text{ GeV}/c^2$). The points with error bars were considered for the background fit.

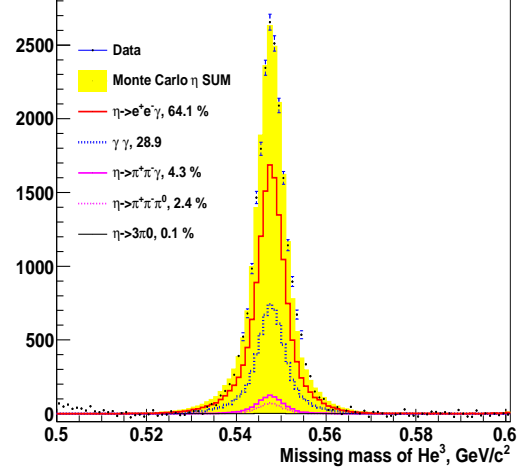


Figure 4.18: Normalization of the simulated η decays to the η content in data with the number of produced η -s N_η taken as a free parameter. The data points correspond to the missing mass of ${}^3\text{He}$ after prompt pions subtraction (blue curve in the figure 4.17). All η channels have identical shape and are normalized to the data according to the branching ratios.

caused by prompt pions. The enhancement between $0.3 - 0.4 \text{ GeV}/c^2$ is due to the prompt channel $pd \rightarrow {}^3\text{He}\pi^+\pi^-$, where the effect of the hadronic splittings was observed, for details see [41].

The result of the background fit on ${}^3\text{He}$ missing mass is shown in the figure 4.17. The fit range was chosen in the interval $0.5 - 0.6 \text{ GeV}/c^2$ and the points in the η signal region were excluded from the fit. The blue curve represents the ${}^3\text{He}$ missing mass after subtraction of the polynomial background. This is the content of the η decays in data. In figure 4.18 the normalization of the η decays in Monte Carlo to the η content in the data is shown. The total number of produced η -s N_η was taken as a fit parameter and the extracted value is 9.3×10^6 .

In addition, an alternative method was used to subtract prompt pions by fitting the missing mass of ${}^3\text{He}$ with an other function, defined as the sum of a polynomial and a Lorentzian function, see the figures 4.19 and 4.20. In the figure 4.19 the η

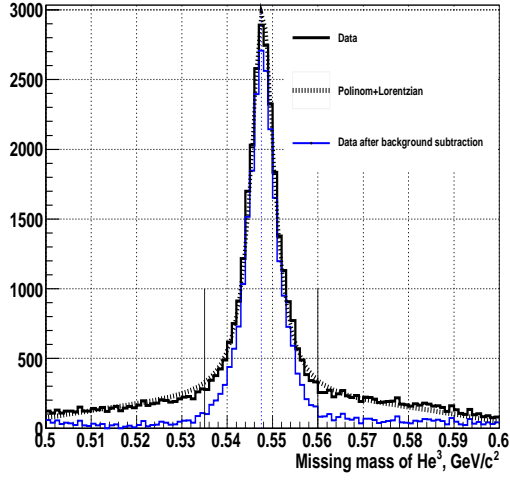


Figure 4.19: Subtraction of the prompt pions in data using the missing mass of ${}^3\text{He}$. The solid black line is the missing mass of $e^+e^-\gamma$ from the left panel of the figure 4.15, the thick dotted curve represents a function which is the sum of a second order polynomial and a Lorentzian function, the solid blue line is the result after the subtraction of the polynomial background. The vertical black lines represent the η signal region, $(0.530 - 0.565\text{GeV}/c^2)$. The points with error bars were considered for background fit.

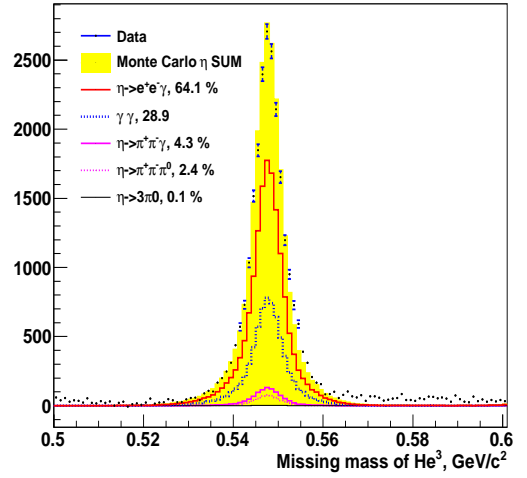


Figure 4.20: Normalization of the simulated η decays to the η content in data with the number of produced η -s N_η taken as a free parameter. The data points correspond to the missing mass of ${}^3\text{He}$ after prompt pions subtraction (blue curve in the figure 4.19). All η channels have identical shape and are normalized to the data according to the branching ratios.

signal region is described by a Lorentzian and the background is described by a polynomial of second order, the total function reproduces the missing mass of ${}^3\text{He}$ spectrum before prompt pion subtraction. Here, the extracted number of N_η is 9.8×10^6 . The average among two measurements for N_η equals to 9.6×10^6 .

The number of single Dalitz - decay event candidates in the first case is 14200 ± 170 , in the second case 15200 ± 170 events, where 170 corresponds to the statistical error. It was defined as $\sqrt{N_{\eta Peak}}$, where $N_{\eta Peak}$ is given by the integral of the missing mass distribution before prompt pions subtraction in the range of the η signal ($0.535 - 0.560$) GeV/c^2 .

The derived number of the η mesons N_η has a systematic error due to prompt pions, this error can be taken as the difference between two presented measurements as 0.5×10^6 , which corresponds to 5 % systematic error by prompt pions.

4.6.3 Event Selection for the Decay $\eta \rightarrow e^+e^-e^+e^-$

Lepton Pair Identification

After the tracks were selected in the Central Detector, the next cuts for the decay $\eta \rightarrow e^+e^-e^+e^-$ are based on the final state of the decay: two electron-positron pairs which have to be identified. From the measurement of the single Dalitz decay of the η and the double Dalitz decay of π^0 [22] it is known that the invariant mass of lepton pairs coming from the virtual photon γ^* will be small.

The cut on the events with more at least two positively and two negatively charged tracks leads to an array of tracks in which the two correct lepton pairs have to be found. First, a lepton pair is identified as a pair of the tracks with opposite charge. In this case the number of possible two pair combinations which appear once each track is given by the formula:

$$N = \frac{1}{2} \times kp \times kn \times (kp - 1) \times (kn - 1) \quad (4.3)$$

where kp and kn is the number of positively and negatively charged tracks, respectively.

Let us consider an event of class **A** with $kp = 2$ and $kn = 2$ and mark the vectors of the first positively charged track as \vec{p}_1 and the second as \vec{p}_2 , two negatively charged tracks as \vec{e}_1 and \vec{e}_2 . The typical event is depicted in the figure 4.21. In this case the formula 4.3 gives $N = 2$, that means there are two possibilities to form the final state of the decay with two lepton pairs:

- case 1: $\vec{L}_1 = \vec{p}_1 + \vec{e}_1$ and $\vec{L}_2 = \vec{p}_2 + \vec{e}_2$
- case 2: $\vec{L}'_1 = \vec{p}_2 + \vec{e}_1$ and $\vec{L}'_2 = \vec{p}_1 + \vec{e}_2$

where \vec{L}_i denotes the vector of lepton pair.

The lepton pairs in both cases are different while the η candidate is only one. The electron and positron from the same virtual photon must form the lepton pair with the smallest invariant mass. This was used to identify the lepton pairs in this study. Thus, the sum of invariant masses of both lepton pairs has to be minimized: $Min(L_1 + L_2, L'_1 + L'_2)$, where L_1, L_2, L'_2 and L'_1 are the invariant masses of lepton pairs.

In another class of the events **B** the number of positively or negatively charged tracks is more than two: $kp > 2$ and $kn \geq 2$, $kp \geq 2$ and $kn > 2$. For example the event has $kp = 3$ and $kn = 2$, where one of the positively charged tracks is due to event overlap (as discussed in 4.5.1), and coming from an other event. In this event four tracks have to be identified as coming from the double Dalitz of the η and the fifth track has to be ignored and not considered for further calculations. Let us mark the tracks as $\vec{p}_1, \vec{p}_2, \vec{p}_3$ (positively charged tracks) and \vec{e}_1, \vec{e}_2 (negatively charged tracks). In this case the formula 4.3 gives $N = 6$, i.e. six possibilities to form the final state of double Dalitz decay:

- case 1: $\vec{L}_1 = \vec{p}_1 + \vec{e}_1$ and $\vec{L}_2 = \vec{p}_2 + \vec{e}_2$
- case 2: $\vec{L}'_1 = \vec{p}_1 + \vec{e}_1$ and $\vec{L}'_2 = \vec{p}_3 + \vec{e}_2$
- case 3: $\vec{L}_1^{\clubsuit} = \vec{p}_1 + \vec{e}_2$ and $\vec{L}_2^{\clubsuit} = \vec{p}_2 + \vec{e}_1$
- case 4: $\vec{L}_1^{\diamond} = \vec{p}_1 + \vec{e}_2$ and $\vec{L}_2^{\diamond} = \vec{p}_3 + \vec{e}_1$
- case 5: $\vec{L}_1^{\heartsuit} = \vec{p}_2 + \vec{e}_1$ and $\vec{L}_2^{\heartsuit} = \vec{p}_3 + \vec{e}_2$
- case 6: $\vec{L}_1^{\spadesuit} = \vec{p}_2 + \vec{e}_2$ and $\vec{L}_2^{\spadesuit} = \vec{p}_3 + \vec{e}_1$

Here, the same method for identifying the correct two pairs was used: those two pairs which give the lowest sum of their invariant masses were selected: $Min(L_1 + L_2, L'_1 + L'_2, \vec{L}_1^{\clubsuit} + \vec{L}_2^{\clubsuit}, \vec{L}_1^{\diamond} + \vec{L}_2^{\diamond}, \vec{L}_1^{\heartsuit} + \vec{L}_2^{\heartsuit}, \vec{L}_1^{\spadesuit} + \vec{L}_2^{\spadesuit})$.

Topological Cuts

After the selection of the two lepton pairs one can apply further cuts based on their topology: there are several topological features in this decay. In the left panel of the figure 4.22 the correlation of the invariant mass and the opening angle of each lepton pair is plotted. As it can be seen most of events have small opening angles Ω_{ee} and low invariant masses IM_{ee} . Events with the opening angle $\Omega_{ee} < 40^\circ$ and invariant mass $IM_{ee} < 0.1 \text{ GeV}/c^2$ were accepted. In the right panel of figure 4.22 the opening angle Φ_{L_1, L_2} between the selected lepton pairs is shown (see the

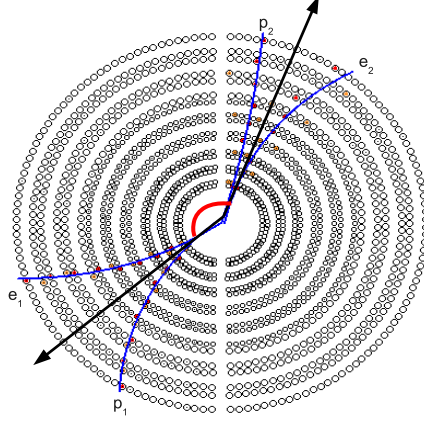


Figure 4.21: Typical event candidate of the decay $\eta \rightarrow e^+e^-e^+e^-$ from Monte Carlo simulation (XY -plane). The lepton tracks are the blue curves, p_1, e_1 are the positron and electron from the first lepton pair, p_2, e_2 are the positron and electron from the second lepton pair, the vectors of lepton pairs are marked as black arrows, the angle between the lepton pairs is marked in red. The topology of the lepton pairs shows the small opening angle between positron \vec{p}_1 (\vec{p}_2) and electron \vec{e}_1 (\vec{e}_2) from the same virtual photon.

angle marked red in the figure 4.21). The events between two blue verticals in the right panel of figure 4.22 were accepted: $\Phi_{L1,L2} = (85^\circ - 175^\circ)$. Thus, the set of cuts:

- $\Omega_{ee} < 40^\circ$
- $IM_{ee} < 0.1 \text{ GeV}/c^2$
- $\Phi_{L1,L2} = (85^\circ - 175^\circ)$

will be called topological cuts.

The development of the missing mass of ${}^3\text{He}$ in data under the discussed cuts is shown in figure 4.23. Several orders of magnitude are suppressed after the cuts. The selection of events with at least two positively and two negatively charged tracks suppresses three orders of magnitude. This can be explained by only a few final states with four charged tracks. The cut on the invariant mass and the opening angle of the lepton pairs rejects a significant share of the events with pions.

The reconstruction efficiency of the decay $\eta \rightarrow e^+e^-e^+e^-$ according to Monte Carlo study is around 12% after the topological cuts. It implies that less than

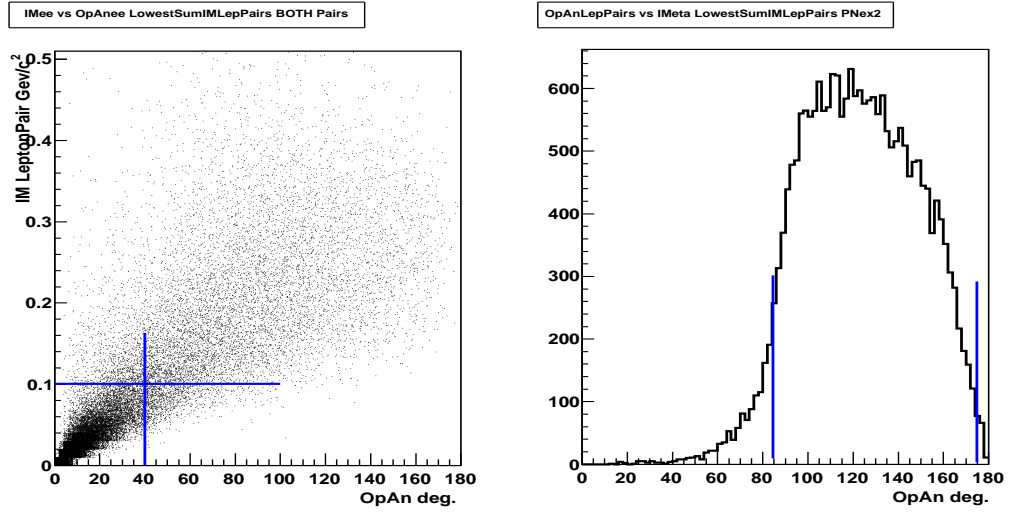


Figure 4.22: Monte Carlo for $\eta \rightarrow e^+e^-e^+e^-$. Left: invariant mass of the e^+e^- pair versus the opening angle between e^+ and e^- , right: the opening angle between lepton pairs in the laboratory frame. The blue lines represent the cut region: in the left events under the horizontal line and to the left of the vertical line are accepted, in the right: the events between the two lines are accepted.

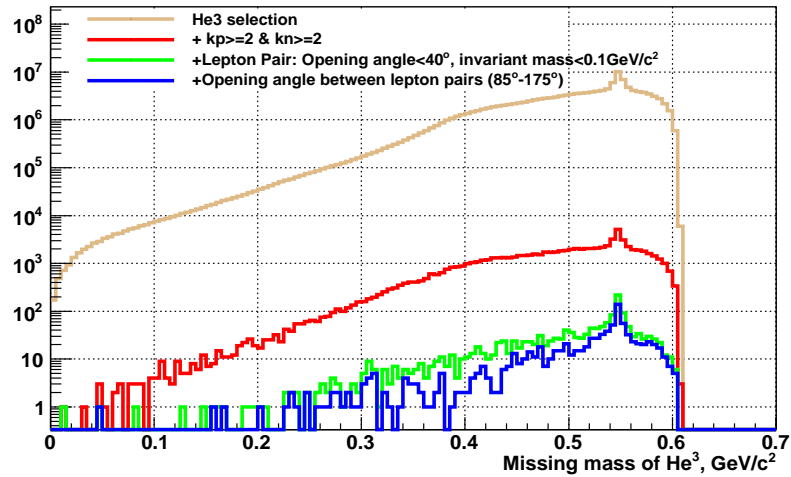


Figure 4.23: Missing mass of ${}^3\text{He}$ developing under the different cuts in data: each cut is an enhancement of the previous one. The events after ${}^3\text{He}$ selection are drawn in brown, the red curve represents the events after selecting at least two positively and two negatively charged tracks in the central detector, the green curve is after applying the cuts on the invariant mass and the opening angle of lepton pair: $\Omega_{ee} < 40^\circ$ and $IM_{ee} < 0.1 \text{ GeV}/c^2$, blue shows the distribution after the topological cuts.

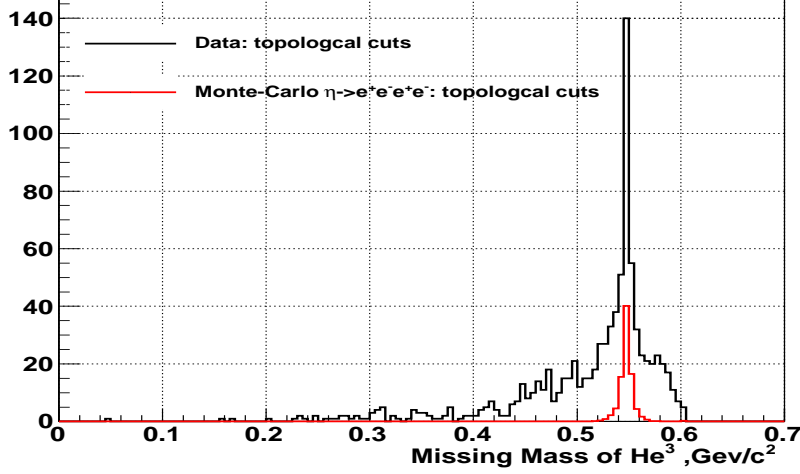


Figure 4.24: Missing mass of ${}^3\text{He}$ after the topological cuts. Black curve is the data, that corresponds to the blue curve in the figure 4.23, red is the simulation of the decay $\eta \rightarrow e^+e^-e^+e^-$ after the same cuts. It was normalized to the data with the branching ratio $BR = 6.9 \times 10^{-5}$ and the total number of the η -s $N_\eta = 9.6 \times 10^6$.

60 events of the decay $\eta \rightarrow e^+e^-e^+e^-$ are expected in the whole data sample, assuming a branching ratio of 6.9×10^{-5} .

In the figure 4.24 a comparison of the Monte Carlo simulation of the signal channel and data is shown after the topological cuts. The remaining background from the η decays is mostly coming from the hadronic decays of the η , mainly from the $\eta \rightarrow \pi^+\pi^-\pi^0$ decay.

The next cut is related to electron-pion separation on the event selection level. In figure 4.25 the missing mass of the decay products $e^+e^-e^+e^-$ after the topological cuts is shown. The signal channel with the main background channel $\eta \rightarrow \pi^+\pi^-\pi^0$ and sum of the prompt pion channels are shown for illustration. There are two enhancements in the figure: the lower is around the mass of $2.8 \text{ GeV}/c^2$, which corresponds to the mass of ${}^3\text{He}$, and at higher masses, which is due to misidentified pions. Using the vertical dotted lines as cut region the channels with pions can be effectively rejected. The effect of this cut on the missing mass of ${}^3\text{He}$ is demonstrated in figure 4.26. The background from η decays is suppressed by factor of 3, which is due to the rejection of events from $\eta \rightarrow \pi^+\pi^-\pi^0$. The cut finally leads to a signal to background ratio $\sim 1 : 1$.

The reconstruction efficiency for $\eta \rightarrow e^+e^-e^+e^-$ under the discussed cuts is shown in table 4.6.

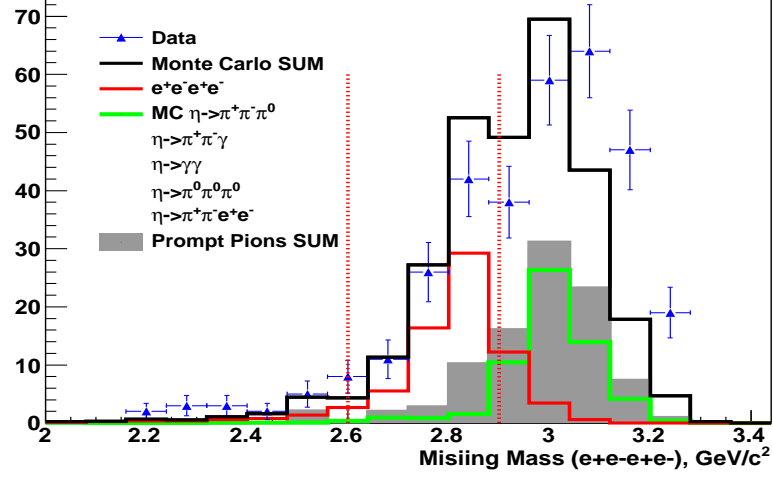


Figure 4.25: Missing mass of the decay products $e^+e^-e^+e^-$ after the topological cuts and the cut on the missing mass of ${}^3\text{He}$ in the range $(0.535 - 0.560) \text{ GeV}/c^2$. The cross sections for prompt channels were taken from the missing mass of ${}^3\text{He}$ in the figure 4.27.

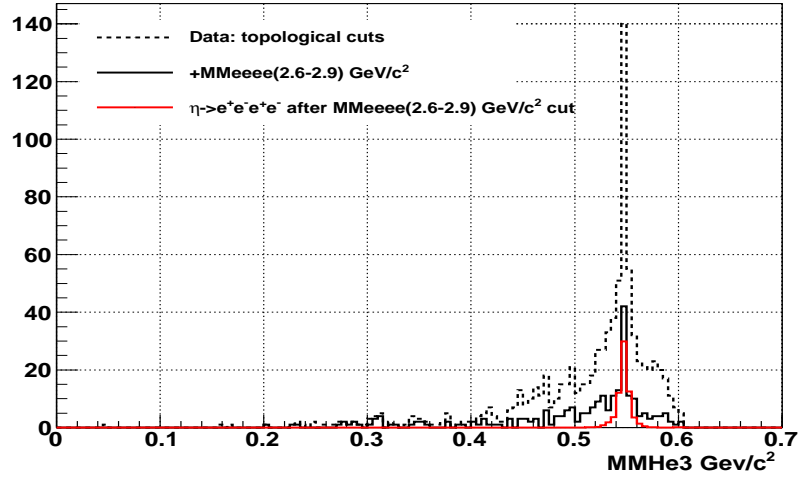


Figure 4.26: Missing mass of ${}^3\text{He}$. The black dotted curve is data after the topological cuts: the cut on the invariant mass and the opening angle of both lepton pairs: $IM_{ee} < 0.1 \text{ GeV}/c^2$, $\Omega_{ee} < 40^\circ$ and the cut on the opening angle between the lepton pairs and solid black is in addition after the cut on the missing mass of the decay products in the range $2.6 - 2.9 \text{ GeV}/c^2$. The red is the simulation of the decay $\eta \rightarrow e^+e^-e^+e^-$ after the topological cuts and the cut on the missing mass of the decay products. The simulation was normalized to the data with the branching ratio $BR = 6.9 \times 10^{-5}$ and the total number of the η -s $N_\eta = 9.6 \times 10^6$.

Cut	Efficiency, %
cut1	90,8
cut2	20,9
cut3	12,6
cut4	10,0

Table 4.6: Efficiencies of the cuts: each cut is an enhancement of the previous one. Cut1 yields events after ${}^3\text{He}$ reconstruction in the forward detector, cut2 selects events with at least two positively and negatively charged tracks in the central detector, cut3 is based on the topology of two lepton pairs and includes three conditions: the opening angle of lepton pair is smaller than 40° , the invariant mass of lepton pair is smaller than $0.1\text{GeV}/c^2$ and the opening angle between two lepton pairs has to be in the range $(85^\circ - 175^\circ)$, cut4 yields events with the missing mass of the decay products in the range $(2.6 - 2.9)\text{GeV}/c^2$.

4.7 Simulation and Data Comparison

The number of simulated events for each Monte Carlo channel is different due to the different reconstruction efficiency, see table 4.3. Data and Monte Carlo simulation are compared under the same set of cuts. Each Monte Carlo channel is normalized to the data according to formula 4.2, with the total number of the η -s $N_\eta = 9.6 \times 10^6$. In this section for illustrative purpose, the branching ratio for $\eta \rightarrow e^+e^-e^+e^-$ was taken as 6.9×10^{-5} and cross sections of the prompt pion channels are taken as parameters. ${}^3\text{He}$ missing mass distribution was used for the extraction of the parameters which later are used for other distributions. Thus, the presented figures contain information about the cross sections of prompt pions and are not related to the branching ratio calculation.

In figure 4.27 the ${}^3\text{He}$ missing mass after the topological cuts is shown for data and Monte Carlo. The values of the prompt pion cross sections are were extracted and used for the invariant mass of $e^+e^-e^+e^-$, see table 4.7.

In the ${}^3\text{He}$ missing mass distribution the prompt pions are seen as a wide, smoothly populated region (grey filled area), that will be later used for their subtraction, analogically to the $\eta \rightarrow e^+e^-\gamma$ studies. On the invariant mass distribution of $e^+e^-e^+e^-$ the prompt pion background results in a peak shifted to the left from η mass due to misidentified pions. In order to suppress the channels with pions the distribution of the missing mass of the decay products is used, shown in figure 4.25. The missing mass of ${}^3\text{He}$ and the invariant mass of $e^+e^-e^+e^-$ after applying the cut for $MM_{e^+e^-e^+e^-}$ in the range $(2.6 - 2.9)\text{GeV}/c^2$ are shown in figure 4.28. As it can be seen from the invariant mass of $e^+e^-e^+e^-$ the prompt pions are suppressed by 35 %, the $\eta \rightarrow \pi^+\pi^-\pi^0$ is suppressed nearly by 80 % and the signal to background ratio is improved by factor of two.

Channel	Cross Section, μb , Fig. 4.27	Cross Section, μb , Fig. 4.28
$pd \rightarrow He^3\pi^+\pi^-\pi^0$	0.2	0.7
$pd \rightarrow He^3\pi^+\pi^-$	3.5	2.4
$pd \rightarrow He^3\pi^0\pi^0$	3.8	2.1
$pd \rightarrow He^3\pi^0\pi^0\pi^0$	0.03	0.03

Table 4.7: Extracted cross sections of the prompt pion channels according to the missing mass of ${}^3\text{He}$ in figures 4.27 and 4.28.

The extracted cross sections are in a reasonable agreement with expectations and previously extracted values for the single Dalitz decay of the η , see table 4.5.

The agreement between data and simulations is demonstrated for different cut combinations in figures 4.27 and 4.28. The missing mass of ${}^3\text{He}$ distribution after the topological cuts shows a slight discrepancy in the η mass region and good agreement for the prompt pion background. The discrepancy can be explained by a high admixture of prompt pions. On the invariant mass distribution in figure 4.27 the η signal region in data is reproduced by Monte Carlo, while lower mass region is not. This is due to the cut on the missing mass of ${}^3\text{He}$ in the η signal region for the invariant mass distribution. Rather good agreement between data and simulation is seen in figure 4.28 after applying the cut on the missing mass of the decay products. The missing mass of ${}^3\text{He}$ is perfectly described in the peak region, but certain discrepancy appears in adjoining region. Good agreement between data and simulation is seen for the invariant mass distribution.

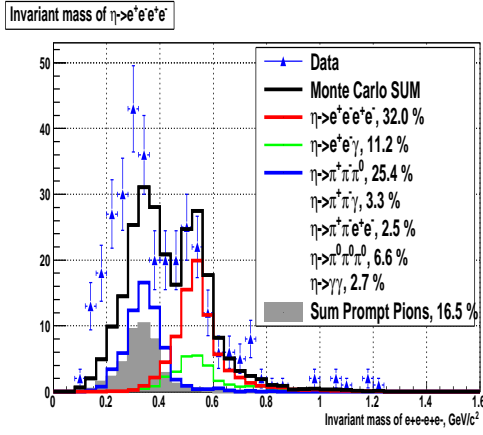
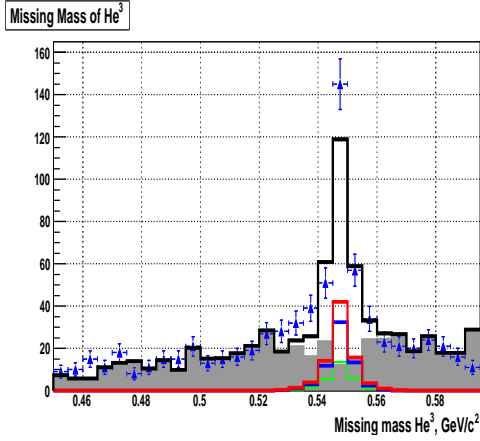


Figure 4.27: Upper panel: ${}^3\text{He}$ missing mass after the topological cuts, lower panel: the invariant mass of $e^+e^-e^+e^-$ after the same cuts and the cut on the missing mass of ${}^3\text{He}$ in the range $(0.535 - 0.560)\text{GeV}/c^2$.

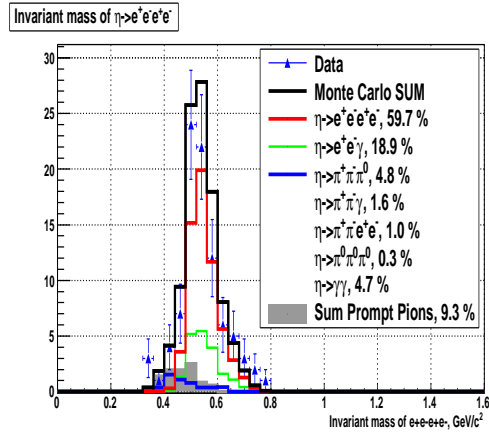
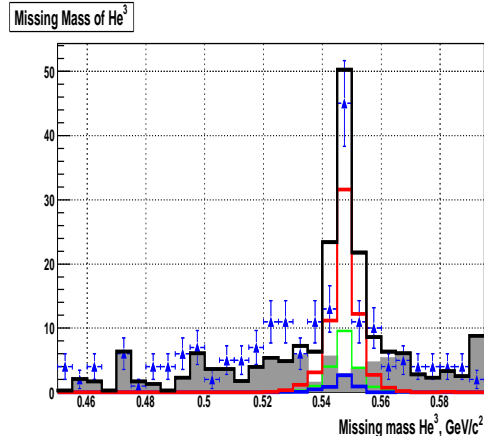


Figure 4.28: Upper panel: ${}^3\text{He}$ missing mass after the topological cuts and the cut on the missing mass of the decay products in the range $(2.6 - 2.9)\text{GeV}/c^2$, lower panel: the invariant mass of $e^+e^-e^+e^-$ after the same cuts and the cut on the missing mass of ${}^3\text{He}$ in the range $(0.535 - 0.560)\text{GeV}/c^2$.

Chapter 5

Results

5.1 Method

The calculation of the branching ratio for the decay $\eta \rightarrow e^+e^-e^+e^-$ is based on the ${}^3\text{He}$ missing mass, because on this distribution the signal from η decays can be separated from the background channels with prompt pions. This step is necessary since the cross sections of prompt pions are not exactly known. Their values extracted as the fit parameters are not reliable since the entire analysis is designed in the way to suppress them.

The ${}^3\text{He}$ missing mass is considered under the topological cuts and the cut on the missing mass of the decay products. Under this set of cuts agreement between data and simulations has been demonstrated in section 4.7. In this chapter the branching ratio is taken as a parameter in the normalization procedure of the η sum in Monte Carlo and η content in data. The ${}^3\text{He}$ missing mass from the different η decays are identical. Each channel was normalized to data according to formula 4.2. The total number of η -s N_η is taken from the study of the normalization process as $N_\eta = (9.6 \pm 0.5) \times 10^6$, extracted in 4.6.2.

The $BR(\eta \rightarrow e^+e^-e^+e^-)$ is given by formula:

$$BR(\eta \rightarrow e^+e^-e^+e^-) = \frac{N_{\eta \rightarrow e^+e^-e^+e^-}}{N_\eta * \varepsilon} \quad (5.1)$$

where $N_\eta = 9.6 \times 10^6$ corresponds to the total number of η -s produced in the experiment, ε is the reconstruction efficiency for the $\eta \rightarrow e^+e^-e^+e^-$ decay given by $\varepsilon = \frac{N_{rec}}{N_{sim}}$, N_{rec} is a number of reconstructed events and N_{sim} is a number of generated events. The number of event candidates for $\eta \rightarrow e^+e^-e^+e^-$ is given by:

$$N_{\eta \rightarrow e^+e^-e^+e^-} = N_{\eta Data} - N_{\eta Background} \quad (5.2)$$

where $N_{\eta Data}$ is the integral of the ${}^3\text{He}$ missing mass in data after prompt pion

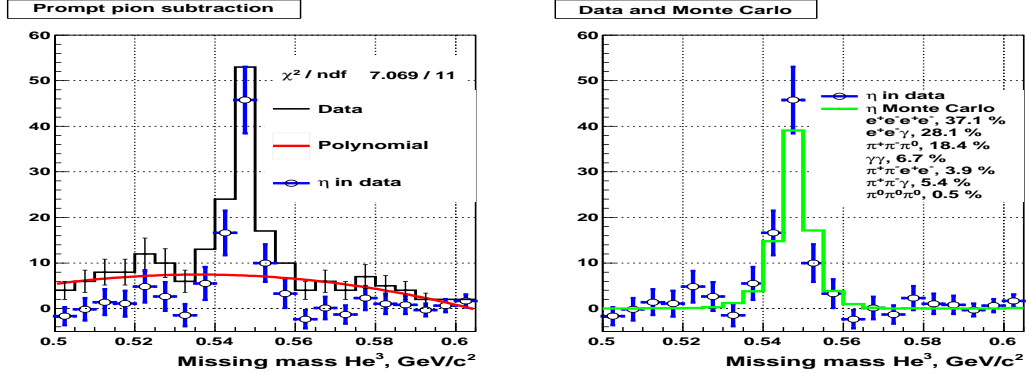


Figure 5.1: Left panel: missing mass ${}^3\text{He}$ after the topological cuts and the cut on the missing mass of decay products in the range $(2.64 - 2.96 \text{ GeV}/c^2)$, drawn in black, is fitted by a polynomial of second order, drawn in red. The blue points with error bars is the missing mass of ${}^3\text{He}$ after the subtraction of the polynomial background, the error bars correspond to the statistical errors before polynomial subtraction. The black error bars show the points considered for the fit, as can be seen the η signal region was excluded. Right panel: comparison of η content in data with Monte Carlo sum of η channels, the branching ratio for the $\eta \rightarrow e^+e^-e^+e^-$ is taken as a parameter.

Figure	$(BR \pm Er_{stat}) \times 10^{-5}$	$N_{cand} \pm Er_{stat}$	$N_{\eta Data} \pm Er_{stat}$
Fig.5.1, middle	2.9 ± 1.1	29.7 ± 10.8	82.0 ± 10.8

Table 5.1: Example for the branching ratio calculations. The missing mass of ${}^3\text{He}$ after the topological cuts and the cut on the missing mass of the decay products in the range $(2.64 - 2.96 \text{ GeV}/c^2)$ was used. The prompt pion background was fitted by the second order polynomial. $N_{cand} = N_{\eta \rightarrow e^+e^-e^+e^-}$ is a number of $\eta \rightarrow e^+e^-e^+e^-$ event candidates.

subtraction in the range $0.535 - 0.560 \text{ GeV}/c^2$, $N_{\eta Background}$ is the integral of the ${}^3\text{He}$ missing mass distribution in Monte Carlo without the $\eta \rightarrow e^+e^-e^+e^-$ decay and can be found by:

$$N_{\eta Background} = N_{\eta Data} - N_{\eta \rightarrow e^+e^-e^+e^-} \quad (5.3)$$

Thus, the task for the branching ratio determination is the measurement of the number of η -mesons in the final event sample $N_{\eta Data}$.

An example of the fitting the prompt pion background is presented in the left panel of the figure 5.1. The missing mass of ${}^3\text{He}$ is taken under the topological cuts (black curve) and the cut on the missing mass of the decay products in the range $(2.64 - 2.96 \text{ GeV}/c^2)$. The polynomial of the second order is used for background fit in the range $(0.5 - 0.6) \text{ GeV}/c^2$, the η signal region was excluded from the fit. The blue points with error bars represent the remaining η content in data. In the

right panel of the figure 5.1 the Monte-Carlo cocktail from η decays is normalized to the η content in data.

The extracted branching ratio with the statistical error is presented in the table 5.1. In this table and other tables of the chapter $N_{cand} = N_{\eta \rightarrow e^+e^-e^+e^-}$ is a number of event candidates of double Dalitz decay of η . The statistical error Er_{stat} for the branching ratio, number of event candidates and number of η -mesons is defined by the number of events on ${}^3\text{He}$ missing mass **before** the prompt pion subtraction in the η signal region: $(0.535 - 0.560) \text{ GeV}/c^2$. Thus, the table contains all necessary information: in the first column the pointer to the certain figure is listed, in the second column the branching ratio with its statistical error is presented, in the third column number of event candidates for the $\eta \rightarrow e^+e^-e^+e^-$ decay with statistical error, the last column contains the number of the η -mesons in data after prompt pion subtraction.

According to the table the number of events due to the prompt pions production can be obtained as: $(10.8)^2 - 82.0 = 116.6 - 82.0 = 34.6$ and number of η background events is given by formula 5.3: $N_{\eta\text{Background}} = 82.0 - 29.7 = 52.3$.

5.2 Consistency Checks

In order to prove the result for the branching ratio the analysis method has to be checked for stability by *consistency checks*. Consistency checks show the invariance of the branching ratio under variation of cuts, a different fit technique, rebining of histograms. Information about treatment of systematic errors can be found in [63] and [64]. Consistency checks have to be done for a certain set of cuts, where agreement between simulations and data is expected. As it was shown, (figure 4.28) the topological cuts and the cut on the missing mass of the decay products provide such agreement.

Schematically the data samples after certain set of cuts are shown in figure 5.2. Part of entire data sample by red filled area corresponds to subset of data after the set of cuts where agreement between simulations and data has been observed. Consistency checks will move inside the red filled area (for example blue filled) and will lead to other subsets of data where the branching ratio should not change significantly. If it does, then it points out to the systematic effect to be studied or fixed.

In this work the following consistency checks were done:

1. changing fit technique
2. changing cuts
3. rebining histograms

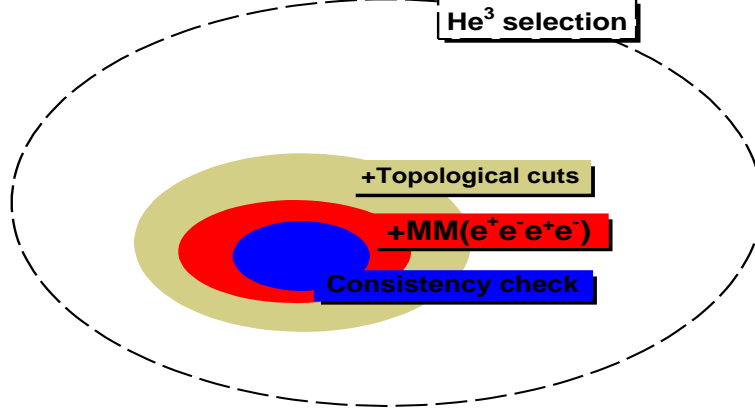


Figure 5.2: Schematic view of subsets of entire data sample: dashed oval corresponds to entire data sample after ³He selection, brown filled area corresponds to subset of data after the topological cuts, red filled area is after the cut on the missing mass of the decay products and blue filled area is due to narrowing the cut on the missing mass of decay products.

By fit technique the fit of prompt pions on the missing mass of ³He is meant: the background fit can be presented by different functions. By changing cuts different cut regions have to be considered. The branching ratio is calculated at each change in the analysis chain and eventually all results are compared. The total effect of each check is defined as a maximum deviation among presented measurements and the average: variation *var*. In such case the variation is the most informative and safe.

The variation of cut has certain constraints, in some cases it is limited by the resolution of observable σ and allows to expand the cut withing $\pm 4\sigma$ rule. Other constraint is due to the limitation of the analysis method itself: the cuts are supposed to describe certain preselected data sample, but not the entire one. Therefore if the result behaves stable under certain changes (inside certain range) and, suddenly, drops down or rise up, it might hint to the limit for this condition or cut. In order to judge about the contribution to the systematic error of cut the threshold σ_{Δ} is used given by the formula:

$$\sigma_{\Delta} = \sqrt{\sigma_2^2 - \sigma_1^2} \quad (5.4)$$

where σ_1 and σ_2 are statistical errors for different measurements of the branching ratio. By comparing σ_{Δ} and maximum deviation *var* first conclusion about the

Figure, row	$(BR \pm Er_{stat}) \times 10^{-5}$	$N_{candidates} \pm Er_{stat}$	$N_{\eta Data}$
Fig.5.3, upper	3.5 ± 1.1	36.0 ± 10.8	87.7 ± 10.8
Fig.5.1	2.9 ± 1.1	29.7 ± 10.8	82.0 ± 10.8
Fig.5.3, lower	3.7 ± 1.0	37.9 ± 10.3	86.1 ± 10.3
Result:	$BR = (3.4 \pm 1.1^{stat.} \pm 0.5^{var.}) \times 10^{-5}$		

Table 5.2: Measurements for the branching ratio calculations. The missing mass of ${}^3\text{He}$ is taken after the topological cuts and the cut of the decay products in the range $2.64 - 2.96 \text{ GeV}/c^2$. The prompt pion background was fitted by three different functions.

systematic effect is drawn.

5.2.1 Prompt Pion Subtraction

In order to check the effect by the prompt pion background on the branching ratio, the missing mass of ${}^3\text{He}$ is fitted by different functions and the branching ratio of $\eta \rightarrow e^+e^-e^+e^-$ is calculated for each case.

Three different ways of fitting the prompt pions fit are considered, see figure 5.3. In the first case, the background is fitted simply by a first order polynomial in the range outside of the η signal, see the top graph to the left. In the second case the ${}^3\text{He}$ missing mass is fitted by a second order polynomial which should describe the background shape more precisely than just a straight line, see the middle row. Finally the distribution is fitted by a combined function which is the sum of background and signal. In this case the background is described by the second order polynomial and η signal is described by a Lorentzian. All three methods are reasonable and should provide reasonable results.

The results for the branching ratio are presented in table 5.2. The average value for the branching ratio is 3.3×10^{-5} with the statistical error equals 1.1×10^{-5} . The variation of the result equals 0.4×10^{-5} . Thus, the branching ratio is: $BR = (3.4 \pm 1.1_{stat.} \pm 0.5_{var.}) \times 10^{-5}$.

5.2.2 Variation of cuts

Missing Mass of the Decay Products

The cut on the missing mass of the decay products $MM_{e^+e^-e^+e^-}$ is one of the cuts which suppresses pions, see figure 4.25. The cut region is defined by the resolution of this observable. According to Monte Carlo the $MM_{e^+e^-e^+e^-}$ distribution has a width of $\sigma = 60 \text{ MeV}/c^2$ and the corresponding range for the cut withing

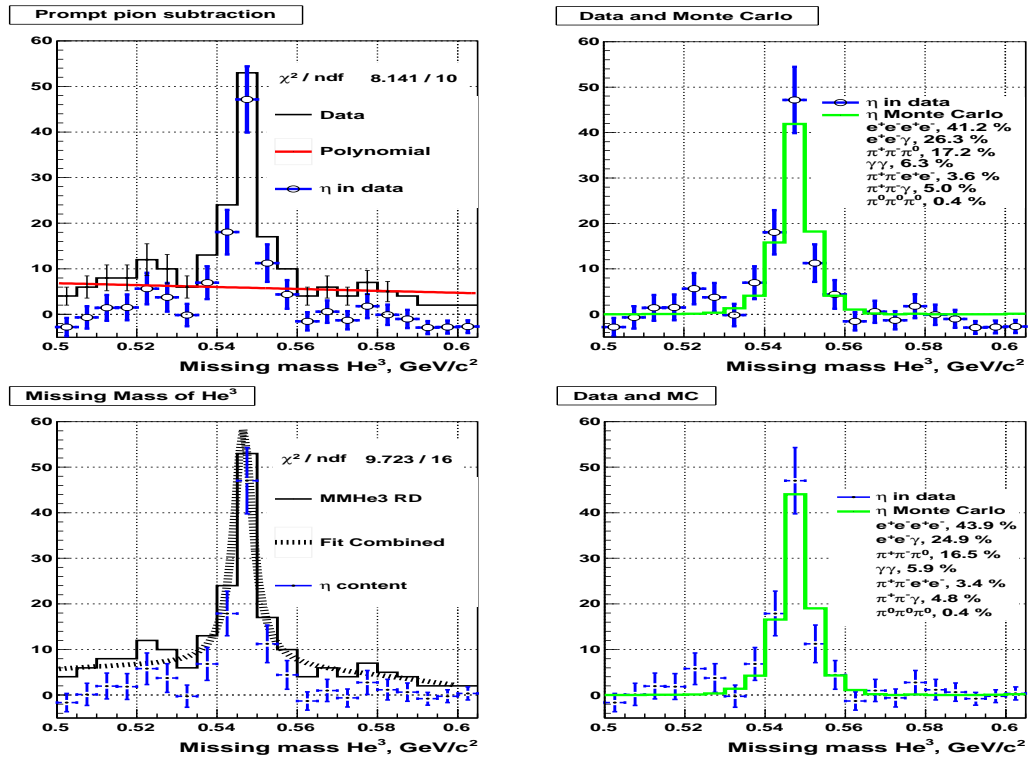


Figure 5.3: Left: missing mass ${}^3\text{He}$ after the topological cuts and the cut on the missing mass of the decay products $2.64 - 2.96 \text{ GeV}/c^2$, drawn in black, is fitted by two different functions: the polynomial of the first order on the upper left panel and combined function is on the lower left panel. Right: comparison of the corresponding η content in data with Monte Carlo sum of η channels.

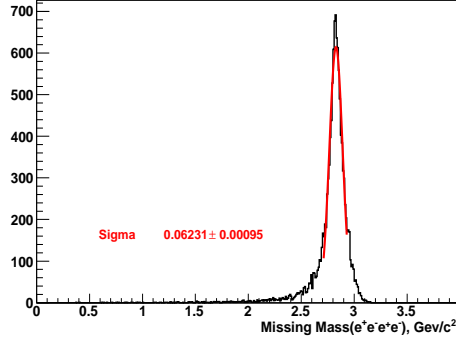


Figure 5.4: Missing mass of the decay products $MM_{e^+e^-e^+e^-}$ for the Monte Carlo simulation of the $\eta \rightarrow e^+e^-e^+e^-$. The distribution has a width of $\sigma \sim 60 \text{ MeV}/c^2$.

$\pm 3\sigma$ rule is around $(2.62 - 2.98) \text{ GeV}/c^2$, see figure 5.4. The maximum valid range for cut variation is defined by $\pm\sigma$ for the borders: $(2.56 - 3.04) \text{ GeV}/c^2$.

The effect of changing the cut regions on the branching ratio is shown in the table 5.3. A polynomial of second order was used for prompt pion subtraction. During these measurements the very narrow region $(2.68 - 2.92 \text{ GeV}/c^2)$ was tested, which implies the most significant rejection of events and poor statistics on the distribution. In order to present the fit of such a distribution properly the histogram binning was decreased, see figure 5.3. Also the widest cut region was tested. It implies more events on the distribution and corresponds to the situation with the highest admixture of prompt pions, see figure 5.5, lower row. In the right panel of this figure a slight discrepancy between Monte Carlo and data is observed in the η signal region. This can be explained by high admixture of prompt pions on ${}^3\text{He}$ missing mass, that makes their subtraction less accurate.

Slight fluctuations of the statistical error are observed, in the order of 10%. It can be ignored assuming the fact of a different distribution shape after the cut variation.

The average value for the branching ratio equals 2.7×10^{-5} , the maximum variation between the average and measured values is 0.4×10^{-5} . Thus, the branching ratio equals: $BR = (2.7 \pm 1.1_{stat.} \pm 0.4_{var.}) \times 10^{-5}$.

Invariant Masses of Lepton Pairs

The cut on the invariant mass of the lepton pairs is another cut for pion suppression during event selection. The variation of this cut is presented in the table 5.4. The cut on the missing mass of the decay products was taken in the range $2.64 - 2.96 \text{ GeV}/c^2$. With stricter cut the distribution becomes more flat which makes background fit easier. Average result: $BR = (3.1 \pm 1.1_{stat.} \pm 0.5_{var.}) \times 10^{-5}$.

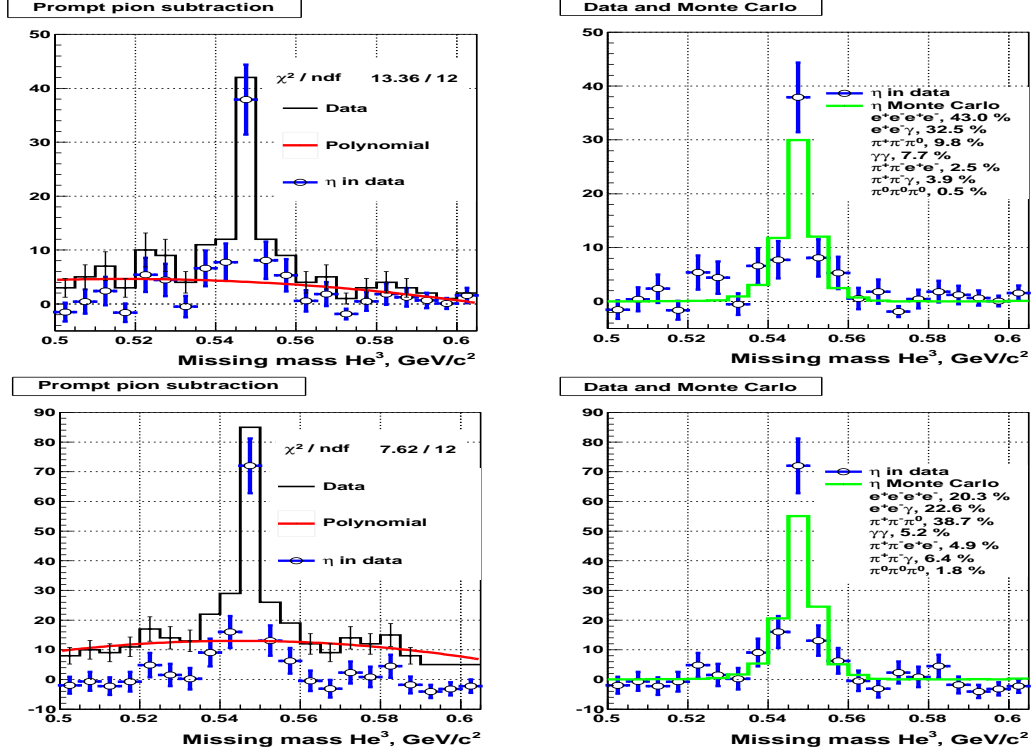


Figure 5.5: Left: missing mass of ${}^3\text{He}$ after the topological cuts and the cut on the missing mass of the decay products drawn in black, is fitted by the second order polynomial in red. Top: $2.68 - 2.92 \text{ GeV}/c^2$, lower: $2.56 - 3.04 \text{ GeV}/c^2$. Right: comparison of the η content in data with Monte Carlo sum of η channels.

Range, GeV/c^2 , Fig., row	$BR \pm Er_{stat}$	$N_{cand} \pm Er_{stat}$	$N_{\eta Data}$
(2.64-2.96), Fig.5.1	$(2.9 \pm 1.1) \times 10^{-5}$	29.7 ± 10.8	82.0 ± 10.8
(2.68-2.92), Fig.5.5, upper	$(2.5 \pm 1.0) \times 10^{-5}$	23.2 ± 9.4	58.0 ± 9.4
(2.56-3.04), Fig.5.5, lower	$(2.7 \pm 1.2) \times 10^{-5}$	29.8 ± 13.5	118.9 ± 13.5
(2.6-2.9), Fig.5.6, upper	$(2.5 \pm 1.0) \times 10^{-5}$	23.2 ± 9.7	58.4 ± 9.7
(2.62-2.96), Fig.5.6, lower	$(3.1 \pm 1.1) \times 10^{-5}$	32.1 ± 11.1	84.0 ± 11.1
Result:	$BR = (2.7 \pm 1.1^{stat.} \pm 0.4^{var.}) \times 10^{-5}$		

Table 5.3: Measurements for the branching ratio calculations with different cuts on the missing mass of the decay $\eta \rightarrow e^+e^-e^+e^-$ products. The polynomial of the second order was used for prompt pion subtraction.

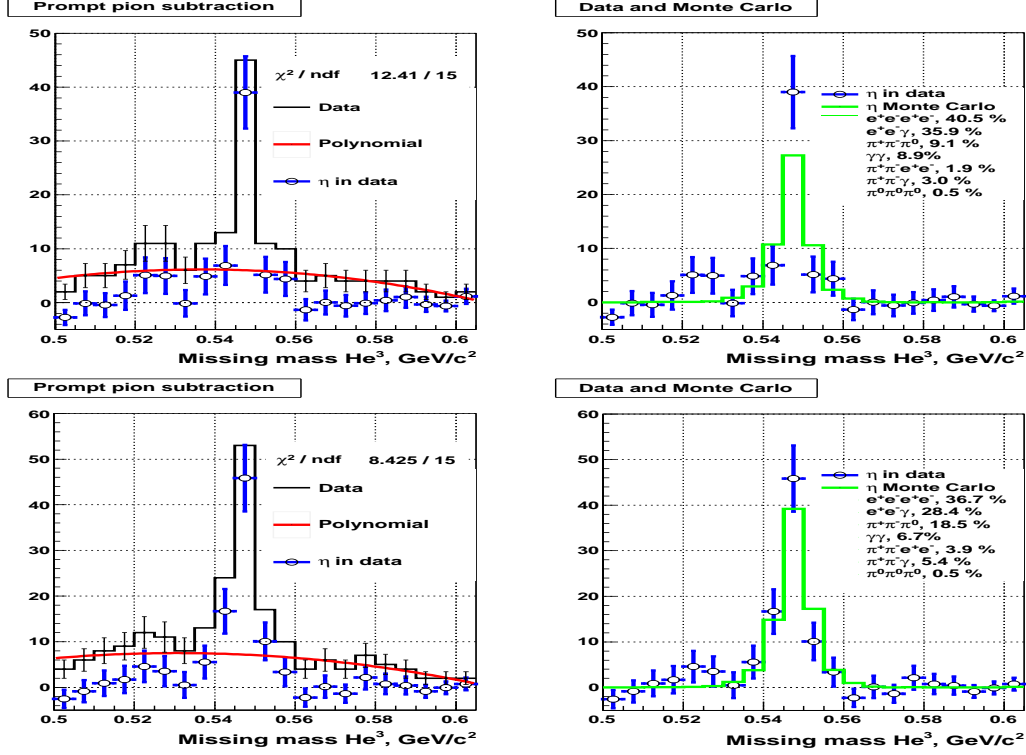


Figure 5.6: Analogically to the figure 5.5, top: $2.60 - 2.90 \text{ GeV}/c^2$, lower: $2.62 - 2.96 \text{ GeV}/c^2$.

Range $IM_{e^+e^-}$, GeV/c^2	$(BR \pm Er_{stat}) \times 10^{-5}$	$N_{cand} \pm Er_{stat}$	$N_{\eta Data}$
(0 - 0.1), Fig.5.1	2.9 ± 1.1	29.7 ± 10.8	82.0 ± 10.8
(0 - 0.12), Fig.5.7, top	3.4 ± 1.1	36.2 ± 11.9	93.9 ± 11.9
(0 - 0.08), Fig.5.7, lower	2.7 ± 1.0	25.9 ± 9.4	68.8 ± 9.4
(0 - 0.06), Fig.5.8, top	2.6 ± 1.0	22.1 ± 8.5	55.2 ± 8.5
(0 - 0.04), Fig.5.8, lower	3.6 ± 1.1	22.9 ± 7.3	44.0 ± 7.3
Result:	$BR(3.0 \pm 1.1_{stat.} \pm 0.4_{var.}) \times 10^{-5}$		

Table 5.4: Results for the branching ratio calculations with different cut on the invariant mass of the lepton pairs. Polynomial of a second order was used for prompt pion subtraction.

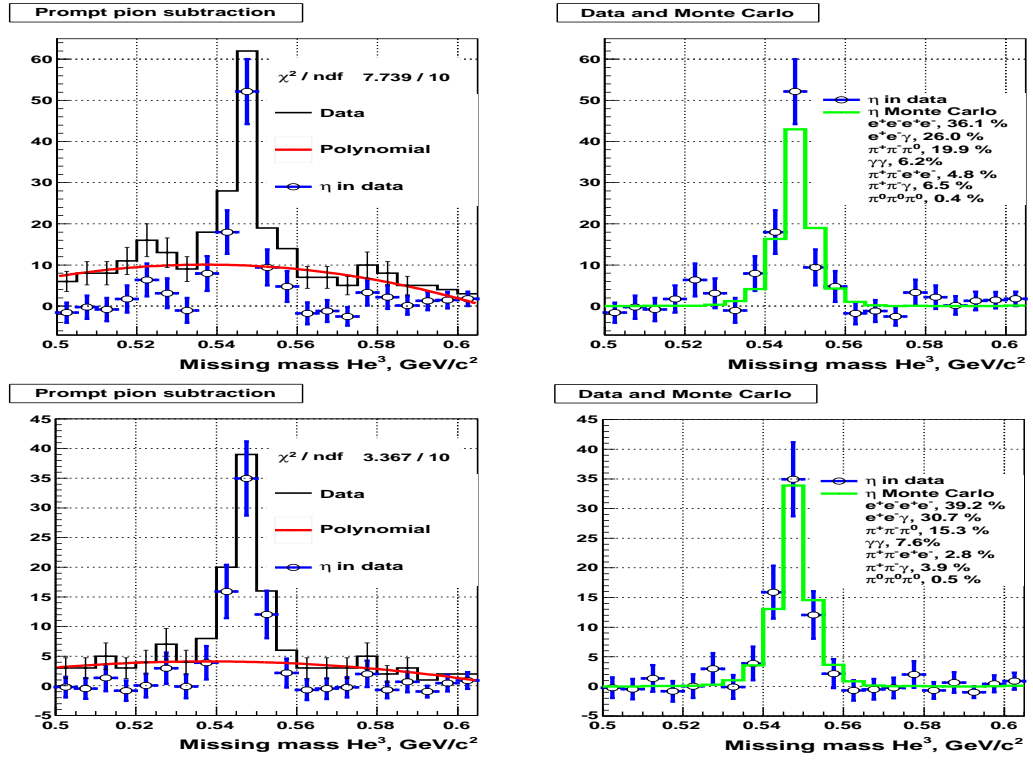


Figure 5.7: Missing mass of ${}^3\text{He}$ after changed topological cuts and the cut on the missing mass of the decay products $2.64 - 2.96 \text{ GeV}/c^2$. The cut on the invariant mass of the lepton pairs was tested: top: $IM_{e^+e^-} < 0.12 \text{ GeV}/c^2$, lower: $IM_{e^+e^-} < 0.08 \text{ GeV}/c^2$.

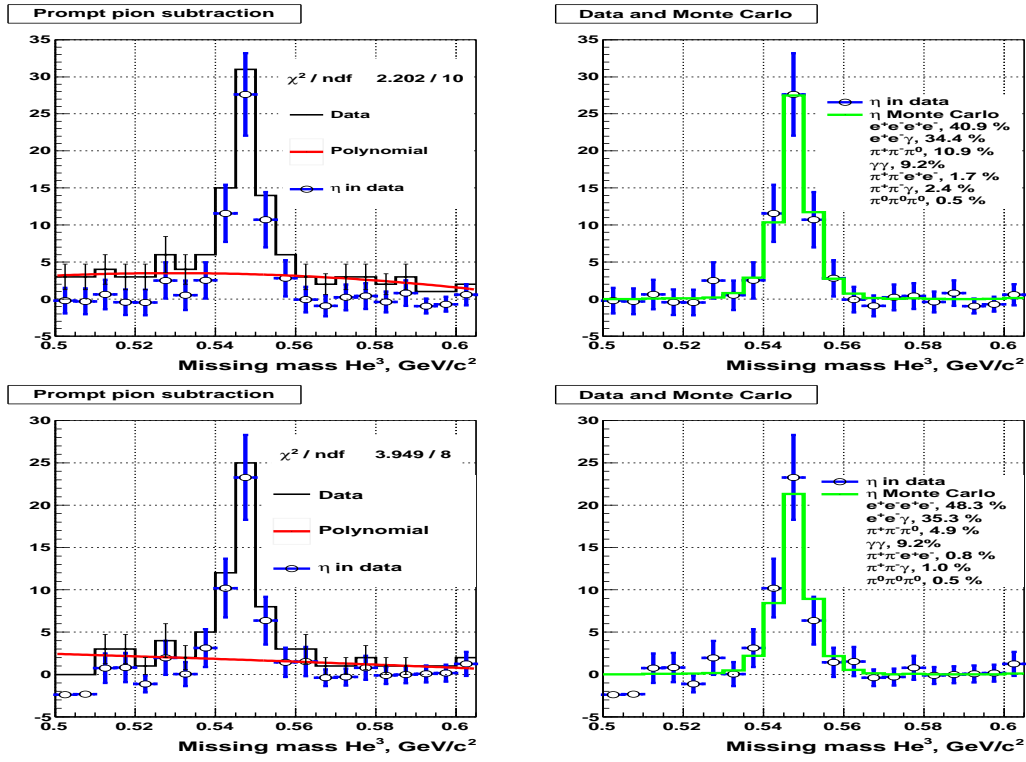


Figure 5.8: Missing mass of ${}^3\text{He}$ after the topological cuts and the cut on the missing mass of the decay products $2.64 - 2.96 \text{ GeV}/c^2$ and the cut on the invariant mass of the lepton pairs, top: $IM_{e^+e^-} < 0.06 \text{ GeV}/c^2$, lower: $IM_{e^+e^-} < 0.04 \text{ GeV}/c^2$.

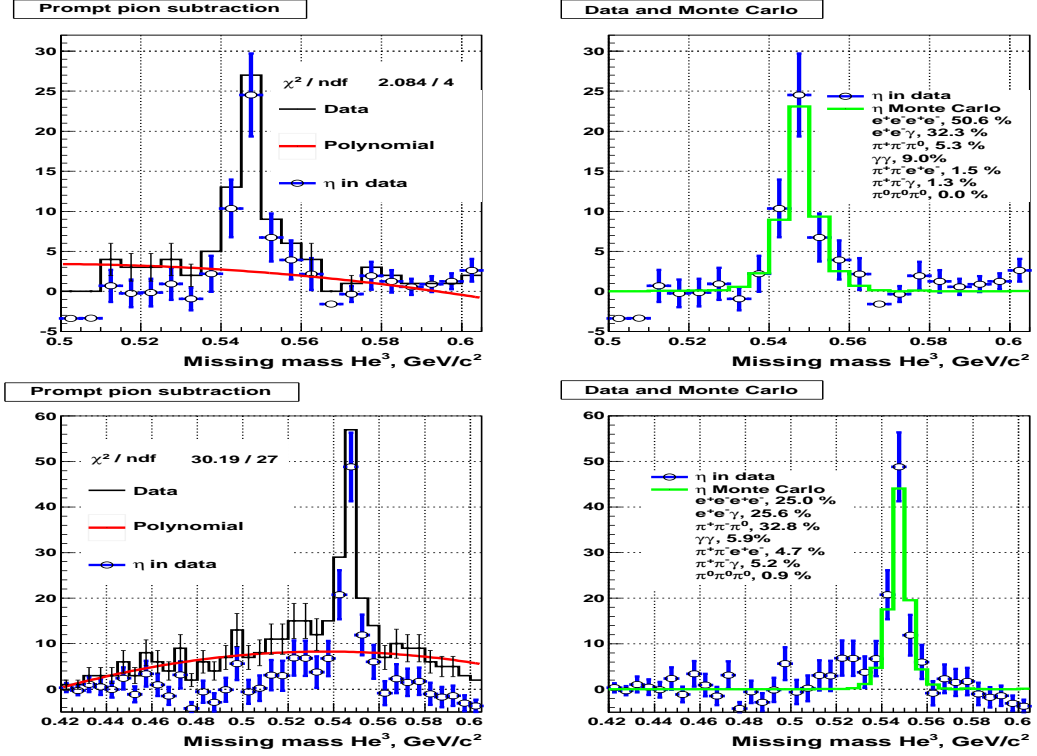


Figure 5.9: Missing mass of ${}^3\text{He}$ after the topological cuts and the cut on the missing mass of the decay products $2.64\text{--}2.96\text{ GeV}/c^2$ and the cut on the opening angles of the lepton pairs, top: $\Omega_{e^+e^-} < 20^\circ$, lower: $\Omega_{e^+e^-} < 60^\circ$.

Opening Angles of Lepton Pairs

The effect of varying the opening angle cut of the lepton pairs on the missing mass of ${}^3\text{He}$ is presented in figures 5.9 and 5.10. The results for the branching ratio are in the table 5.5. Average result: $BR_{\eta \rightarrow e^+e^-e^+e^-} = (2.6 \pm 1.1_{stat.} \pm 0.9_{var.}) \times 10^{-5}$. The variation by this cut is the largest among other cuts, it might hint to a problem with opening angle of the lepton pair. From the other hand, if one ignores the result by looser cut ($\Omega < 80^\circ$), then average branching ratio equals $BR = (2.9 \pm 1.1_{stat.} \pm 0.5_{var.}) \times 10^{-5}$. The grounds for this ignoring comes from the fact that 80° for the opening angle of the leptons pairs is too large and can not be controlled in this range. The results are shown in the table 5.5.

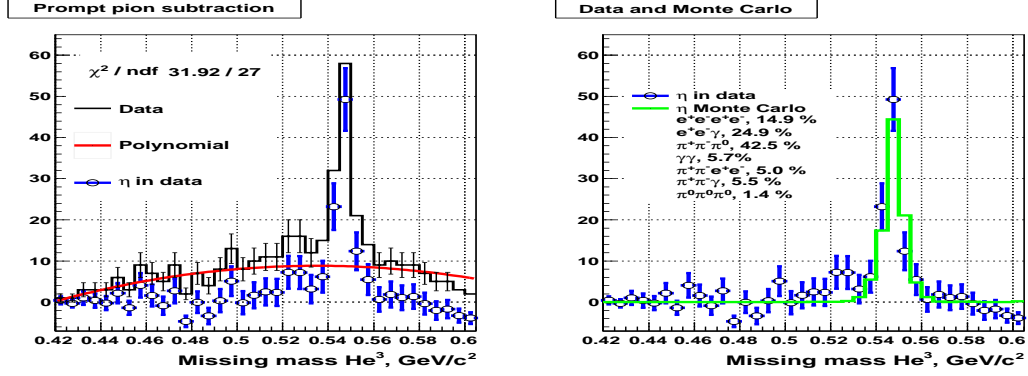


Figure 5.10: Missing mass of ${}^3\text{He}$ after the topological cuts and the cut on the missing mass of the decay products $2.64\text{--}2.96\text{ GeV}/c^2$ and the cut on the opening angles of the lepton pairs, $\Omega_{e^+e^-} < 80^\circ$.

Range, Fig., row	$(BR \pm Er_{stat}) \times 10^{-5}$	$N_{cand} \pm Er_{stat}$	$N_{\eta Data}$
$(0^\circ - 20^\circ)$, Fig.5.9, upper	3.4 ± 1.1	24.0 ± 7.7	45.7 ± 7.7
$(0^\circ - 40^\circ)$, Fig.5.1	2.9 ± 1.1	29.7 ± 10.8	82.0 ± 10.8
$(0^\circ - 60^\circ)$, Fig.5.9, lower	2.4 ± 1.0	26.9 ± 11.6	95.6 ± 11.6
$(0^\circ - 80^\circ)$, Fig.5.10	1.7 ± 1.1	18.8 ± 11.8	97.7 ± 11.8
Result:	$BR = (2.6 \pm 1.1^{stat.} \pm 0.9^{var.}) \times 10^{-5}$		
Result (ignore last):	$BR = (2.9 \pm 1.1^{stat.} \pm 0.5^{var.}) \times 10^{-5}$		

Table 5.5: Results for the branching ratio calculations with different cut on the opening angles of the lepton pairs. Polynomial of a second order was used for prompt pion subtraction.

Type of events	$(BR \pm Er_{stat}) \times 10^{-5}$	$N_{cand} \pm Er_{stat}$	$N_{\eta Data}$
Fig.5.11, top	3.7 ± 1.0	37.9 ± 10.3	82.9 ± 10.3
Fig.5.11, lower	2.4 ± 0.9	24.3 ± 9.3	67.6 ± 9.3
Result:	$BR = (3.1 \pm 1.0^{stat.} \pm 0.7^{var.}) \times 10^{-5}$		

Table 5.6: Results for the branching ratio for different types of events: multi-track events (figure 5.11, top) and events with exactly two positively and exactly two negatively charged tracks (figure 5.11, lower).

5.3 Systematic Effect by Event Overlap

Event overlap in data (discussed in 4.5.1) was studied as another source of systematic effect.

Effect of event overlap can add an additional track or even several tracks to the final state of the decay. This extra track can pass through the cuts and substitute a good track. The effect is not included in simulations and therefore influences only the data. In order to evaluate this effect on the branching ratio the events only with exactly two positively and exactly two negatively charged tracks were considered. Obtained result was compared with multi-track events.

The effect is shown in figure 5.11: top row shows distributions based on multi-track events and lower row corresponds to events with exactly two positively and exactly two negatively charged tracks. The plot on top has been shown already with fitting the prompt pion background in slightly more narrow range. Here the fitting range was extended ($0.47 - 0.59 GeV/c^2$) in order to be as much as possible to the range on the plot below, where it was necessary to extend the range for a good fit.

Immediate effect in statistics of the histograms is visible: the lower plot contains 20% less events than upper one due to consideration of exact number of tracks. Number of signal event candidates drops down, that results in lower branching ratio. At the same time the statistical error remains almost the same, that hints to systematic error. The maximum deviation is 0.7×10^{-5} for the branching ratio, see table 5.6.

Results for the branching ratio

Thus, four results for the branching ratio were obtained and summarized in the table 5.7. The last column contains the threshold for passing the check σ_{Δ} , which was obtained according to the formula 5.4. In traditional way of analysis the results can be averaged for the final number and variations can be summed up under the root squared and signed to the systematic error. Considering threshold for each variation the conclusion would be different: the consistency check passes (does not

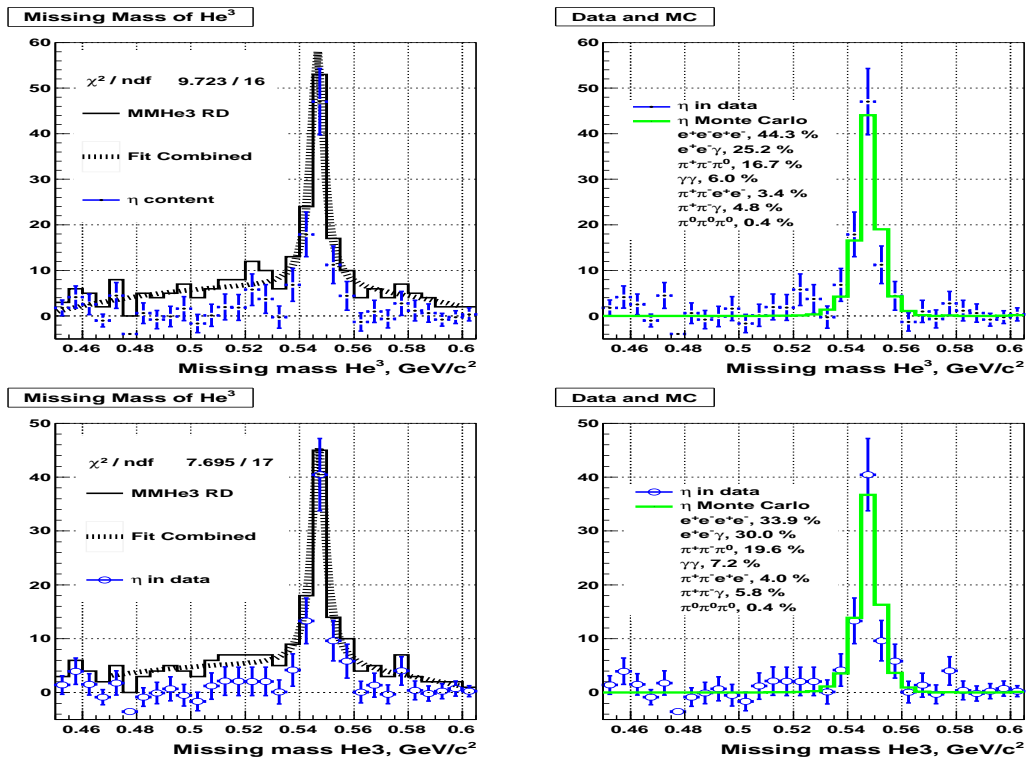


Figure 5.11: Missing mass of ${}^3\text{He}$ after the topological cuts and the cut on the missing mass of the decay products $2.64 - 2.96$, top: multi-track events were considered (as all other pictures), lower: events with exactly two positively and exactly two negatively charged tracks were considered.

Source of variation	$(BR \pm Er_{stat} \pm var) \times 10^{-5}$	Threshold, $\sigma_{\Delta} \times 10^{-5}$
Missing mass of $(e^+e^-e^+e^-)$	$2.7 \pm 1.1 \pm 0.4$	0.7
Invariant masses of (e^+e^-)	$3.0 \pm 1.1 \pm 0.4$	0.5
Opening angles of (e^+e^-)	$2.6 \pm 1.1 \pm \mathbf{0.9}$	0.5
Event overlap	$3.1 \pm 1.0 \pm \mathbf{0.7}$	0.4
Average	2.9 ± 1.1 (stat) ± 1.3 (syst.trad.)	

Table 5.7: Results for the branching ratio with variations var and thresholds for variation σ_{Δ} .

have a systematic effect) if it is lower than the corresponding threshold. As can be seen the variation due to the opening angle cut is 0.9, greater than the threshold 0.5. The variation caused by effect of event overlap is also above the threshold: $0.7 > 0.4$. Therefore, these consistency checks do not pass and have significant systematic effect to be studied.

Chapter 6

Conclusion and discussions

The branching ratio for the $\eta \rightarrow e^+e^-e^+e^-$ decay was calculated based on the missing mass of ${}^3\text{He}$ as $(2.9 \pm 1.1_{(stat)}) \times 10^{-5}$. The result agrees with expectations from quantum electrodynamics within the statistical error, which is $\sim 38\%$. The achieved maximum admixture of $\eta \rightarrow e^+e^-e^+e^-$ decay candidates is 50.6%, which corresponds to a signal to background ratio $\sim 1 : 1$. The single Dalitz decay $\eta \rightarrow e^+e^-\gamma$ shows a similar signal to background ratio with similar ideology of the analysis chain. In both cases the ratio can be improved by suppressing the main background due to photon conversion. The other significant background originates from the hadronic mode $\eta \rightarrow \pi^+\pi^-\pi^0$ (5 % in the optimum case) which can be suppressed by involving particle identification in future analyses.

The remarkable point is that the branching ratio shows stability for different fractions of η -decays. See for example variations of the $\eta \rightarrow e^+e^-e^+e^-$ admixture from 20.3 % to 43.0 %, while at the same time the $\eta \rightarrow \pi^+\pi^-\pi^0$ admixture is suppressed from 38.7 % to 9.8 %, in figure 5.5. This confirms the stability of the analysis chain.

The calculated variations of the branching ratio passed the threshold σ_Δ for two checks: changing the missing mass of the decay products and the invariant masses of the lepton pairs. Two other checks showed the variations above the threshold: the opening angles of the lepton pairs and the effect by event overlap.

Consistency checks have to be done for other possible uncertainties of the branching ratio. Among them three are of special importance: the total number of η -mesons produced in experiment, the hypothetical spatial resolution for charged track reconstruction in the central detector and the event overlap in data. The number of η -mesons was calculated based on a sample of ~ 14000 decay events of η -single Dalitz decays, where the events with exactly one positively and exactly one negatively charged track were considered. At this stage the analysis ideology differs for single and double Dalitz decays of η : in the last case multi-track events were considered.

Twice more η -mesons (2×10^7) have been produced in the same reaction and similar conditions as discussed in the thesis ($pd \rightarrow {}^3\text{He}\eta$ at 1 GeV) during a production run in September 2009. Furthermore, a statistically more abundant sample of η mesons is expected from the reaction $pp \rightarrow pp\eta$ at 1.4 GeV beam energy (discussed in 4), taken during a production run in November 2009, although here the background is very different compare to $pd \rightarrow {}^3\text{He}$ at 1 GeV.

Studies of other rare decays of η , like $\eta \rightarrow e^+e^-$, $\eta \rightarrow \pi^0e^+e^-$, $\eta \rightarrow e^+e^-\gamma$ are currently going on in WASA-at-COSY collaboration. They should be coordinated between each other and be complementary, since all of them have lepton pair(s) in the final state.

Chapter 7

Appendix

A. Time diagram of tracks of η double Dalitz event candidates in data.

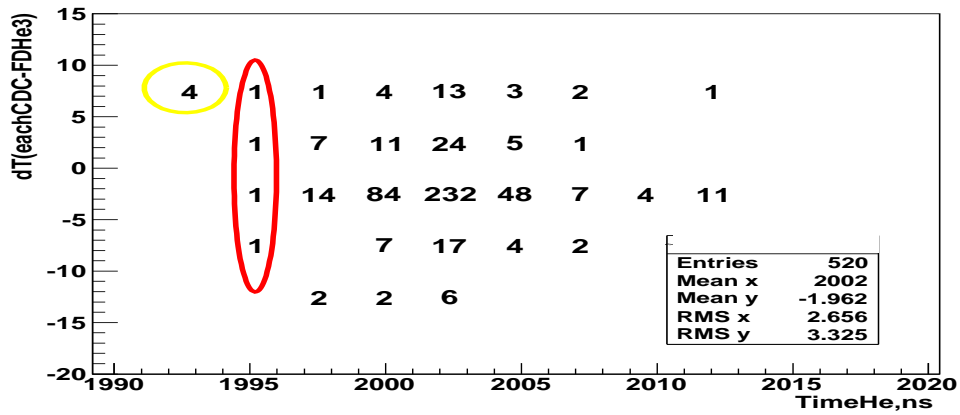


Figure 7.1: Time diagram of tracks of η double Dalitz event candidates in data: time difference between each lepton candidate and ${}^3\text{He}$ track in the Forward Detector on the Y -axis, time of the ${}^3\text{He}$ track on the X -axis. The events after the topological cuts ($IM_{e^+e^-} < 0.1\text{GeV}/c^2$, $\Omega_{e^+e^-} < 40^\circ$, $\Phi_{L_1,L_2} = (85^\circ - 175^\circ)$), the cut on the missing mass of the decay products in the range $(2.62 - 2.98)\text{GeV}/c^2$ and the cut on the missing mass of ${}^3\text{He}$ is in the range $(0.535 - 0.560)\text{GeV}/c^2$. By yellow circle a good example of event is marked: all four tracks in the central detector has the same time within one bin (5 ns). By red ellipse an example of critical event is marked: four tracks in the central detector have wide time interval relatively to the time of ${}^3\text{He}$ track. As can be seen most of the tracks are very close in time.

B. Particle identification in calorimeter for η –single Dalitz in data.

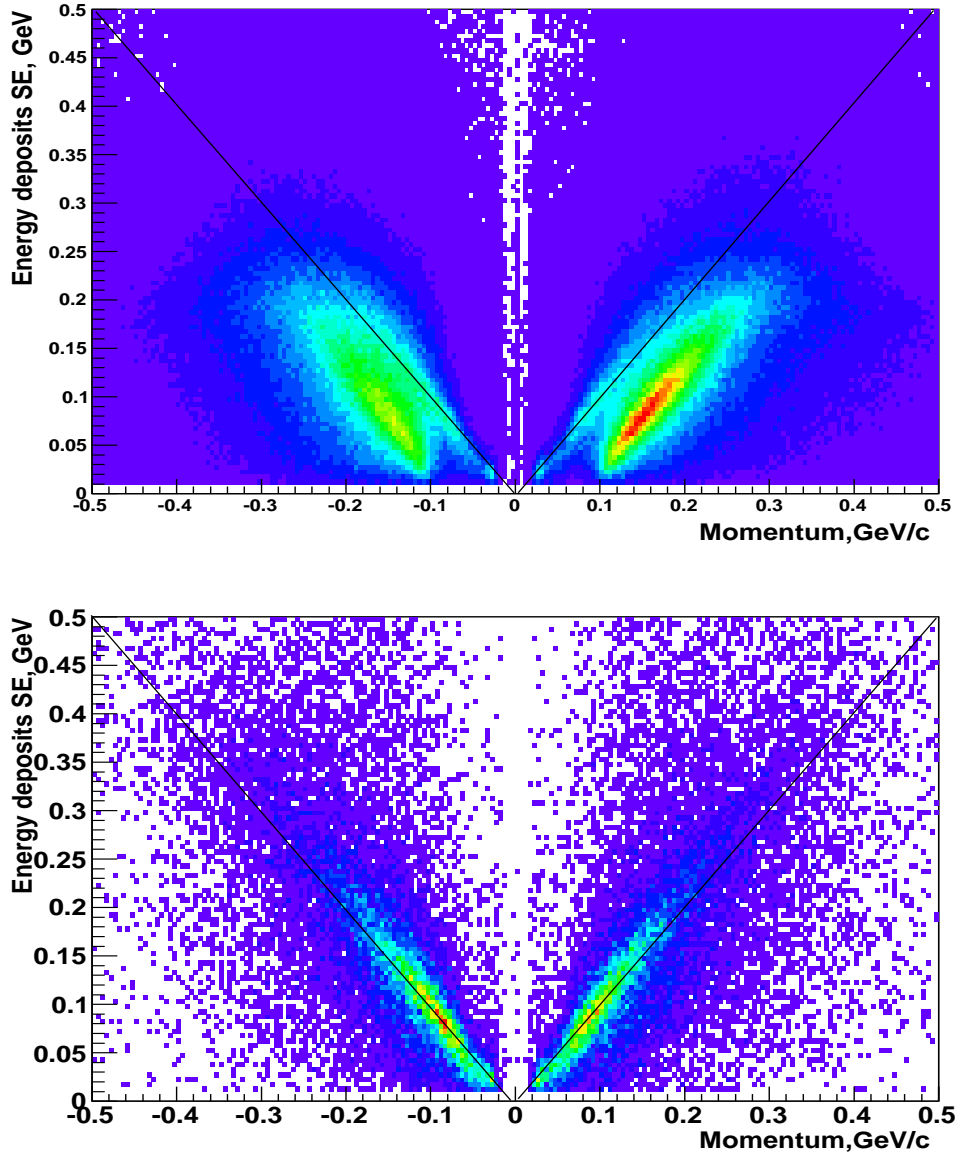


Figure 7.2: Experimental data: energy deposit in calorimeter versus particle momentum \times charge provided by the mini drift chamber. Black diagonals represent linear correlation between energy and momentum, which is the signature of electrons and positrons. Upper panel: after track selection for $\eta \rightarrow e^+e^-\gamma$ decay, lower panel: after the cut on the missing mass of $e^+e^-\gamma$ ($2.65 - 2.95$) GeV/c^2 , invariant mass of lepton pair < 0.1 GeV/c^2 and the missing mass of ${}^3\text{He}$ ($0.535 - 0.560$) GeV/c^2 .

C. Particle identification in calorimeter for η -double Dalitz in data.

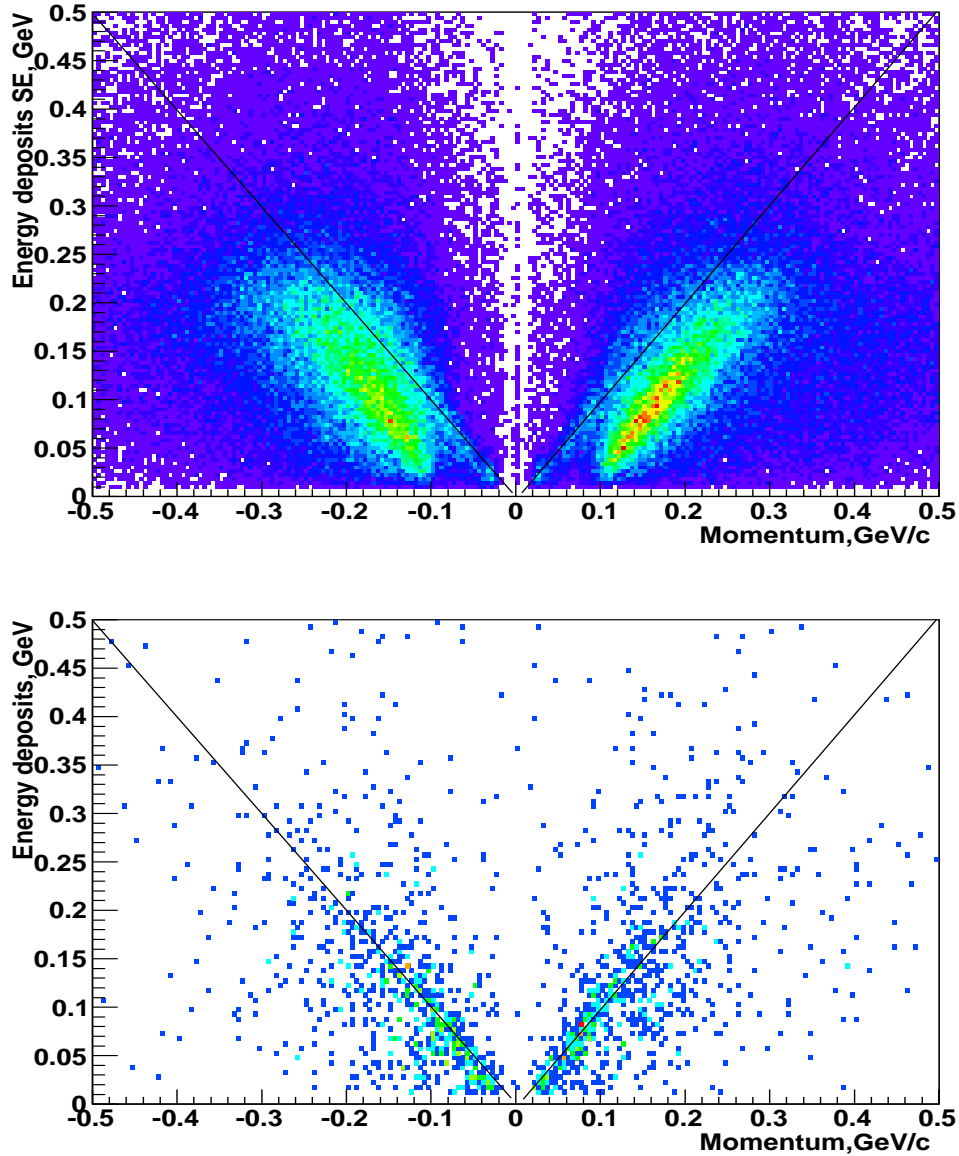


Figure 7.3: Experimental data: energy deposit in calorimeter versus particle momentum \times charge provided by the mini drift chamber. Black diagonals represent linear correlation between energy and momentum, which is the signature of electrons and positrons. Upper panel: after track selection for $\eta \rightarrow e^+e^-e^+e^-$ decay, lower panel: after the cut on the missing mass of $e^+e^-e^+e^-$ ($2.62 - 2.98$) GeV/c^2 , invariant masses of the lepton pairs < 0.1 GeV/c^2 , opening angles of the lepton pairs $\Omega < 40^\circ$ and the missing mass of ${}^3\text{He}$ ($0.535 - 0.560$) GeV/c^2 .

D. Individual missing mass of ${}^3\text{He}$ distributions for Monte Carlo η -decays in comparison with data.

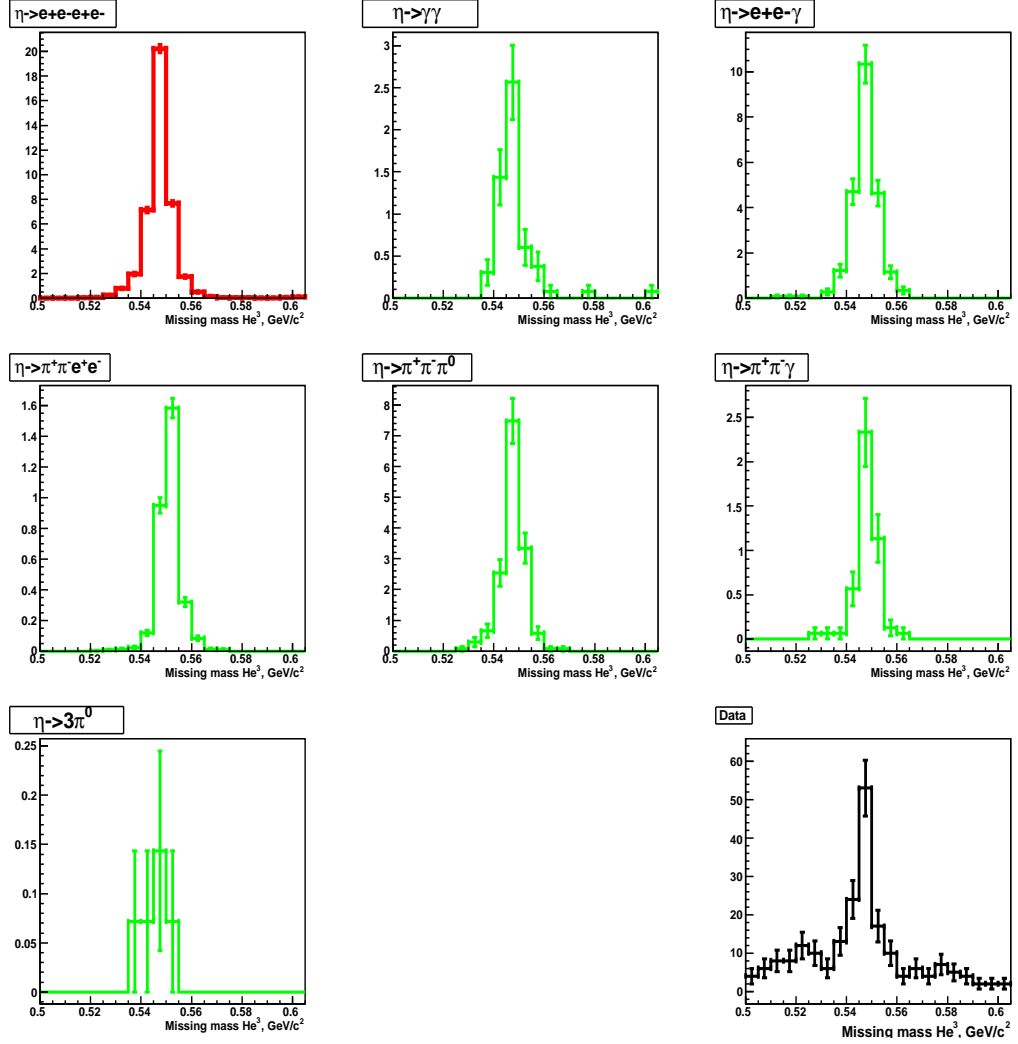


Figure 7.4: Individual missing mass of ${}^3\text{He}$ for each η Monte Carlo channel after the topological cuts invariant masses of lepton pairs $< 0.1 \text{ GeV}/c^2$, opening angles of the lepton pairs $\Omega < 40^\circ$, opening angle between the lepton pairs Φ_{L_1, L_2} is in the range $(85^\circ - 175^\circ)$ and the cut on the missing mass of the decay products in the range $(2.64 - 2.96) \text{ GeV}/c^2$. Each Monte Carlo distribution is normalized to the data according to formula 4.2, the number of η -s produced in experiment is taken as 9.6×10^6 . The error bars correspond to the absolute statistical errors defined by number of simulated events (before the normalization).

Bibliography

- [1] E. Noether, Nachr. D. König. Gesellsch. D. Wiss. Zu Göttingen, Math-phys. Klasse 1918, 235-257.
- [2] V. Koch, Aspects of Chiral Symmetry, arXiv:nucl-th/9706075v2, 27 Jun 1997.
- [3] M. Berlowski et al. Measurement of lepton decays of the η meson, arXiv:0711.3531v2 [hep-ex/0608031], 2007.
- [4] A. Pevsner et al., Evidence for a three-pion resonance near 550 MeV, Phys. Rev. Lett. 7, 421–423, 1961
- [5] T. N. Pham. $\eta - \eta'$ mixing angle from Vector Meson Radiative Decays. arXiv:1005.5671v3, 13 Sep 2010.
- [6] A. Bramon, R. Escribano and M. D. Scadron. The $\eta - \eta'$ mixing angle revisited. arXiv:hep-ph/9711229v2, 14 May 1998.
- [7] K. Nakamura et al. (Particle Data Group), Review of particle physics, J. Phys. G37 075021, 2010
- [8] D.H. Miller et al. (CLEO Collaboration), Measurement of the η -Meson Mass Using $\psi(2S) \rightarrow \eta J/\psi$, Phys. Rev. Lett. 99 122002, 2007 [arXiv: 0707.1810[hep-ex]]
- [9] F. Ambrosino et al. (KLOE Collaboration), Precise measurements of the η and the neutral kaon meson masses with the KLOE detector, JHEP 12(2007)073 [arXiv: 0710.5892[hep-ex]]
- [10] A. Lai et al. (NA48 Collaboration), New measurements of the η and K^0 masses, Phys. Lett. B533 196-206, 2002
- [11] B.M.K. Nefkens, Rare and not-so-rare decays of light mesons, in *Meson production, interaction and decay: proceedings*, edited by A. Magiera, W. Oelert, E. Grosse, World Scientific, River Edge, NJ, 1991, pp. 40–64

- [12] S. Kullander et al., Rare η Decays and the CP Symmetry, *Acta Phys. Polon. B* 29 97-111, 1998
- [13] M. Wolke, Measurements of η' Decays using WASA@COSY.
- [14] L.G. Landsberg, Electromagnetic decays of light mesons, *Phys. Rept.* 128, 301–376, 1985
- [15] I. Froehlich et al. Pluto: A Monte Carlo Simulation Tool for Hadronic Physics. arXiv:0708.2382v2 [nucl-ex] 6 Nov 2007
- [16] R. I. Djhelyadin et al., *Phys. Lett. B* 94, 548 (1980)
- [17] J. Stepaniak et al., *Phys. Scripta*, T99, 133 - 139 (2002)
- [18] R.H. Dalitz, On an alternative decay process for the neutral π -meson, Letters to the Editor, *Proc. Phys. Soc. A*64, 667-669 (1951)
- [19] R. R. Akhmetshin *et al.* Study of conversion decays $\Phi \rightarrow \eta e^+ e^-$, $\eta \rightarrow e^+ e^- \gamma$ and $\eta \rightarrow \pi^+ \pi^- e^+ e^-$ at CMD-2. *Physics Letters B* 501, p. 191-199, 2001.
- [20] M. Berlowski *et al.* Measurement of η Meson Decays into Lepton-Antilepton Pairs, *Physical Review*, D77, p. 032004, 2008
- [21] C. Jarlskog, H. Pilkuhn, Eta decays with $e^+ e^-$ and $\mu^+ \mu^-$ pairs, *Nucl. Phys. B* 1 264–268, 1967
- [22] N. M. Kroll and W. Wada, Internal Pair Production Associated with the Emission of High-Energy Gamma Rays, *Phys. Rev.* 98, 1355 - 1359, (1955)
- [23] J. Bijnens, J. Gasser, Eta Decays at and Beyond p^4 in Chiral Perturbation Theory, *Phys. Scripta T* 99 34-44, 2002
- [24] T. Miyazaki, E. Takasugi, Internal Conversion of Pseudoscalar Mesons Into Lepton Pairs, *Phys. Rev. D* 8 2051-2062 (1973)
- [25] J. Bijnens and F. Persson. Effects of different Form-factors in Meson-Photon-Photon Transitions and the Muon Anomalous Magnetic Moment, 13 June 2001, arXiv: hep-ph/0106130.
- [26] T. Petri, Anomalous decays of pseudoscalar mesons, arXiv: 1010.2378v1 [nucl-th], October 2010.

- [27] P. Herczeg, Exotic Decays of Light Mesons, Int. Workshop on Production and Decay of Light Mesons, Paris, Mar 3, 1988, proc. ed. by P.Fleury, World Scientific, Singapore (1988) p.16
- [28] J.Bijnens, in Chiral Dynamics: Theory and Experiment, eds. A.M.Bernstein, D.Drechsel and T.Walcher, Mainz, Springer, 1997.
- [29] Djhelyadin, R. I. *et al.*, Phys. Lett. B 94, 548 (1980)
- [30] Official web-site of the KLOE collaboration: <http://www.lnf.infn.it/kloe>.
- [31] M. Jacewicz, "Measurement of the Reaction $pp \rightarrow pp\pi^+\pi^-\pi^0$ with CELSIUS/WASA at 1.36 GeV".
- [32] R. Maier et al. Cooler synchrotron COSY, Nucl. Phys., A626:395c-403c, 1997.
- [33] D. Prasuhn et al. Electron and stochastic cooling at COSY, Nucl. Instruments and methods., A441:167-174, 2000.
- [34] C. Ekstrom and The CELSIUS/WASA Collaboration, The CELSIUS/WASA Pellet Target System, Physica Scripta. T99, 169-172, 2002.
- [35] M. Capeans. Aging of Gaseous Detectors: assembly materials and procedures, CERN
- [36] Official web-site of the CMS collaboration: <http://www-hep.phys.cmu.edu/cms>.
- [37] L. Yurev, Performance of the MDC - Central Part of the WASA - before installation at COSY, 2006
- [38] R. J. M. Y. Ruber et al. An ultra-thin-walled Superconducting Solenoid for Meson-decay Physics, Uppsala University, 1999
- [39] R.J.M.Y. Ruber. Radiation hardness test of CsI crystals for WASA, WASA Report 2/90, 1990
- [40] I. Koch. Measurement of $2\pi^0$ and $3\pi^0$ Production in Proton-Proton Collisions at a Center of Mass Energy of 2.465 GeV. PhD thesis, Uppsala Universitet, Sweden, 2004.
- [41] C. Redmer, In search of the Box-Anomaly with the WASA facility at COSY, March 2010

- [42] C. Pauly et al. A scintillator hodoscope for experiments at proton storage rings, 2005
- [43] J. Zabierowski, J. Rachowski, The Light-Pulser Monitoring System for the WASA detector facility, 2009
- [44] K. Zwoll et al. Flexible data acquisition system for experiments at COSY. IEEE Trans. Nucl. Sci., 41: 37-44, 1994
- [45] Root homepage, <http://root.cern.ch>
- [46] M. A. Kagarlis, GSI Report 2000-03 (2000), unpublished
- [47] CERN Program Library Long Writeup W5013. GEANT - Detector Description and Simulation Tool, 1993.
- [48] S. Baranov, A. Glazov, V. Donov. Autocalibration method for determination of drift time-space relation for HPDT", ATLAS Internal Note MUON-NO-040, 4 May 1994
- [49] P. Podkopal, Energy calibration of the WASA Plastic Scintillator Barrel, IKP Annual Report, 2006
- [50] Volker Hejny, Calorimeter calibration, internal document on the webpage of the WASA collaboration.
- [51] Komogorov M., Morosov B., Povtorejko A., Tikhomirov V. Track recognition algorithm for WASA Mini Drift Chamber (MDC) Version 1.0, WASA memo 97-11, 1997
- [52] R. Kalman, Trans. ASME, J. Basic Engineering (1960)
- [53] R.K Bock, H. Grote, D. Notz and M. Regler. Data analysis techniques for high-energy physics experiments., Cambridge University Press, 1990
- [54] Greg Welch and Gary Bishop, An Introduction to the Kalman Filter, 2006
- [55] William R. Leo, Techniques for Nuclear and Particle Physics Experiments. Springer-Verlag (1994)
- [56] E. Chiavassa et al. Measurement of the $pp \rightarrow pp\eta$ total cross section between 1.265 GeV and 1.50 GeV. *Phys. Lett.*, B322:270-274, 1994
- [57] R. Bilger et al. Measurement of the $pd \rightarrow {}^3\text{He}\eta$ cross section between 930 and 1100 MeV, Physical Review C, VOLUME 65, 044608 (2002)

- [58] C. Zheng. Matching Trigger Efficiency of Forward Detector of WASA-at-COSY. IKP, Annual Report, 2008.
- [59] J. Zlomanczuk. Uppsala Universitet, Sweden, web-site, <http://www4.tsl.uu.se/jozef/WasaCosy/Odin/Odin.html>, e-mail: jozef.zlomanczuk@fysast.uu.se, phone: +46 (0)18 471 1587.
- [60] K. Schönning *et al.*. Production of η and 3π mesons in the $pd \rightarrow {}^3\text{He}X$ reaction at 1360 and 1450 MeV, 2010.
- [61] M. Bashkanov *et al.*, Exclusive Measurements of $pd \rightarrow {}^3\text{He}\pi\pi$: the ABC Effect Revisited, arXiv:nucl-ex/050811v3 10 Sep 2006.
- [62] A. De Santis for the KLOE collaboration, Recent Results from KLOE, arXiv:0805.2521v1 [hep-ph], 2008
- [63] R. Barlow, "Systematic errors: facts and fictions".
- [64] R. Barlow, "Introduction to Statistical Issues in Particle Physics", PHYS-TAT2003, SLAC, Stanford, California, September 8-11, 2003.

List of Figures

1.1	Meson octet	4
1.2	Diagrams for the η -meson	8
1.3	Surface plot for momentum squared	9
1.4	Form factor influence	9
2.1	COSY floor plan	14
2.2	Beam cycle	16
2.3	pelletSetup	17
2.4	Photo of the pellet stream	17
2.5	WASA cross section	19
2.6	MDC views	20
2.7	MDC construction	21
2.8	MDC layer efficiency	22
2.9	PSB parts	23
2.10	One PSB element	24
2.11	Magnetic field inside iron yoke	25
2.12	SEC schematic view	26
2.13	One SEC element	26
2.14	FWC photo	27
2.15	FPC modules	29
2.16	Forward Trigger Hodoscope	29
2.17	Forward Range Hodoscope	30
2.18	The FRI	31
2.19	The FVH	31
2.20	DAQ scheme	33
2.21	Trigger system scheme	34
3.1	Data analysis scheme	36
3.2	T_0 determination in the MDC	41
3.3	Calibrated time in the MDC	41
3.4	Drift function of the MDC	41

3.5	Helix and magnetic field	44
3.6	Helix parameters	44
3.7	Momentum reconstruction by PR and FF	46
3.8	Momentum resolution with different spatial resolutions	47
3.9	Efficiencies of different pattern recognition algorithms	48
3.10	Efficiencies in 2-D plots	48
3.11	Matching scheme for CD track finder	51
3.12	Azimuthal angle difference between the MDC and PSB clusters	52
3.13	Opening angle between the MDC and SEC clusters	52
3.14	Difference between azimuthal angles of the PSB and SEC clusters	53
3.15	Particle identification in the central detector	54
3.16	Particle identification in the CD, data	55
3.17	Particle identification, $\eta \rightarrow e^+e^-e^+e^-$	56
3.18	Particle identification, $\eta \rightarrow e^+e^-\gamma$	56
3.19	Particle identification in the Forward Detector	57
4.1	Unbiased missing mass of ${}^3\text{He}$, experimental data	60
4.2	Beam cycle in beamtime 2008	62
4.3	Signal of the η in data	63
4.4	${}^3\text{He}$ identification in data	65
4.5	The signature of the two body reaction $pd \rightarrow {}^3\text{He}X$	65
4.6	${}^3\text{He}$ identification in data	69
4.7	The time difference charged tracks	70
4.8	D_0 distance in data	70
4.9	Time difference neutral tracks	70
4.10	Photons energy in Monte Carlo simulation of $\eta \rightarrow e^+e^-\gamma$	70
4.11	The opening angle between real and virtual photons	71
4.12	Topology of single Dalitz of the η	72
4.13	Topology of single Dalitz of the η in data	73
4.14	The missing mass of ${}^3\text{He}$ developing in data, single Dalitz	74
4.15	${}^3\text{He}$ missing mass after final cuts for $\eta \rightarrow e^+e^-\gamma$ tagging	76
4.16	Invariant mass of lepton pair in $\eta \rightarrow e^+e^-\gamma$ studies	76
4.17	Prompt pion subtraction, polynomial, single Dalitz	77
4.18	η content in data and simulations	77
4.19	Prompt pion subtraction, combined function, single Dalitz	78
4.20	η content in data and simulations, using combined function	78
4.21	Event candidate for $\eta \rightarrow e^+e^-e^+e^-$	81
4.22	Topology of $\eta \rightarrow e^+e^-e^+e^-$	82
4.23	Missing mass of ${}^3\text{He}$ is developing, $\eta \rightarrow e^+e^-e^+e^-$	82
4.24	Missing mass of ${}^3\text{He}$ after the topological cuts	83
4.25	Missing mass of the decay products $e^+e^-e^+e^-$	84

4.26	Missing mass of ${}^3\text{He}$	84
4.27	${}^3\text{He}$ missing mass after topological conditions	87
4.28	${}^3\text{He}$ missing mass after the cut on $MM_{e^+e^-e^+e^-}$ (2.6 - 2.9) $GeV c^2$	87
5.1	$MM({}^3\text{He})$ after the topological cuts and MM_{eeee}	90
5.2	Consistency cuts for data subsets	92
5.3	$MM({}^3\text{He})$ after the cut on $MM_{e^+e^-e^+e^-}$ 2.64 – 2.96	94
5.4	Missing mass of the decay products $MM_{e^+e^-e^+e^-}$	95
5.5	$MM({}^3\text{He})$ after cuts on $MM_{e^+e^-e^+e^-}$	96
5.6	$MM({}^3\text{He})$ after the 2.62-2.96 $MM_{e^+e^-e^+e^-}$	97
5.7	$MM({}^3\text{He})$ after $IM_{e^+e^-} < 0.12 GeV/c^2$	98
5.8	$MM({}^3\text{He})$ after $IM_{e^+e^-} < 0.06 GeV/c^2$	99
5.9	$MM({}^3\text{He})$ after $\Omega_{e^+e^-} < 20^\circ, \Omega_{e^+e^-} < 60^\circ$	100
5.10	$MM({}^3\text{He})$ after $\Omega_{e^+e^-} < 80^\circ$	101
5.11	$MM({}^3\text{He})$ and event overlap	103
7.1	Times of event candidates	107
7.2	Particle identification plot by SE and MDC, $\eta \rightarrow e^+e^-\gamma$	108
7.3	Particle identification plot by SE and MDC, $\eta \rightarrow e^+e^-e^+e^-$	109
7.4	Individual missing mass of ${}^3\text{He}$ for each η Monte Carlo channel	110

List of Tables

1.1	Conservation laws	2
1.2	Classification of mesons	3
1.3	Properties of the η -meson	5
1.4	Non hadronic decay modes of the η -meson	7
2.1	Pellet target parameters	18
3.1	Kind of tracks in the central detector	50
4.1	Experimental conditions, in beamtime 2008	61
4.2	Calibration sets	64
4.3	Simulated Monte Carlo channels	67
4.4	Preliminary estimates of admixture of some η decay channels . . .	67
4.5	Cross sections of prompt pions, single Dalitz	75
4.6	Efficiencies of the cuts for $\eta \rightarrow e^+e^-e^+e^-$	85
4.7	Cross sections of prompt pions	86
5.1	Results for the branching ratio calculations, example	90
5.2	Branching ratio calculations, prompt pions	93
5.3	Branching ratio calculations, $MM_{e^+e^-e^+e^-}$	96
5.4	Branching ratio calculations, $IM_{e^+e^-}$, polynomial.	97
5.5	Branching ratio calculations, $\Omega_{e^+e^-}$, polynomial.	101
5.6	Branching ratio calculations, event overlap, combined function. .	102
5.7	Branching ratio calculations, summarized	104

Acknowledgements

The work presented in this document is the result of great efforts of many colleagues from WASA-at-COSY collaboration. I continue to wonder how it was possible to provide such experiment, take data and finally analyse them in front of computer monitor. This is amazing.

I express my gratitude to Prof. Dr. Hans Ströher for a great opportunity to work in research field of Nuclear Physics at the Institute für Kernphysik in Forschungszentrum Jülich. I say thank him very much for his time and his support along all my way from the beginning till present moment. Thank you very much!

I would like to thank Volker Hejny for his great support in data analysis business, for exact answers on my uncertain questions, for valuable advices and his *knowledge about everything*. Ok, for sure everything in RootSorter and data acquisition system. Thank you very much!

I would like to thank Magnus Wolke for teaching me physics and valuable advices how to analyse data. Thank you very much!

I would like to thank Andrzej Kupsc for teaching me in both: physics and data analysis. Thanking to his valuable comments the work was moving forward. Thank you very much!

I would like to say thank you to Susan Schadmand for adapting my english to English and for fast response during reading the thesis. Thank you very much!

I express my thanks to Christian Pauly and Christoph Redmer for countless discussions and finding the time to answer my questions. Many questions have been solved on the way to your offices and on the way back, thank you very much!

I would like to thank my colleagues: Peter Vlasov, Patrick Wurm, Małgorzata Hodana, Daniel Coderre, Michał Janusz. It was very fruitfull to cooperate with you!

Many thanks to my cellmate Andrey Polyanskiy for daily discussions and immediate response on my questions about histogram fitting and many others.

I would like to thank Pavel Saviankou for his interest in data analysis.

Of course I am gratefull to my wife Anna for her understanding, patience and care...

Erklärung

Ich versichere, daß ich die von mir vorgelegte Dissertation selbständig angefertigt, die benutzten Quellen und Hilfsmittel vollständig angegeben und die Stellen der Arbeit - einschließlich Tabellen, Karten und Abbildungen -, die anderen Werken im Wortlaut oder dem Sinn nach entnommen sind, in jedem Einzelfall als Entlehnung kenntlich gemacht habe; daß diese Dissertation noch keiner anderen Fakultät oder Universität zur Prüfung vorgelegen hat; daß sie - abgesehen von unten angegebenen Teilpublikationen - noch nicht veröffentlicht worden ist sowie, daß ich eine solche Veröffentlichung vor Abschluß des Promotionsverfahrens nicht vornehmen werde.

Die Bestimmungen dieser Promotionsordnung sind mir bekannt. Die von mir vorgelegte Dissertation ist von Herrn Prof. Dr. Ströher betreut worden.

Leonid Yurev

Publications

Study of the decay $\eta \rightarrow e^+e^-e^+e^-$ with WASA-at-COSY. Published in AIP Conf.Proc. 950: 232-235, 2007

Lebenslauf

Name:	Leonid Yurev
geboren am:	25.12.1983
geboren in:	Voronezh, USSR
Anschrift:	Vogelsangstrasse 4a 52428 Jülich
Familienstand:	verheiratet
Staatsangehörigkeit:	russisch

Schulbildung:	
09.1991 - 05.1999	Grundschule <i>N</i> 28 in Voronezh
09.1999 - 05.2001	Gymnasium namens Akademiker N.G. Basov bei der staatlichen Universität der Stadt Voronezh

Studium:	
09.2001 - 06.2005	Bakkalaures der Physik an der Staatlichen Universität der Stadt Voronezh
09.2005 - 06.2006	Diplom in Physik an der Staatlichen Universität der Stadt Voronezh

Berufstätigkeit:	
seit 07.2006	Ausländischer Mitarbeiter am Forschungszentrum Jülich